DISSERTATION

Modeling and Control of Reheating Strategies for Refractory Metals

Ausgeführt zum Zwecke der Erlangung des akademischen Grades eines
Doktors der technischen Wissenschaften (Dr. techn.)

unter der Leitung von

Univ.-Prof. Dipl.-Ing. Dr. techn. Andreas Kugi
E376
Institut für Automatisierungs- und Regelungstechnik

eingereicht an der
Technischen Universität Wien
Fakultät für Elektrotechnik und Informationstechnik

von

Florian Rötzer
Matrikelnummer: 00925939

Wien, Juli 2021

Studiendekan:	Univ.-Prof. Dr.-Ing. Wolfgang Gawlik
Betreuer:	Univ.-Prof. Dipl.-Ing. Dr. techn. Andreas Kugi
Tag des Rigorosums:	30. August 2021
Prüfungsvorsitzender:	Univ.-Prof. Dr.-Ing. Wolfgang Gawlik
Erster Gutachter:	Prof. Ian Craig, Ph.D.
Zweiter Gutachter:	Associate Prof. Dipl.-Ing. Dr.-Ing. Wolfgang Kemmetmüller

Abstract

The production of plates from refractory metals involves several reheating processes that have a critical influence on the quality of the final product. This thesis deals with the application of control engineering methods to two reheating processes in a flat stock production line. The objective in both cases is to save time and energy in the reheating processes, while the quality of the products should not be compromised.

In the first part of the thesis, batch-type chamber furnaces used in a hot rolling plant are considered. Energy saving is achieved by minimizing the residence times for each product that is charged into the furnace. When the product is in the furnace, its temperature cannot be measured. Therefore, a detailed process model of the chamber furnace is derived from first principles and subsequently reduced to a first-order nonlinear system, which is able to capture the time evolution of the discharge temperature of the product with sufficient accuracy. The first-order model is exploited in a learning strategy to improve the estimates of the minimum residence times from one product to the next. Additionally, the products of the plant are assigned to product classes according to their material and surface properties to further improve the estimation results.

Simulation studies are performed with the validated detailed process model and the proposed learning strategy with different product classes. The results show a high accuracy if the product parameters are well known. Uncertainties in the product parameters have a moderate influence on the estimation results that can be mitigated by narrowing the definitions of the product classes. The designed estimator is computationally inexpensive and can be applied to a wide range of similar furnace systems.

The second part of the thesis deals with an induction heating system used in the strip coil production. Thin sheets of refractory metals are reheated along a cutting

line to improve the quality of the cutting edges. Flatness defects of the sheet cause fluctuations in the air gap between the inductor and the sheet, which entail strong temperature inhomogeneities. The goal is to bring the temperature along each cutting line above a minimum threshold without unnecessary overheating.

The induction heating problem is formulated as a multiphysics process model, which is subsequently simplified for the controller design. The resulting control-oriented model consists of an advection equation and an equivalent circuit model. Based on the control-oriented model, a cascade controller for the transmitted heating power and a two-degrees-of-freedom temperature controller, comprising a feedforward and a feedback part, are designed to compensate for changes in the mean air gap.

Based on the validated detailed process model, the performance of the designed temperature controller is tested in extensive simulation studies. The results show that the proposed controller performs well for sufficiently homogeneous air gap geometries. The concept allows for further improvements in several directions, depending on the available system inputs and outputs.

Kurzzusammenfassung

Bei der Produktion von Platten aus Refraktärmetallen werden mehrere Erwärmprozesse durchlaufen, welche einen entscheidenden Einfluss auf die Qualität des Endprodukts haben. Die vorliegende Arbeit befasst sich mit der Anwendung regelungstechnischer Methoden auf zwei Erwärmprozesse in einer Flachgüterproduktionslinie. Das Ziel ist in beiden Fällen die Reduktion von Zeit- und Energieverbrauch des jeweiligen Prozesses, wobei die Qualität des Produkts erhalten bleiben soll.

Im ersten Teil der Arbeit werden die Kammeröfen einer Warmwalzanlage betrachtet. Durch Minimierung der Liegezeit der Produkte im Ofen wird Energie eingespart. Während des Erwärmens im Ofen kann die Produkttemperatur nicht gemessen werden. Deshalb wird ein detailliertes Prozessmodell eines Kammerofens erstellt und sukzessive auf ein nichtlineares Modell erster Ordnung reduziert, welches imstande ist, den zeitlichen Verlauf der Produktentnahmetemperatur hinreichend genau abzubilden. Das Modell erster Ordnung dient als Basis für eine Lernstrategie, die die Schätzung der minimalen Liegezeiten von Produkt zu Produkt verbessert. Darüber hinaus wird das Produktportfolio nach Materialeigenschaften und Oberflächenbeschaffenheit in Produktklassen eingeteilt, um die Genauigkeit der Schätzung weiter zu erhöhen.

Die vorgeschlagene Lernstrategie mit mehreren Produktklassen wird anhand des validierten Prozessmodells in ausführlichen Simulationsstudien getestet. Für den Fall, dass die Produktparameter hinreichend genau bekannt sind, weisen die erzielten Ergebnisse eine sehr hohe Genauigkeit auf. Unsicherheiten in den Produktparametern zeigen einen mäßigen Einfluss auf das Schätzergebnis, welcher durch Einengung der Definitionen der Produktklassen weiter minimiert werden kann. Der entworfene Schätzer kann ohne großen Rechenaufwand implementiert werden und ist für eine Vielzahl von ähnlichen Öfen anwendbar.

Der zweite Teil der Arbeit beschäftigt sich mit der induktiven Erwärmung in der

Bandrollen-Produktionsanlage. Dünne Bleche werden entlang einer Schnittspur erwärmt, um die Qualität der Schnittkanten zu verbessern. Unebenheiten im Blech bewirken dabei Schwankungen des Luftspalts zwischen Induktor und Blech, welche wiederum starke Inhomogenitäten beim Erwärmen der Schnittspur nach sich ziehen. Das Ziel ist es nun, die Temperatur entlang jeder Schnittspur über einen vorgegebenen unteren Schwellwert zu bringen, ohne unnötig zu überheizen.

Für das induktive Erwärmproblem wird zunächst ein detailliertes Prozessmodell erstellt und anschließend für den Reglerentwurf vereinfacht. Das resultierende Entwurfsmodell besteht dabei aus einer Transportgleichung für das thermische und einem Ersatzschaltbild für das elektromagnetische Teilsystem. Auf Basis des Entwurfsmodells wird dann ein kaskadierter Reglerentwurf durchgeführt. Der innere Kreis der Kaskade regelt die übertragene Heizleistung und über den äußeren Kreis wird die Temperatur entlang der Schnittspur über eine Zwei-Freiheitsgrad-Regelung, bestehend aus einem Vorsteuer- und einem Regleranteil, eingestellt und Schwankungen des Luftspaltmittelwerts ausgeglichen.

Die Regelgüte des entworfenen Zwei-Freiheitsgrad-Reglers wird anschließend in Simulationsstudien am validierten Prozessmodell getestet. Die Ergebnisse zeigen, dass der Regler für einen hinreichend homogenen Luftspalt sehr gut arbeitet. Der Regler erlaubt verschiedene Erweiterungen, je nach Vorhandensein von Stellgrößen und Messinformationen.

Contents

List of Symbols

Abbreviations

1DOF	1 degree of freedom
2DOF	2 degrees of freedom
AC	Alternating current
FE	Finite element (method)
FV	Finite volume (method)
LQG	Linear-quadratic Gaussian
LQR	Linear-quadratic regulator
ODE	Ordinary differential equation
PDE	Partial differential equation
PI	Proportional-integral
POD	Proper orthogonal decomposition
RLS	Recursive least-squares
RMS	Root-mean-square

General notation

$\arg\min$	Solution of an optimization (minimization) problem
$\mathrm{cov}(\cdot)$	Covariance of a stochastic vector with itself
Δ	Laplace operator, Change of a quantity
$\mathrm{dist}(\cdot,\cdot)$	Euclidean distance between points or sets
$\emptyset$	Empty set
$\mathbb{R}^3$	3D Euclidean space
∂	Boundary of a set

∂_n	Surface normal (partial) derivative
∂_t	Time (partial) derivative
$\mathrm{Re}(\cdot)$	Real part of a complex number
$\mathbf{0}$	Zero vector or matrix
$\mathbf{1}$	Vector or matrix of ones
$\boldsymbol{\nabla}$	Spatial gradient
$\boldsymbol{a} \cdot \boldsymbol{b}$	Inner product of $\boldsymbol{a}$ and $\boldsymbol{b}$
$\boldsymbol{a} \times \boldsymbol{b}$	Cross-product of $\boldsymbol{a}$ and $\boldsymbol{b}$

Part I, Latin Symbols

A	Area
a	Absorptivity
C	Global heat capacity
c_p	Specific heat capacity
E	Radiation exchange factor
e	Error/difference between two quantities
$\mathcal{F}$	Radiation exchange function (integral kernel)
F	Radiation view factor
m	Mass
N	Total count of elements, model order
$\dot{Q}$	Global heat flux
$\dot{q}$	Heat flux density
q	Forgetting factor in RLS
R	Thermal resistance
r	Reference value (temperature control), diffuse reflectivity
T	Temperature
t	Time coordinate
t^{in}, t^{out}	Charge time, discharge time
u	Supplied total heating power
y	Sensor output
$\boldsymbol{A}$	Dynamic matrix of a system or model
$\boldsymbol{B}$	Input matrix of a system or model
$\boldsymbol{C}$	Output matrix of a system or model
$\boldsymbol{c}$	Output vector of a system or model
$\boldsymbol{D}$	Data matrix
$\boldsymbol{d}$	Disturbance inputs to a system or model
$\boldsymbol{e}$	Error/difference between two vectors

$\boldsymbol{K}$	Controller gains
$\boldsymbol{M}$	Mass matrix of a system or model
$\boldsymbol{R}$	Radiation nonlinearity of a system or model
$\boldsymbol{T}$	Temperature vector
$\boldsymbol{u}$	Supplied heating powers per zone
$\boldsymbol{V}$	Matrix of eigenvectors
$\boldsymbol{v}$	Eigenvector
$\boldsymbol{x}$	Spatial coordinate in $\mathbb{R}^3$, generic system state
$\boldsymbol{y}$	Sensor output vector

Part I, Greek Symbols

α	Heat transfer coefficient
β	Overheating ratio
ε	Emissivity
η	Scaling factor for λ of hydrogen-infused porous media
η^p	Substitutional parameter for plate emissivity
Γ	2D surface in $\mathbb{R}^3$
λ	Thermal conductivity
μ	Eigenvalue
Ω	3D domain in $\mathbb{R}^3$
ρ	Mass density
σ	Stefan-Boltzmann constant

Part I, Diacritics, Superscripts, Subscripts

$\hat{\zeta}$	Estimate of ζ
$\overline{\zeta}$	Upper limit for ζ
$\widetilde{\zeta}$	POD projection of ζ
$\underline{\zeta}$	Lower limit for ζ
ζ^*	Solution ζ an optimization problem
ζ^{ct}	ζ of the contact heat transfer
ζ^{id}	ζ of the identification method
ζ^{∞}	ζ of the surroundings
ζ^{in}	ζ of the inner wall surfaces, ζ at charge time
ζ^{out}	ζ of the outer wall surfaces, ζ at discharge time
ζ^{PI}	ζ of the PI controllers
ζ^{rad}	ζ of the radiation exchange
ζ^{c}	ζ of a cluster c

ζ^d	ζ of the furnace door, ζ of the disturbance input
ζ^h	ζ of the heaters
ζ^m	ζ of the measurement box
ζ^p	ζ of the plate
ζ^u	ζ of the heating powers
ζ^w	ζ of the furnace walls
$\zeta_1, \zeta_2, \zeta_{12}$	ζ of two adjacent domains, or their interface
$\zeta_i, \zeta_j, \zeta_k, \zeta_c$	i^{th}, j^{th}, k^{th}, or c^{th} element in a family of ζ
ζ_s	ζ at steady state

Part II, Latin Symbols

a^{g}	Air gap width
a^{tr}	Transformer ratio
b	Input function (spatial distribution of the input power)
C	Courant number
C^{r}	Capacitor
c_p	Specific heat capacity
G_{uy}	Transfer function from u to y
h	Enthalpy density
I	Current (RMS)
i	Imaginary unit $\sqrt{-1}$
J	Current
L_σ	Stray inductance
L_h	Coupled inductance
l_x, l_y, l_z	Measurements of the heated domain
N	Model order
n	Measurement noise
P	Power (active)
Q	Global heat source, process noise variance
q	Local heat source, forgetting factor in RLS
R	Resistance
$\underline{S}$	Complex power
T	Temperature
t	Time coordinate
U	Voltage (RMS)
u	Virtual (power) input
v_x	Velocity in x direction

w	Process noise
x	Spatial coordinate (longitudinal)
x^{h}	Leading (head) edge of the sheet
x^{t}	Trailing (tail) edge of the sheet
y	System output, spatial coordinate (vertical)
z	Spatial coordinate (lateral)
$\boldsymbol{A}$	Magnetic vector potential
$\boldsymbol{B}$	Magnetic flux density
$\boldsymbol{c}$	System output vector
$\boldsymbol{E}$	Electric field
$\boldsymbol{G}$	Process noise input vector
$\boldsymbol{H}$	Magnetic field
$\boldsymbol{h}$	Discretized system state (mean enthalpy densities at grid points)
$\boldsymbol{I}$	Identity matrix
$\boldsymbol{J}$	Current density
$\boldsymbol{n}$	Surface normal unit vector
$\boldsymbol{P}$	Error covariance matrix
$\boldsymbol{v}$	Eigenvector or POD mode
$\boldsymbol{x}$	Spatial coordinate (3D), system state vector

Part II, Greek Symbols

δ	Discrete-time shift operator
δ^{in}, δ^{out}	Flag: sheet visible at entry/exit point
δ_0	Discrete-time impulse function
Γ	2D Surface in 3D space
λ	Thermal conductivity
μ	Magnetic permeability, eigenvalue
Ω	3D domain
ω	Angular frequency
ϕ	Phase angle
ρ	Mass density
σ	Electric conductivity
$\boldsymbol{\Gamma}$	System input vector
$\boldsymbol{\Phi}$	System dynamic matrix

Part II, Diacritics, Superscripts, Subscripts

$\hat{\zeta}$	Estimate of ζ, peak value of ζ
$\overline{\zeta}$	Mean/average value of ζ
$\widetilde{\zeta}$	Variation of the notion ζ
ζ^{ext}	Extrinsic ζ
ζ^{fb}	ζ of the feedback loop
ζ^{Fe}	ζ of the magnetic cores
ζ^{ff}	ζ of the feedforward loop
ζ^{g}	ζ of the air gap
ζ^{h}	ζ of the leading sheet edge
ζ^{id}	ζ for identification
ζ^{in}	ζ at the entry point
ζ^{out}	ζ at the exit point
ζ^{r}	ζ of the capacitor
ζ^{s}	ζ of the AC source
ζ^{t}	ζ of the trailing sheet edge
ζ^{tr}	ζ of the ideal transformer
ζ^{c}	ζ of the inductor coil
ζ^{d}	ζ of lateral heat diffusion
ζ^{e}	ζ of the estimator (Kalman filter)
ζ^{h}	ζ of the net heating (sheet)
ζ^{l}	ζ of the total losses
ζ^{p}	ζ of the sheet
$\zeta_1, \zeta_2, \zeta_{12}$	ζ of two adjacent domains, or their interface
ζ_{meas}	ζ measured
ζ_j, ζ_k	j^{th} or k^{th} element in a family of ζ
ζ_x	ζ in x direction

CHAPTER 1

Introduction

The production of high-quality heavy plates, sheets and strips of refractory metals is a widely uncharted territory in control engineering. Refractory metals are a class of elements that have melting points beyond 2200°C and are very resistant to mechanical wear (cf. [7, p.120]). Typical representatives of this class are niobium (Nb), molybdenum (Mo), tantalum (Ta), tungsten (W), and rhenium (Re). Their thermal, mechanical and electric properties make refractory metals a valuable resource for the semiconductor industry which, in turn, has highest demands on the purity and microstructure of these metal products.

Plansee SE is the world-leading supplier of refractory metals – both pure and alloyed – for the semiconductor industry. Their standard way of producing flat stock (i.e., plates, sheets and strips) from refractory metals is by powder metallurgy (see [34]), where plates and sheets are produced from powders of refractory metal oxides, sulfides, etc. The powders undergo chemical preprocessing and are sintered into blocks. The blocks are subsequently formed at a hot rolling plant. Further heating, cutting and grinding steps follow, depending on the product. For hot rolling and strip cutting, reliable control of the involved reheating processes is crucial to ensure a high product quality.

This thesis deals with the optimization of the performance of these reheating systems by means of modern control engineering techniques. The reheating system of the hot rolling plant comprises several chamber furnaces, while the reheating prior to strip cutting is done by a number of parallel induction heating units. Both systems are batch-type reheating systems (as opposed to continuous furnaces) which follow the strategies of reheating by waiting and reheating by active control, respectively.

The reheating-by-waiting strategy is applied to reheating tasks where the final temperature of a product is relevant, but the heating trajectory itself is, at least

within certain limits, arbitrary. Part I of this thesis is concerned with this strategy to reheat the sintered blocks of refractory metals above their recrystallization temperature in chamber furnaces before and during the rolling process. The chamber furnaces are controlled to a predefined constant setpoint temperature and the products are charged into the furnaces for a certain time period. The main research question is how to determine the right discharge times of the various products (different geometries, materials, surface properties) depending on the desired target temperature and temperature homogeneity in the product.

Part II of this thesis deals with the inductive reheating of thin sheets of refractory metal along a predefined cutting line before the sheet is cut into stripes. Since the sheets are not perfectly flat, the air gaps under the inductors change along the length of the sheet, which in turn causes large temperature fluctuations. The main research question here is to design a temperature control concept which systematically compensates for the varying (unmeasured) air gaps.

This research work was part of the EU project SemI40 (see also [63]). Parallel to the investigations in this thesis, further aspects of the production line were optimized. The related publications [1–3] deal with the optimal production schedule in the hot rolling plant. The optimization of the production schedule is based on optimized processing times which are the central result of Part I of this thesis.

Part I

Reheating of Sintered Blocks in Chamber Furnaces

CHAPTER 2

Preliminaries

This first part of the thesis deals with the reheating process in the hot rolling plant of Plansee SE. The hot rolling plant is shown in Fig. 2.1. Sintered blocks of refractory metals enter the product charging station and a manipulator charges them into one of several batch-type chamber furnaces. The blocks are reheated above their recrystallization temperature to increase formability (i.e., ductility) and rolled out into heavy plates at a reversing millstand in several passes.

The reheating of plates takes significantly longer than the rolling passes. For this reason, several furnaces are used in parallel. Each furnace operates at an individual fixed setpoint temperature. The plates charged into the furnace asymptotically reach the furnace temperature, which corresponds to the desired plate temperature.

With each rolling pass, the plate experiences a certain drop in temperature due to thermal radiation and the contact of the plate with the working rolls and the roller table. If the plate temperature is too low, both the working rolls and the plate are at risk to be damaged. While the rolls experience increased wear due to the decreased ductility of the plate, the deformability necessary to non-destructively roll the plate to the desired thickness is not given. For the plates, cracks and inhomogeneous microstructure are the consequence, and the production yield effectively drops.

To keep the plate temperature above a certain level during rolling, it is necessary to reheat the plate again after a few rolling passes.

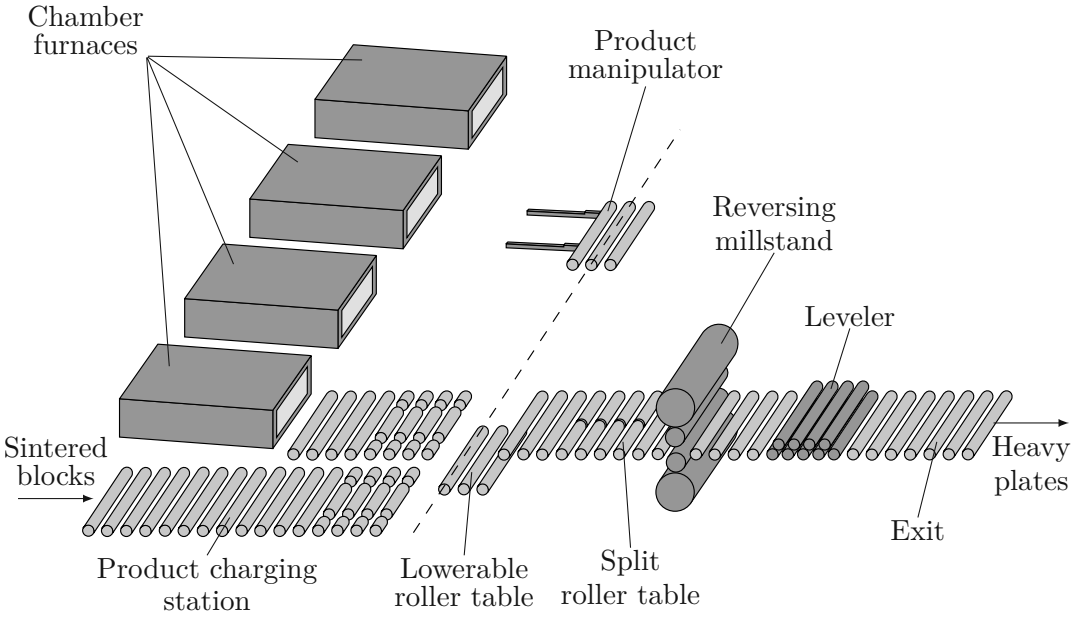

Figure 2.1: Hot rolling plant.

2.1 Industrial Requirements

For the reheating process, the requirement is to optimize both the energy consumption and the throughput of each furnace. The furnace geometry and mode of operation cannot be changed. The required exit temperature of each plate is specified by a desired reference value and a tolerance range, typically around 30°C.

The furnace is controlled to a fixed operating point and dissipates a certain amount of heating power at steady state. Additional heating power is required only when a plate is being reheated. The ceramic walls of the furnace are around one meter thick. Consequently, the overall wall temperature changes only slowly compared to the plate temperature. An improvement of the control concept for the furnace temperature is therefore not a promising option to reduce the energy consumption or to enhance the throughput. Both the energy consumption and the throughput can be improved if the reheating time is minimized. Therefore, the minimization of reheating times is one of the main goals of this thesis.

The diversity of products that are processed by the hot rolling plant also entails a logistic problem. In terms of throughput, the optimal sequence of products for reheating and rolling is not known in advance. This problem is addressed in the related works [1–3].

2.2 State of the Art

The computation of the minimal reheating time for a product in the furnace requires exact knowledge of the product temperature. In the considered case, the product temperature is not measured and must therefore be estimated based on a suitable mathematical model.

2.2.1 Reheating Time Optimization

In the last decades, different applications with a similar goal have been reported in the literature, where reheating processes were analyzed in terms of residence time and energy efficiency.

The optimal residence time for the annealing of steel coils in hydrogen-based batch-type furnaces was investigated in [59, 60]. The heating schedule was improved empirically with respect to the reheating time, temperature homogeneity, and other constraints imposed on the system. A more systematic approach to the optimization of residence times in similar furnaces was given in [11]. A validated mathematical model of the furnace was used to calculate the optimal residence times, with respect to the coil dimensions, off-line. Since this is a brute-force approach, the parameter space of the products has to be sufficiently small and the mathematical model has to be computationally inexpensive. For larger parameter spaces, where some parameters might be unknown or uncertain, the works [61, 62] suggest the transition to an artificial neural network. As a result, the optimal residence time for each product can be calculated on demand. However, using a neural network comes with inherent downsides, like possible overfitting. Also, correct results for untested data are achieved only with a certain probability, which is not desirable in the production of refractory metal plates due to the relatively small lot sizes and high costs of a single plate.

Similarly, the reheating of steel slabs in a walking-beam or pusher-type furnace was investigated. In [22], five distinct modes of operation, including different reheating times, were compared in terms of mean slab temperatures, skid marks, and heat flux to find an optimum. The influence of a fixed process time was investigated more thoroughly in [37], where the expected exit temperature, skid marks, and temperature inhomogeneity for a corresponding reheating time were reported. The findings are valuable for understanding the influence of the chosen reheating time, however, for optimization, the inverse problem is of interest. In [12], the optimum reheating time for a slab with respect to the slab thickness and the admissible temperature inhomogeneity was investigated. The calculations are done off-line for a small space of parameters.

The existing works mainly focus on a furnace operation where products are heated in an environment which can rapidly change its temperature. This is achieved either by moving the product from one furnace zone to the next, or by changing the temperature of the heating media. When the furnace temperature

can be controlled in a dynamic way, the product temperature can be actively steered towards the desired exit temperature without the need to wait for its asymptotic convergence.

The furnaces considered in this thesis maintain a near-constant temperature during the reheating process, which causes an increased sensitivity of the required reheating time with respect to the product temperature. Along with this higher sensitivity comes the need for an accurate and computationally efficient model of the considered reheating process. For this reason, the state of the art concerning furnace modeling is examined next.

2.2.2 Furnace Modeling and Simulation

Different furnace models with varying detail and complexity have been reported over the last years, where a strong focus was laid on reheating furnaces with moving batches. Control-oriented models in one or two spatial dimensions for the online calculation of different points of operation have been used in the steel industry for several decades, see, e.g., [74].

Three-dimensional models of walking-beam and pusher-type furnaces were published based on finite differences [30], tailored finite-volume methods [21, 35, 38], finite-element methods [40], and tailored Galerkin methods [68]. The models have become more and more complex, taking into account different effects like the radiation exchange in non-gray gaseous media. Tailored methods aim at low computational costs and moderate accuracy. The reported stationary accuracy of such models is up to 20°C, which is roughly the accuracy required in the reheating process considered in this thesis.

Computations with high accuracy were achieved in [31, 49] using the software Ansys Fluent. Stationary errors were reported as low as 10°C, while errors in the transient phase were below 40°C. Results with such a high accuracy are desirable for the reheating process considered in this thesis. Unfortunately, they come at relatively high computational costs, as the underlying mesh comprises several hundred thousand nodes.

Batch-type furnaces cover a wide spectrum from reheating to heat treatment furnaces. Depending on the application, the heating may be performed very slowly or quickly. Accordingly, the transient accuracy of the reported simulation models can vary in a wider range. For instance, batch-type furnaces were modeled in a single spatial dimension using finite differences in [71]. For a metal strip annealing furnace, a mathematical model with an accuracy of 25°C is reported in [28]. In a follow-up work, the model was extended to two spatial dimensions and an accuracy of 15°C over the whole temperature profile could be achieved. Similar accuracy in three spatial dimensions are the results in [32, 43]. All of the above-mentioned models of batch-type furnaces rely on tailored finite-difference schemes to achieve a good compromise between accuracy and computational effort.

Similar results with less modeling effort can be achieved using numerical solvers

like ANSYS FLUENT as in [23, 73], or BAFSIM in [61]. The accuracy again comes at higher computational costs.

In view of the achievable low errors (about 10°C), it has become state of the art to model the furnaces with numerical solvers, like finite-element (see, e.g., [14]) or finite-volume software, and make forward predictions of the process outcome. A comparison of different levels of detail for a model of a walking-beam furnace is given in [65]. The results suggest to find the right balance between model accuracy and complexity. In particular, at a certain point in the modeling process, it is recommendable to give up a further increase of the level of detail in favor of exploiting parameter estimation strategies to improve the model accuracy.

2.2.3 Temperature and Parameter Estimation

In order to estimate and correct the product temperature in real time, a feedback loop with some meaningful sensor information is required. Usually, during a reheating cycle, the product temperature is not measured directly, but the furnace temperature is available. If the product temperature has a significant influence on the furnace temperature, an estimator similar to [33] can be used to approximate the product temperature. Unfortunately, in the considered furnace, the product's influence on the wall temperature is minor.

The product temperature can, however, be determined by forward calculation of a mathematical model, see, e.g., [67, 68]. If the product temperature before and after the reheating process is available, the relevant parameters of the reheating process can be estimated and the evolution of the product temperature during reheating can be determined with increasing accuracy. A similar idea for a continuous furnace can be found in [69].

2.3 Motivation and Goals

The forward calculation of processing times based on pure first-principles models exhibits limited accuracy if the model parameters are not well known. Algorithms based on artificial intelligence (AI) and machine learning, on the other hand, show promising accuracy (see, e.g., [6, 29]) and fast computation times, however, they are often not reliable. Thus, it seems desirable to combine these two approaches.

Efforts from the AI perspective were made in the form of physics-informed neural networks, see, e.g., [51]. At the core, this is still a neural network and it was not explicitly examined how the solutions will behave if the process parameters are uncertain or change over time.

In the present case, for the purpose of reliability, we want to have a physical model at the center of our solution. The model parameters will be tuned with data-driven methods that allow for continuous updates to ensure a high accuracy even if the process parameters drift over time.

The goal is to develop a system that gives reliable and accurate calculations of the reheating times at minimal computational costs. In a larger context, the calculation of the reheating times should be embedded in a continuously-updating scheduling problem (see [3]), which explains the need for very fast computations.

2.4 Approach and Scientific Contributions

The approach pursued in this thesis can be summarized as follows:

- Design a process model with reasonable complexity and find the most relevant uncertain parameters.
- Evaluate the model accuracy and apply appropriate model order reduction techniques.
- Utilize discharge temperature measurements to correct the model and improve the estimate of the reheating times.

Large parts of the mathematical modeling approach and the estimator design are already published in [56, 57].

2.5 Outline of Part I

Part I of the thesis is organized as follows: Chapter 3 is concerned with the derivation of a detailed process model. The relevant heat transfer mechanisms are identified and modeled based on a simplified geometry. A coarse meshing strategy is proposed, the detailed process model is discretized, and uncertain parameters are identified.

In Chapter 4, the discretized process model is simplified by means of proper orthogonal decomposition, and the modal dynamics are examined. Based on the findings, a minimal model is derived to approximate the relevant parts of the dynamics.

The real-time calculation of optimum reheating times, based on estimates of the uncertain parameters in the process, is introduced in Chapter 5. In particular, the minimal model is extended by an online parameter estimator, where the estimates are driven by the measured plate exit temperatures. Similar products are assigned to product classes and the estimated class mean values of the uncertain parameters are used to determine the reheating times. The performance of the designed estimator is evaluated by means of the detailed process model from Chapter 3.

Finally, Chapter 6 contains some concluding remarks and gives an outlook on potential follow-up work.

CHAPTER 3

Physical Modeling

As a basis for all further investigations, a detailed mathematical model of the considered chamber furnaces is derived in this chapter. Large parts of the described modeling process are already published in [56].

The geometry of such a furnace is outlined in Fig. 3.1. The furnace operates at a setpoint temperature which corresponds to the desired final temperature of the load, i.e., the metal plate. This setup prevents the load from overheating.

The furnace is charged with a plate made of sintered or rolled molybdenum (or other refractory metals) that absorbs heat from the surrounding chamber. The furnace chamber is divided into a number of individually controlled zones to improve the spatial homogeneity of the furnace temperature. The atmosphere in the chamber is pure hydrogen gas to avoid and revert oxidation on the plate surface.

The furnace is electrically heated by resistors, which are uniformly distributed on the ceiling of the chamber. The furnace doors are built as radiation shields and the furnace walls consist of different layers of refractory ceramics. The walls and the furnace entrance are enclosed by a steel framework to prevent hydrogen leakage and to support the refractory ceramics.

Based on the manufacturing plan of each product, a human operator decides when a plate is charged into a furnace or discharged for rolling. When the plate is charged or discharged, a two-color pyrometer under the furnace door measures the entry or exit temperature along a line on the bottom of the plate. This measurement is treated as ground truth for the heating process.

The plate is required to reach its desired final temperature in minimal time. While the plate is in the furnace, its temperature cannot be measured directly. Thus, in order to ensure a reliable reheating of the plates and simultaneously minimize the reheating times, an accurate online estimate of the plate temperature

Figure 3.1: Sketch of the considered chamber furnace with three zones.

is required.

The goal of this chapter is therefore to derive a detailed process model based on first principles that correctly predicts the furnace behavior and the temperature profile in the plate, such that the calculated plate exit temperature resembles the pyrometer measurements with high accuracy.

3.1 Heat Transfer and Furnace Geometry

In this section, a PDE model for the heat exchange in the system is derived. This model will be the starting point for all further investigations in the subsequent chapters.

3.1.1 Heat Transfer

According to the furnace geometry shown in Fig. 3.1, let Ω^w and Ω^p be the domains of the furnace wall and the product, such that

$$\Omega^w \subset \mathbb{R}^3, \quad \Omega^p \subset \mathbb{R}^3, \quad \Omega^w \cap \Omega^p = \emptyset, \quad \partial\Omega^w = \Gamma^{\text{in}} \cup \Gamma^{\text{out}}. \tag{3.1}$$

In each of these solids, heat conduction at a point $\boldsymbol{x}$ and time t is governed by

$$\rho(\boldsymbol{x})c_p(T,\boldsymbol{x})\partial_t T = \boldsymbol{\nabla}\cdot(\lambda(T,\boldsymbol{x})\boldsymbol{\nabla}T), \quad \boldsymbol{x}\in\Omega^w\cup\Omega^p, \quad t>0 \tag{3.2a}$$

$$-\lambda(T,\boldsymbol{x})\partial_n T = \dot{q}(T,\boldsymbol{x},\boldsymbol{u}), \quad \boldsymbol{x}\in\partial\Omega^w\cup\partial\Omega^p, \quad t>0 \tag{3.2b}$$

$$T|_{t=0} = T_0, \quad \boldsymbol{x}\in\Omega^w\cup\Omega^p, \quad t=0. \tag{3.2c}$$

Here, the quantities T, ρ, c_p, and λ are the temperature field, density, specific heat and thermal conductivity, respectively. The symbol $\boldsymbol{u}$ denotes the active power supplied to each zone of the furnace, while $\dot{q}$ in the boundary conditions describes a general heat flux on the boundary of each solid. The operator ∂_n denotes the derivative in the outward surface normal direction. The symbol T_0 denotes the initial temperature field. The dependence of the material parameters on the spatial coordinate $\boldsymbol{x}$ refers to the different materials in the system. In particular, the furnace wall is a layered structure built from different refractory ceramics. The density ρ is independent of T, as thermal expansion is expected to be negligible.

The heating powers $\boldsymbol{u} = \left[u_j\right]_{j=1,\dots,N^u}$ are supplied by N^u separate heating wires on the ceiling of the furnace chamber, represented by the surfaces Γ^h_j, with

$$\Gamma^h = \bigcup_{j=1}^{N^u} \Gamma^h_j, \quad \Gamma^h_j \cap \Gamma^h_k = \emptyset \quad \text{if } j \neq k. \tag{3.3}$$

The common assumption is made that the heaters have negligible heat capacities and thus negligible dynamics.

The hydrogen in the furnace diffuses into the porous wall material and considerably alters the thermal conductivity of the wall. To account for this phenomenon, a factor $\eta > 1$ is used to scale the nominal values $\lambda^w(T, \boldsymbol{x})$ accordingly, i.e.,

$$\lambda(T, \boldsymbol{x}) \mapsto \eta\lambda^w(T, \boldsymbol{x}), \quad \boldsymbol{x} \in \Omega^w. \tag{3.4}$$

In order to describe the plate and furnace separately, let ρ^w and c_p^w be the (nominal) density and specific heat capacity of the furnace wall materials. Also, let ρ^p, c_p^p, and λ^p be the respective material parameters of the plate. The PDE model (3.2) thus becomes

$$\begin{aligned}
\rho^w(\boldsymbol{x})c_p^w(T, \boldsymbol{x})\partial_t T &= \boldsymbol{\nabla} \cdot (\eta\lambda^w(T, \boldsymbol{x})\boldsymbol{\nabla}T), && \boldsymbol{x} \in \Omega^w, && t > 0 && \text{(3.5a)}\\
-\eta\lambda^w(T, \boldsymbol{x})\partial_n T &= \dot{q}^w(T, \boldsymbol{x}, \boldsymbol{u}), && \boldsymbol{x} \in \partial\Omega^w, && t > 0 && \text{(3.5b)}\\
T|_{t=0} &= T_0, && \boldsymbol{x} \in \Omega^w, && t = 0 && \text{(3.5c)}\\
\rho^p c_p^p(T)\partial_t T &= \boldsymbol{\nabla} \cdot (\lambda^p(T)\boldsymbol{\nabla}T), && \boldsymbol{x} \in \Omega^p, && t > 0 && \text{(3.5d)}\\
-\lambda^p(T)\partial_n T &= \dot{q}^p(T, \boldsymbol{x}, \boldsymbol{u}), && \boldsymbol{x} \in \partial\Omega^p, && t > 0 && \text{(3.5e)}\\
T|_{t=0} &= T_0, && \boldsymbol{x} \in \Omega^p, && t = 0. && \text{(3.5f)}
\end{aligned}$$

Next, the heat fluxes $\dot{q}^w$ and $\dot{q}^p$ at the boundaries will be formulated.

3.1.1.1 Chamber Boundary Conditions

Inside the furnace chamber, heat transfer between the solid domains can take place mainly via radiation exchange or contact heat transfer. The convective heat transfer in the furnace is up to two orders of magnitude smaller than the radiation exchange and will thus be neglected in the model. For radiation exchange in the furnace, all surfaces are assumed to be gray and Lambertian. The atmosphere in the chamber is hydrogen and therefore considered transparent for radiation (cf. [9, Sec. 13.6]). For contact heat transfer, the Cooper-Mikic-Yovanovich correlation (see [8, Eq. (4.248)]) is employed.

Consider two surface elements, denoted by the index 1 and 2, respectively. The heat flux densities $\dot{q}_{12}^{\text{rad}}$ due to radiation exchange and $\dot{q}_{12}^{\text{ct}}$ due to contact conduction between these elements are given by

$$\dot{q}_{12}^{\text{rad}} = \sigma\varepsilon_{12}\left(T_1^4 - T_2^4\right) = \sigma\varepsilon_{12}\left(T_1^3 + T_1^2T_2 + T_1T_2^2 + T_2^3\right)(T_1 - T_2) \tag{3.6a}$$

$$\dot{q}_{12}^{\text{ct}} = 1.25\frac{2\lambda_1\lambda_2}{\lambda_1 + \lambda_2}\frac{m_{12}^{\text{asp}}}{\sigma_{12}^{\text{asp}}}\left(\frac{p_{12}}{H_{12}}\right)^{0.95}(T_1 - T_2) + \dot{q}_{12}^{\text{rad}}. \tag{3.6b}$$

In (3.6a), σ is the Stefan-Boltzmann constant, ε_{12} is the radiation exchange factor between the two elements, and T_1, T_2 denote the temperatures of the respective surface elements. Additionally, in (3.6b), λ_1 and λ_2 are the thermal conductivities

Parameter	Unit	Typical values	Mean	Source
ε_{12}	–	0.2 – 0.8	0.5	[70]
λ_1, λ_2	W/(Km)	50 – 160, 2.5 – 4.7	105, 3.6	[48], data sheets
σ_{12}^{asp}	µm	1 – 10	5.5	[72, Chap.1]
m_{12}^{asp}	rad	0.1 – 0.4	0.25	[20]
H_{12}	GPa	1.5 – 3.5	2.5	[48]
p_{12}	Pa	245 – 22367	11306	–
T_1, T_2	°C	30 – 1500, 950 – 1500	765, 1225	–

Table 3.1: Typical values for the parameters in (3.6).

of the participating solids, σ_{12}^{asp} and m_{12}^{asp} are the average height[1] and slope of the surface asperities (i.e., surface microstructures), H_{12} is the microhardness (or, Vickers hardness) of the weaker surface, and p_{12} is the contact pressure. Note that $\dot{q}_{12}^{\text{rad}}$ is also a part of $\dot{q}_{12}^{\text{ct}}$ because the thermal contact is made up of both microstructures that are in touch with each other and the gaps in between.

Using the mean of typical parameter values, as given in Table 3.1, (3.6) yields

$$\dot{q}_{12}^{\text{rad}} \approx 239\text{W}/(\text{Km}^2)(T_1 - T_2) \tag{3.7a}$$

$$\dot{q}_{12}^{\text{ct}} - \dot{q}_{12}^{\text{rad}} \approx 3.31\text{W}/(\text{Km}^2)(T_1 - T_2) \tag{3.7b}$$

$$\frac{\dot{q}_{12}^{\text{ct}} - \dot{q}_{12}^{\text{rad}}}{\dot{q}_{12}^{\text{rad}}} \approx 0.014. \tag{3.7c}$$

In conclusion, it will be accepted that the radiation exchange dominates the heat transfer inside the furnace chamber. For this reason, only radiation exchange will be considered in the following.

Based on the considerations above, the flux terms $\dot{q}^w(T, \boldsymbol{x}, \boldsymbol{u})$ and $\dot{q}^p(T, \boldsymbol{x}, \boldsymbol{u})$ in the boundary conditions (3.5b) and (3.5e) will be formulated. Let Γ^{in} be the surface of the furnace walls Ω^w facing inwards[2] (see Fig. 3.1), with

$$\Gamma^{\text{in}} \subset \partial\Omega^w, \quad \partial\Gamma^{\text{in}} = \partial\Gamma^d. \tag{3.8}$$

The boundary conditions (3.5b) and (3.5e) are specified on $\partial\Omega^p$ and Γ^{in} in the form

$$\begin{aligned}\dot{q}^\kappa(T, \boldsymbol{x}, \boldsymbol{u}) &= \sigma\varepsilon^\kappa T(\boldsymbol{x}, \cdot)^4 - \sigma\varepsilon^p \int_{\partial\Omega^p} K(\Omega^p, \varepsilon^p; \boldsymbol{x}, \boldsymbol{x}') T(\boldsymbol{x}', \cdot)^4 \, \mathrm{d}\boldsymbol{x}' \\ &\quad - \sigma\varepsilon^w \int_{\partial\Gamma^{\text{in}}} K(\Omega^p, \varepsilon^p; \boldsymbol{x}, \boldsymbol{x}') T(\boldsymbol{x}', \cdot)^4 \, \mathrm{d}\boldsymbol{x}' - \sum_{j=1}^{N^u} \frac{u_j}{A_j^h} \int_{\Gamma_j^h} K(\Omega^p, \varepsilon^p; \boldsymbol{x}, \boldsymbol{x}') \, \mathrm{d}\boldsymbol{x}',\end{aligned} \tag{3.9}$$

[1] The literature mostly uses the notions of average height R_a and maximum height R_z of asperities. In this sense, σ_{12}^{asp} would be $(R_{a,1} + R_{a,2})/2$.

[2] The surface Γ^{in} does not include the furnace door Γ^d, which is considered as an adiabatic radiation shield due to its minor influence on the heating of the plates.

with $\kappa = p$ and $\boldsymbol{x} \in \partial\Omega^p$, or $\kappa = w$ and $\boldsymbol{x} \in \Gamma^{\text{in}}$, respectively. Here, ε^w and ε^p are the emissivities of the wall and plate surfaces, respectively, and A_j^h is the surface area of Γ_j^h. The integral kernel $K(\Omega^p, \varepsilon^p; \boldsymbol{x}, \boldsymbol{x}')$ describes the net portion of heat emitted from $\boldsymbol{x}'$ that is absorbed at $\boldsymbol{x}$. It depends on the geometry and properties of the radiation enclosure and therefore changes with Ω^p and ε^p. Moreover, due to energy conservation, it holds that

$$0 \leq K(\Omega^p, \varepsilon^p; \boldsymbol{x}, \boldsymbol{x}') \leq 1 \tag{3.10a}$$

$$\int_{\partial\Omega^p \cup \Gamma^{\text{in}} \cup \Gamma^h} K(\Omega^p, \varepsilon^p; \boldsymbol{x}, \boldsymbol{x}') \, \mathrm{d}\boldsymbol{x} = \text{const.} \tag{3.10b}$$

Note that, if the heater Γ_j^h (currently modeled as a 2D surface) radiates to both sides, this has to be accounted for in A_j^h, K, and the integral over Γ_j^h.

3.1.1.2 Outer Boundary Conditions

The outer boundary Γ^{out} of the furnace walls exchanges heat with the environment via radiation and free convection, and is defined by

$$\Gamma^{\text{out}} = \partial\Omega^w \backslash \Gamma^{\text{in}}. \tag{3.11}$$

Accordingly, the outer boundary condition is given by

$$\dot{q}^w(T, \boldsymbol{x}, \boldsymbol{u}) = \sigma\varepsilon^{\text{out}}\left(T^4 - (T^\infty)^4\right) + \alpha^{\text{out}}(T - T^\infty), \quad \boldsymbol{x} \in \Gamma^{\text{out}}. \tag{3.12}$$

Here, T^∞ is the ambient temperature, i.e., the temperature of the production hall. The symbols ε^{out} and α^{out} denote the emissivity of the steel framework and the heat transfer coefficient due to free convection, respectively. Note that the value for α^{out} can differ between the top, bottom and side walls of the steel framework.

3.1.2 Furnace Model Geometry

As a first step towards a simpler, computationally efficient process model, the heat conduction in the furnace walls is examined in more detail. Assuming a linear, homogeneous, isotropic material, the heat conduction in Ω^w is governed by

$$\rho^w c_p^w \partial_t T = \lambda^w \Delta T, \quad \boldsymbol{x} \in \Omega^w. \tag{3.13a}$$

Furthermore, a constant furnace temperature T^{in} is assumed on the inner surface Γ^{in} of the wall and the outer boundary Γ^{out} is set to the constant temperature T^{out}, such that

$$T|_{\Gamma^{\text{in}}} = T^{\text{in}} = \text{const.}, \quad \boldsymbol{x} \in \Gamma^{\text{in}} \tag{3.13b}$$

$$T|_{\Gamma^{\text{out}}} = T^{\text{out}} = \text{const.}, \quad \boldsymbol{x} \in \Gamma^{\text{out}}. \tag{3.13c}$$

At steady state, i.e., $\partial_t T = 0$, (3.13) can be normalized and rewritten in the form

$$\Delta\xi = 0, \quad \boldsymbol{x} \in \Omega^w \tag{3.14a}$$
$$\xi|_{\Gamma^{\text{in}}} = 1, \quad \boldsymbol{x} \in \Gamma^{\text{in}} \tag{3.14b}$$
$$\xi|_{\Gamma^{\text{out}}} = 0, \quad \boldsymbol{x} \in \Gamma^{\text{out}}, \tag{3.14c}$$

with

$$T = (T^{\text{in}} - T^{\text{out}})\xi + T^{\text{out}}. \tag{3.15}$$

Based on (3.14), a 2D finite-element (FE) model of the furnace cross-section in Fig. 3.1 was implemented in COMSOL MULTIPHYSICS and compared to simpler geometries.

Figure 3.2 shows the considered geometries along with the normalized temperature field ξ. The original cross-section shown in Fig. 3.2a was replaced by the rectangle-based geometry shown in Fig. 3.2b, while the volumes of the chamber and the furnace wall were preserved. In a second step, from Fig. 3.2b to Fig. 3.2c, the wall was further divided into laterally isolated sections, such that each section can be treated as a quasi-1D domain.

It can be seen that the temperature field in the lower half of the wall cross-section changes only to a minor degree from Fig. 3.2a to Fig. 3.2c, while in the upper half of the cross-section, a larger difference is observed. To examine this deviation, the normalized heat flux $\int_{\Gamma^{\text{out}}} \partial_n \xi \, \mathrm{d}s$ out of the system is compared in Table 3.2. Although the outward fluxes of the top, bottom, left and right outer wall surfaces change with the geometry, the difference in the total flux over the outer surface is quite small. The overall energy balance based on the quasi-1D model is therefore expected to be almost identical to the one of the original geometry.

Comparison of $\int \partial_n \xi \, \mathrm{d}s$ on subsets of Γ^{out}					
Subset	Original geom.	Rectangular geom.		Quasi-1D geom.	
Top	1.8484	1.8959	(+2.57%)	2.1650	(+17.13%)
Bottom	3.1402	2.8762	(−8.41%)	2.9355	(−6.52%)
Left/Right	1.3207	1.4576	(+10.37%)	1.2566	(−4.85%)
Total	7.6296	7.6878	(+0.76%)	7.6139	(−0.25%)

Table 3.2: Comparison of different furnace model geometries.

From the results above, it can be concluded that a rectangle-based furnace model geometry with quasi-1D wall sections as in Fig. 3.2c is sufficient to describe the furnace walls.

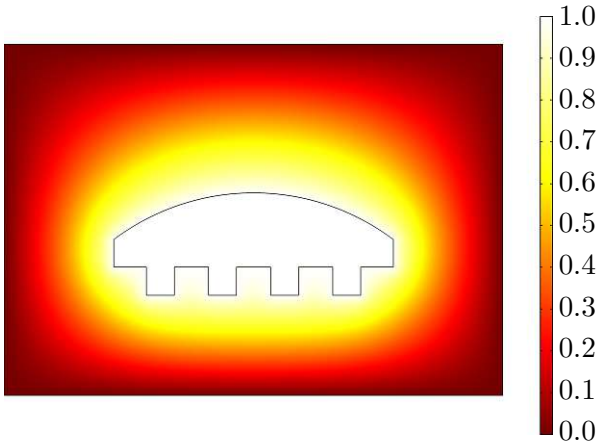

(a) Original geometry.

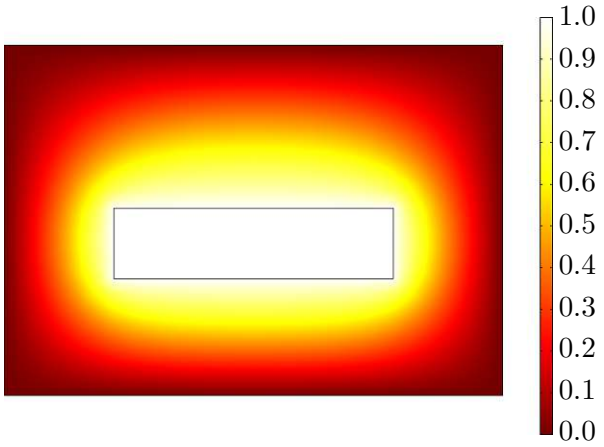

(b) Rectangle-based geometry.

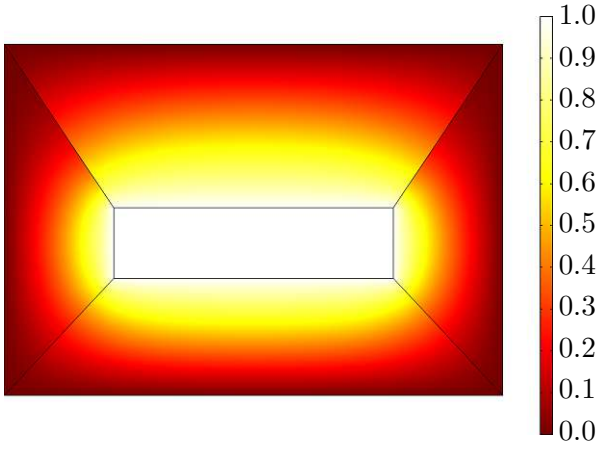

(c) Quasi-1D geometry.

Figure 3.2: Comparison of furnace model geometries: Normalized temperature field $\xi \in [0, 1]$ in the wall cross-sections.

3.2 Model Discretization

For the numerical simulation of the PDE model (3.5) with the boundary conditions (3.9) and (3.12), the model equations can be discretized in space, using FE or finite-volume (FV) methods.

The simplified domain Ω^w shown in Fig. 3.2 is further partitioned into subdomains that arise from the definition of the furnace zones and from the layered structure of the walls. This partitioning suggests a coarse mesh that can be used for fast computation of numerical solutions. The discretized process model is defined separately for the charged and the uncharged furnace.

3.2.1 Meshing Strategy

The geometry simplification shown in Fig. 3.2 is now applied to the entire furnace and the walls are further partitioned into subdomains. The result is depicted in Fig. 3.3.

The walls on each side of the furnace are partitioned in longitudinal direction according to the lengths of the furnace zones. This results in N^w wall sections Ω_i^w with

$$\Omega^w = \bigcup_{i=1}^{N^w} \Omega_i^w, \quad \partial\Omega_i^w \cap \Gamma^{\text{in}} \neq \emptyset, \quad \partial\Omega_i^w \cap \Gamma^{\text{out}} \neq \emptyset. \tag{3.16}$$

Each wall section Ω_i^w is set adiabatic on its lateral boundaries, i.e.,

$$\partial_n T = 0, \quad \boldsymbol{x} \in \partial\Omega_i^w \backslash \partial\Omega^w, \tag{3.17}$$

and thus describes a quasi-1D domain, in the sense that all the heat flux goes from the chamber boundary Γ^{in} to the outer boundary Γ^{out}.

Each wall section Ω_i^w is further partitioned into N_i^w subdomains, according to the (average) layer thickness of each wall material

$$\Omega_i^w = \bigcup_{j=1}^{N_i^w} \Omega_{i,j}^w. \tag{3.18}$$

Each subdomain $\Omega_{i,j}^w$ holds one homogeneous material with the density $\rho_{i,j}^w$, the specific heat capacity $c_{p,i,j}^w$, and the (nominal) thermal conductivity $\lambda_{i,j}^w$. The temperature field in the wall is governed by

$$\rho_{i,j}^w c_{p,i,j}^w(T)\partial_t T = \boldsymbol{\nabla} \cdot \left(\eta \lambda_{i,j}^w(T) \boldsymbol{\nabla} T\right), \quad \boldsymbol{x} \in \Omega_{i,j}^w, \quad t > 0 \tag{3.19a}$$

$$-\eta \lambda_{i,j}^w(T)\partial_n T = \dot{q}^w(T, \boldsymbol{x}, \boldsymbol{u}), \quad \boldsymbol{x} \in \partial\Omega_{i,j}^w \cap \partial\Omega^w, \quad t > 0 \tag{3.19b}$$

$$T|_{\partial\Omega_{i,j}^w} = T|_{\partial\Omega_{i,k}^w}, \quad \boldsymbol{x} \in \partial\Omega_{i,j}^w \cap \partial\Omega_{i,k}^w, \quad t > 0 \tag{3.19c}$$

$$-\eta \lambda_{i,j}^w(T)\, \partial_n T|_{\partial\Omega_{i,j}^w} = \eta \lambda_{i,k}^w(T)\, \partial_n T|_{\partial\Omega_{i,k}^w}, \quad \boldsymbol{x} \in \partial\Omega_{i,j}^w \cap \partial\Omega_{i,k}^w, \quad t > 0 \tag{3.19d}$$

$$\partial_n T|_{\partial\Omega_{i,j}^w} = 0, \quad \text{else}, \quad t > 0 \tag{3.19e}$$

$$T|_{t=0} = T_0, \quad \boldsymbol{x} \in \Omega_{i,j}^w, \quad t = 0 \tag{3.19f}$$

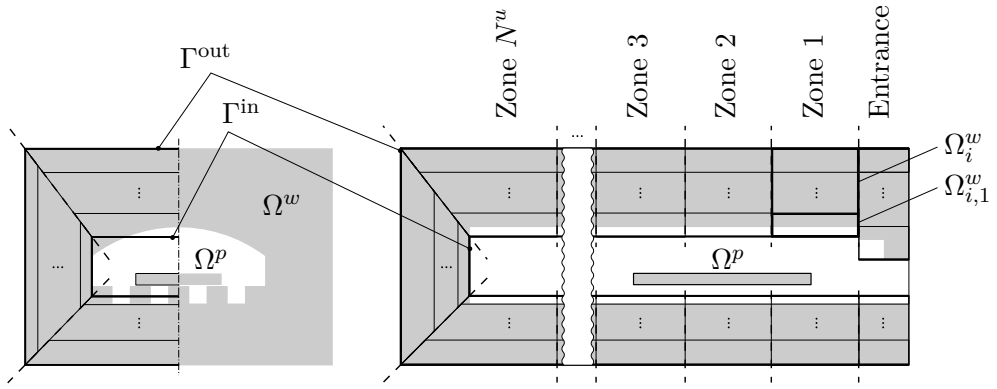

Figure 3.3: Cross- and longitudinal sections of the furnace including the zones, wall sections Ω^w_i, and layers $\Omega^w_{i,j}$.

and the plate temperature is subject to

$$\rho^p c_p^p \partial_t T = \boldsymbol{\nabla} \cdot (\lambda^p(T) \boldsymbol{\nabla} T), \quad \boldsymbol{x} \in \Omega^p, \quad t > 0 \tag{3.19g}$$
$$-\lambda^p(T) \partial_n T = \dot{q}^p(T, \boldsymbol{x}, \boldsymbol{u}), \quad \boldsymbol{x} \in \partial\Omega^p, \quad t > 0 \tag{3.19h}$$
$$T|_{t=0} = T_0, \quad \boldsymbol{x} \in \Omega^p, \quad t = 0, \tag{3.19i}$$

with $\dot{q}^w$ and $\dot{q}^p$ according to (3.9) and (3.12).

3.2.2 Discretized Process Model

For the numerical solution of (3.19) with the boundary conditions (3.9) and (3.12), the mesh given by $\Omega^w_{i,j}$, $j = 1, \ldots, N^w_i$, $i = 1, \ldots, N^w$, can be refined, if necessary, and passed to an FE or FV solver. The ODE system resulting from the spatial discretization has the structure

$$\boldsymbol{M}(\boldsymbol{T}) \frac{\mathrm{d}}{\mathrm{d}t} \boldsymbol{T} = \begin{cases} \boldsymbol{A}(\eta; \boldsymbol{T}) \boldsymbol{T} + \boldsymbol{R}(\boldsymbol{T}) + \boldsymbol{B}\boldsymbol{u} + \boldsymbol{B}^d \boldsymbol{d}, & \text{if } \Omega^p = \emptyset \quad \text{(empty)} \\ \boldsymbol{A}(\eta; \boldsymbol{T}) \boldsymbol{T} + \boldsymbol{R}(\varepsilon^p; \boldsymbol{T}) + \boldsymbol{B}(\varepsilon^p) \boldsymbol{u} + \boldsymbol{B}^d \boldsymbol{d}, & \text{if } \Omega^p \neq \emptyset \quad \text{(charged)} \end{cases} \tag{3.20a}$$

$$\boldsymbol{T}(0) = \boldsymbol{T}_0 \tag{3.20b}$$

for the empty and the charged furnace, respectively. Here, $\boldsymbol{T}$ represents the system state, i.e., in the case of FE and FV methods, the temperatures at certain control points. Accordingly, $\boldsymbol{T}_0$ denotes the initial state at $t = 0$. The disturbance input $\boldsymbol{d} = \begin{bmatrix} T^\infty & (T^\infty)^4 \end{bmatrix}^{\mathrm{T}}$ describes the influence of the ambient temperature T^∞. To illustrate the transition from the PDE model (3.19) to the process model (3.20), the FV method is applied to the PDE model in Appendix A.

3.3 Temperature Sensors and Control Loop

In addition to (3.20), if measurements $\boldsymbol{y}$ of the (discretized) temperature field $\boldsymbol{T}$ are taken, they can be expressed in the form

$$\boldsymbol{y} = \boldsymbol{C}\boldsymbol{T}. \tag{3.21}$$

In this work, temperature measurements are provided by thermocouples and two-color pyrometers. In each zone of the furnace chamber, a thermocouple is mounted on the surface of the side walls. The measured side wall temperatures

$$\boldsymbol{y}^w = \boldsymbol{C}^w\boldsymbol{T} \tag{3.22}$$

are referred to as the furnace temperature or zone temperatures. In the considered chamber furnace, the furnace temperature is controlled to an operating point r by decoupled proportional-integral (PI) controllers. The furnace temperature controller thus has the form

$$\boldsymbol{e}^w(t) = \mathbf{1}r(t) - \boldsymbol{y}^w(t) \tag{3.23a}$$

$$\frac{\mathrm{d}}{\mathrm{d}t}\boldsymbol{x}^{\mathrm{PI}}(t) = \boldsymbol{K}^I\boldsymbol{e}^w(t), \qquad \boldsymbol{x}^{\mathrm{PI}}(0) = \mathbf{0} \tag{3.23b}$$

$$\boldsymbol{u}(t) = \max\{\mathbf{0}, \boldsymbol{x}^{\mathrm{PI}}(t) + \boldsymbol{K}^P\boldsymbol{e}^w(t)\}, \tag{3.23c}$$

where the matrices $\boldsymbol{K}^I$ and $\boldsymbol{K}^P$ are positive definite and diagonal, since the controllers for the furnace zones are decoupled.

During normal operation, the plate temperature can only be measured by a two-color pyrometer when the plate is charged into or discharged from the furnace. In the measurement process, the focal point of the pyrometer moves along a line on the bottom surface of the plate. From this line measurement, a scalar value y^p is computed, which is referred to as the charge and discharge temperature, respectively. The pyrometer measurement is governed by

$$y^p = (\boldsymbol{c}^p)^{\mathrm{T}}\boldsymbol{T}, \tag{3.24}$$

where $\boldsymbol{c}^p \neq \mathbf{0}$ only when the furnace switches between the charged and empty configurations.

Finally, in order to identify and validate the process model (3.20), a test plate was equipped with a recording box and thermocouples to measure the plate temperature during the heating process in the furnace. In this measurement campaign, the temperature y^m in the center of the plate was captured

$$y^m = (\boldsymbol{c}^m)^{\mathrm{T}}\boldsymbol{T}. \tag{3.25}$$

The output (3.21) can now be summarized as

$$\boldsymbol{y} = \begin{bmatrix} \boldsymbol{y}^w \\ y^p \\ y^m \end{bmatrix} = \begin{bmatrix} \boldsymbol{C}^w \\ (\boldsymbol{c}^p)^{\mathrm{T}} \\ (\boldsymbol{c}^m)^{\mathrm{T}} \end{bmatrix} \boldsymbol{T} = \boldsymbol{C}\boldsymbol{T}. \tag{3.26}$$

A diagram of the temperature-controlled process model is shown in Fig. 3.4.

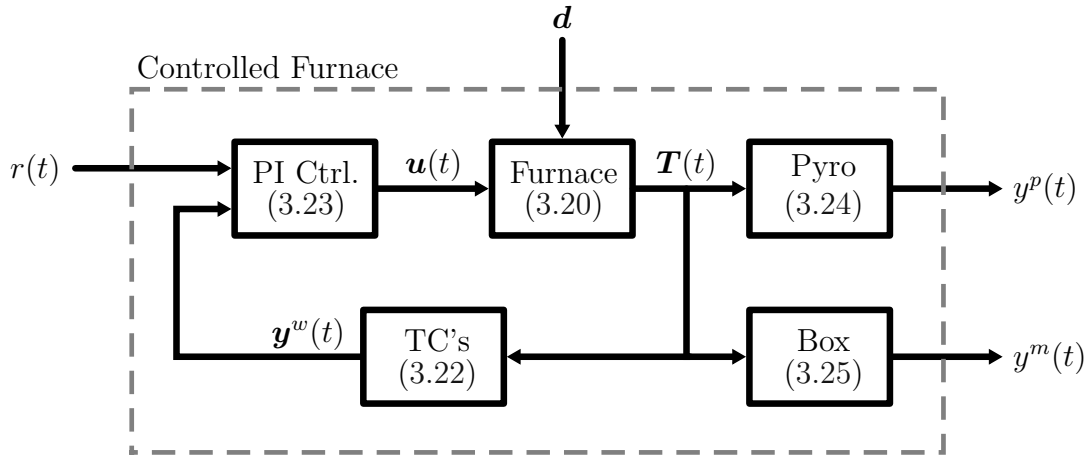

Figure 3.4: Temperature control loop of the chamber furnace. TC's: Thermocouples.

3.4 Model Parameter Identification

The generally unknown parameters η and ε^p have a significant influence on the temperature dynamics and the heating times. The former parameter η describes the influence of the hydrogen atmosphere and affects the heat exchange throughout the furnace walls. The latter parameter ε^p directly influences the heat exchange between the plate and the surrounding walls and may deviate significantly from its nominal value depending on the surface condition of the plate. Therefore, both η and ε^p have to be identified from measurement data.

While the value of η is specific to the respective furnace, the value of ε^p changes from plate to plate. It therefore makes sense to identify η only once for the process model, but the value of ε^p has to be adjusted individually for each plate.

In the following, the parameter η is identified using measurement data from the uncharged furnace in steady-state operation. The empty process model is subsequently validated using a recorded wall temperature profile. An experimental identification of the parameter ε^p and the subsequent validation of the (charged) process model are performed at the end of this section. The accuracy requirement for the identified model due to the used discretization method, namely FV with the meshing shown in Section 3.2.1, is that the maximum error between the measurement and the model should be within a tolerance range of ± 15°C.

3.4.1 Identification of the Parameter η

Following (3.19), the steady-state wall temperature (i.e., $\partial_t T = 0$) of the empty furnace is determined by the parameter η and the steady-state boundary conditions. A choice of $\eta > 1$ is in accordance with the increased thermal conductivity of the hydrogen atmosphere in the furnace compared to air.

A set of four operating points $\left\{ [r_j^{\mathrm{id}}, (\boldsymbol{u}_j^{\mathrm{id}})^{\mathrm{T}}] \middle| j = 1, \ldots, 4 \right\}$ is used to identify η

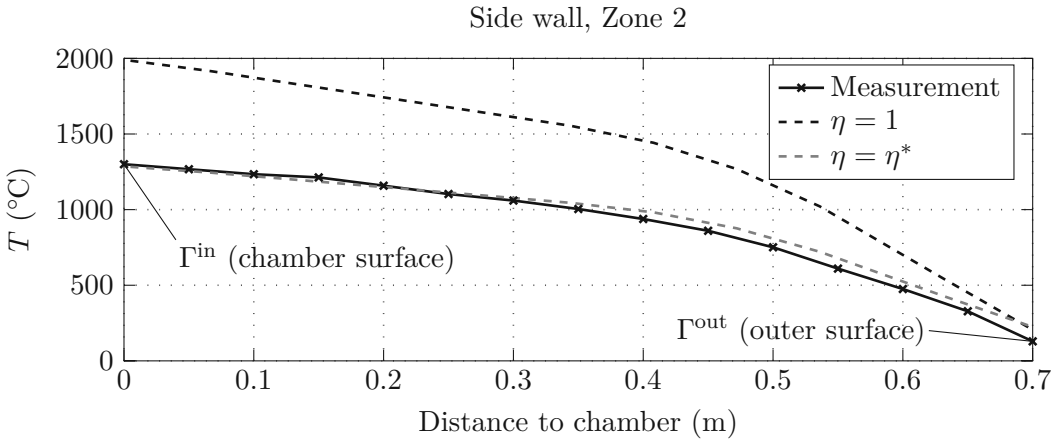

Figure 3.5: Measured and simulated wall temperature profiles for different values of η and the setpoint temperature $r = 1300°C$.

for the empty process model ($\Omega^p = \emptyset$). The respective reference temperatures r_j^{id} of the control loops range from 950°C to 1500°C and $\boldsymbol{u}_j^{\mathrm{id}}$ are the respective measured steady-state power inputs. The identification problem for η reads as

$$\min_{\eta>1} \sum_{j=1}^{4} \left\| \boldsymbol{y}_s^w|_{\boldsymbol{u}_s=\boldsymbol{u}_j^{\mathrm{id}}} - \mathbf{1} r_j^{\mathrm{id}} \right\|_2^2 \tag{3.27a}$$

$$\text{s.t.} \quad \mathbf{0} = \boldsymbol{A}(\eta; \boldsymbol{T}_s)\boldsymbol{T}_s + \boldsymbol{R}(\boldsymbol{T}_s) + \boldsymbol{B}\boldsymbol{u}_s + \boldsymbol{B}^d\boldsymbol{d}, \quad \Omega^p = \emptyset \quad \text{(empty)} \tag{3.27b}$$

$$\boldsymbol{y}_s^w = \boldsymbol{C}^w\boldsymbol{T}_s, \tag{3.27c}$$

with the steady-state inputs $\boldsymbol{u}_s$, temperatures $\boldsymbol{T}_s$, and outputs $\boldsymbol{y}_s^w$.

The optimal value of η is $\eta^* = 2.08$, which shows that the thermal insulation capability of the used ceramics is halved in a hydrogen atmosphere. For comparison, the simulated wall temperature profiles for $\eta = 1$ and $\eta = \eta^*$ are shown in Fig. 3.5. Note that, due to the large heat capacity of the wall, the temperature dynamics of the wall layers are extremely slow. Therefore, any residual temperature errors in the outer layers of the wall only have negligible influence on the transient dynamics of the heating process. Therefore, the identified value η^* can also be used for the charged process model.

The steady-state solution $\boldsymbol{T}_s$ of (3.27) can be decomposed according to

$$\boldsymbol{T}_s = \begin{bmatrix} \boldsymbol{T}_s^w \\ \boldsymbol{T}_s^p \end{bmatrix}, \tag{3.28}$$

where $\boldsymbol{T}_s^w$ represents the wall temperatures and $\boldsymbol{T}_s^p$ ($= \mathbf{0}$ for the empty furnace) represents the plate temperatures. The solution for $\boldsymbol{T}_s^w$ will be used as the initial condition for the walls when a plate is charged into the furnace.

3.4.2 Identification of the Plate Emissivity ε^p

For the identification of ε^p and the subsequent validation of the charged furnace model (3.20), a test plate incorporating a thermocouple measurement was heated in the furnace. To this end, a recording box was mounted on a sintered molybdenum plate, and a thermocouple was attached in a borehole to the plate center. In two consecutive reheating cycles, the plate was reheated from room temperature to two different setpoint temperatures. Table 3.3 lists the parameters of the two reheating cycles.

Parameter		Values	
Name	Symbol	Cycle 1	Cycle 2
Setpoint temp.	r	950°C	1050°C
Wall parameter	η	η^*	
Plate material	–	Mo	
Plate surface	–	Oxidized	
Plate length	l_x^p	1065mm	
Plate width	l_y^p	560mm	
Plate thickness	l_z^p	120mm	
Plate mass	m^p	780kg	
Plate initial temp.	T_0^p	30°C	
Heating powers	$\boldsymbol{u}(t)$	$\boldsymbol{u}_1^m(t)$	$\boldsymbol{u}_2^m(t)$
Plate temp. measurement	$y^m(t)$	$y_1^m(t)$	$y_2^m(t)$

Table 3.3: Parameters for the identification of the plate emissivity ε^p and the validation of the charged furnace model (3.20).

The recorded power inputs and sensor signals of the two cycles are denoted by $\boldsymbol{u}_j^m(t)$ and $y_j^m(t)$, $j = 1, 2$, respectively. The total power $u_j^m = \mathbf{1} \cdot \boldsymbol{u}_j^m$ and the sensor signal $y_j^m(t)$ are depicted in Fig. 3.6.

The identification problem for ε^p reads as

$$\min_{\varepsilon^p \in (0;1)} \int_{t_0}^{t_1} (e_1^m)^2 \, \mathrm{d}t \tag{3.29a}$$

$$\text{s.t.} \quad \boldsymbol{M}(\boldsymbol{T}) \frac{\mathrm{d}}{\mathrm{d}t} \boldsymbol{T} = \boldsymbol{A}(\eta; \boldsymbol{T}) \boldsymbol{T} + \boldsymbol{R}(\varepsilon^p; \boldsymbol{T}) + \boldsymbol{B}(\varepsilon^p) \boldsymbol{u} + \boldsymbol{B}^d \boldsymbol{d} \tag{3.29b}$$

$$\boldsymbol{T}(0) = \begin{bmatrix} \boldsymbol{T}_s^w \\ \mathbf{1} T^\infty \end{bmatrix} \tag{3.29c}$$

$$y^m = (\boldsymbol{c}^m)^{\mathrm{T}} \boldsymbol{T} \tag{3.29d}$$

$$\eta = \eta^* \tag{3.29e}$$

$$\boldsymbol{u} = \boldsymbol{u}_1^m \tag{3.29f}$$

$$e_1^m = y^m - y_1^m, \tag{3.29g}$$

where the previously-identified value η^* is used for η and $\boldsymbol{T}_s^w$ is the steady-state solution for the wall temperature from (3.27) and (3.28). For the considered plate, the emissivity value $\varepsilon^{p*} = 0.58$ was identified. Figure 3.6 compares the simulated and the measured temperatures at the plate center, and the error between the simulation and the measurement. The maximum error is 8.8°C.

To validate the estimated emissivity ε^{p*} together with the charged furnace model (3.20), cycle 2 of Table 3.3 was simulated in the form

$$\boldsymbol{M}(\boldsymbol{T}) \frac{\mathrm{d}}{\mathrm{d}t} \boldsymbol{T} = \boldsymbol{A}(\eta^*; \boldsymbol{T}) \boldsymbol{T} + \boldsymbol{R}(\varepsilon^{p*}; \boldsymbol{T}) + \boldsymbol{B}(\varepsilon^{p*}) \boldsymbol{u}_2^m + \boldsymbol{B}^d \boldsymbol{d} \tag{3.30a}$$

$$\boldsymbol{T}(0) = \begin{bmatrix} \boldsymbol{T}_s^w \\ \mathbf{1} T^\infty \end{bmatrix} \tag{3.30b}$$

$$y^m = (\boldsymbol{c}^m)^{\mathrm{T}} \boldsymbol{T} \tag{3.30c}$$

and compared to the recorded measurement y_2^m by the error term

$$e_2^m = y^m - y_2^m. \tag{3.30d}$$

The results of the model validation are shown in Fig. 3.6. The error between the simulation model and the measurement data is smaller than 12°C and thus within the desired tolerance range of ±15°C, which was specified at the beginning of this section.

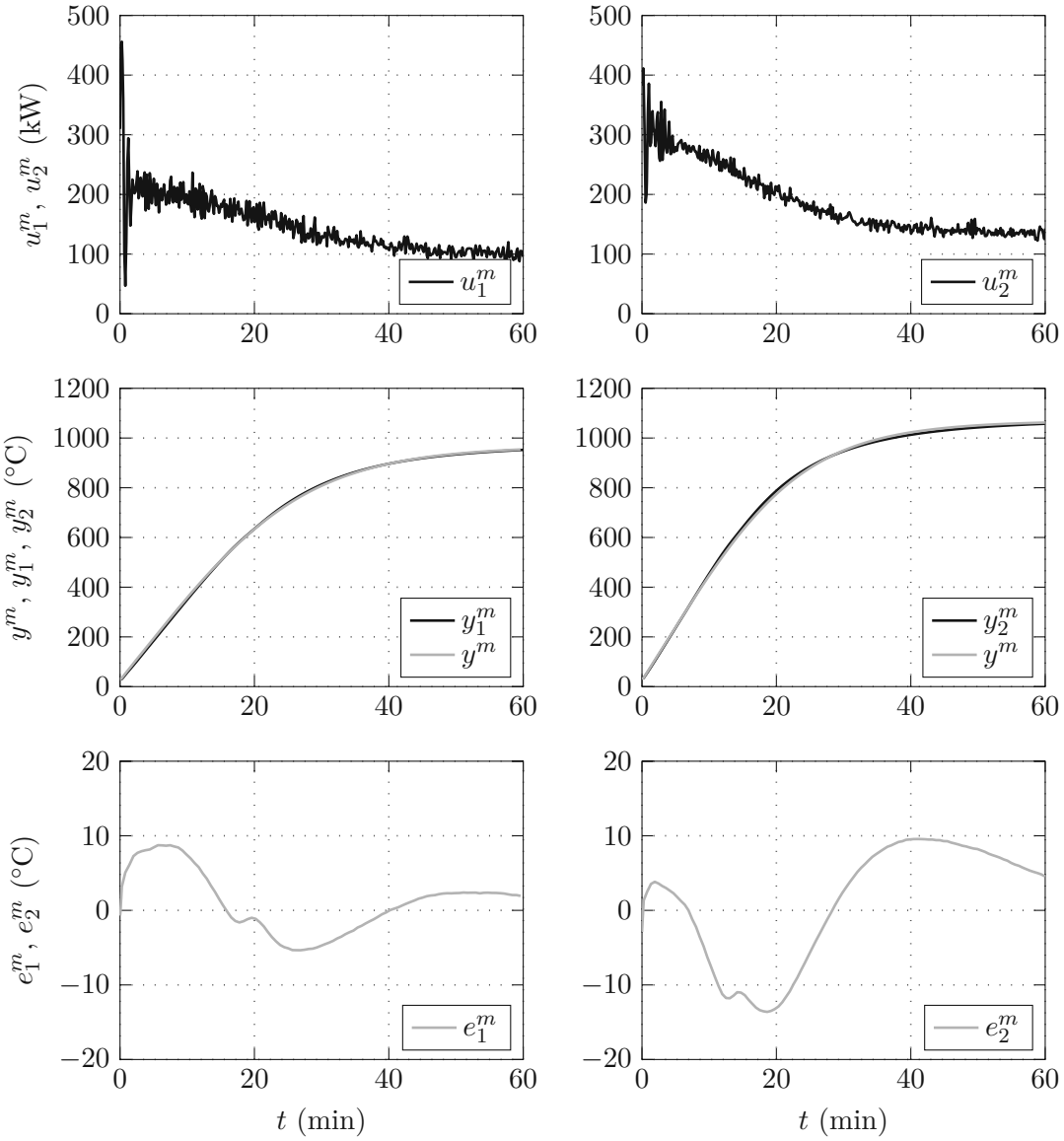

Figure 3.6: Identification of ε^p and validation of the model (3.20).

CHAPTER 4

Model Reduction and Analysis

In order to calculate the optimal reheating time for a product in real time, in this chapter, the process model (3.20) is reduced to a minimal model that features very low computational costs. To this end, a representative reheating trajectory is simulated and analyzed by means of Proper Orthogonal Decomposition (POD), see, e.g., [36]. It is shown that the evolution of $y^p(t)$ is well represented by the dominant POD mode of the plate. Based on this observation, a very simple yet accurate model of first order is derived.

The model reduction based on POD is already published in [56]. Large parts of the derivation of the simple first-order model are published in [57].

4.1 Proper Orthogonal Decomposition

In order to reduce the order of (3.20), a POD is performed on the charged process model and the contributions of each POD mode to the pyrometer output (3.24) are analyzed.

Chamber furnace		
Parameter	Value	Unit
r	1300	°C
η	η^*	–

Heavy plate		
Parameter	Value	Unit
Material	Mo	–
l_x^p	1065	mm
l_y^p	560	mm
l_z^p	120	mm
m^p	780	kg
T_0^p	30	°C
ε^p	0.25	–

Table 4.1: Parameters for a representative reheating trajectory.

4.1.1 Computation of the POD Modes

Consider the charged process model with temperature control (cf. Fig. 3.4),

$$\boldsymbol{M}(\boldsymbol{T})\frac{\mathrm{d}}{\mathrm{d}t}\boldsymbol{T} = \boldsymbol{A}(\eta;\boldsymbol{T})\boldsymbol{T} + \boldsymbol{R}(\varepsilon^p;\boldsymbol{T}) + \boldsymbol{B}(\varepsilon^p)\boldsymbol{u} + \boldsymbol{B}^d\boldsymbol{d}, \quad \text{(charged)} \tag{4.1a}$$

$$\boldsymbol{T}(0) = \begin{bmatrix} \boldsymbol{T}_s^w \\ \mathbf{1}T_0^p \end{bmatrix} \tag{4.1b}$$

$$y^p = (\boldsymbol{c}^p)^{\mathrm{T}}\boldsymbol{T} \tag{4.1c}$$

$$\boldsymbol{y}^w = \boldsymbol{C}^w\boldsymbol{T} \tag{4.1d}$$

$$\boldsymbol{e}^w = \mathbf{1}r - \boldsymbol{y}^w \tag{4.1e}$$

$$\frac{\mathrm{d}}{\mathrm{d}t}\boldsymbol{x}^{\mathrm{PI}} = \boldsymbol{K}^I\boldsymbol{e}^w \tag{4.1f}$$

$$\boldsymbol{u} = \boldsymbol{x}^{\mathrm{PI}} + \boldsymbol{K}^P\boldsymbol{e}^w, \tag{4.1g}$$

with the known parameter values η and ε^p. The steady-state solutions $\boldsymbol{T}_s^0$ and $y_s^{p,0}$ of (4.1a) and (4.1c) for zero input ($\boldsymbol{u} \equiv \mathbf{0}$) are calculated from[1]

$$\mathbf{0} = \boldsymbol{A}(\eta;\boldsymbol{T}_s^0)\boldsymbol{T}_s^0 + \boldsymbol{R}(\varepsilon^p;\boldsymbol{T}_s^0) + \boldsymbol{B}^d\boldsymbol{d}, \quad \text{(charged)} \tag{4.2a}$$

$$y_s^{p,0} = (\boldsymbol{c}^p)^{\mathrm{T}}\boldsymbol{T}_s^0. \tag{4.2b}$$

In the following, the system dynamics relative to $\boldsymbol{T}_s^0$ will be examined based on a representative reheating trajectory. The parameters for this reheating trajectory are listed in Table 4.1. Using the temperature-controlled process model (4.1), $\boldsymbol{T}(t)$ is simulated and snapshots are taken at a sampling time τ, which results in the data matrix

$$\boldsymbol{D} = \begin{bmatrix} \boldsymbol{T}(0) - \boldsymbol{T}_s^0 & \boldsymbol{T}(\tau) - \boldsymbol{T}_s^0 & \boldsymbol{T}(2\tau) - \boldsymbol{T}_s^0 & \dots \end{bmatrix} = \begin{bmatrix} \boldsymbol{D}^w \\ \boldsymbol{D}^p \end{bmatrix}. \tag{4.3}$$

[1] In the simplest case, $\boldsymbol{T}_s^0 = \mathbf{1}T^\infty$ and $y_s^{p,0} = T^\infty$.

A decomposition of $\boldsymbol{D}$ into the submatrices $\boldsymbol{D}^w$ and $\boldsymbol{D}^p$ is assumed, which refer to the wall and plate temperatures, respectively. From the recorded snapshot data in $\boldsymbol{D}^w$ (and $\boldsymbol{D}^p$), the POD modes $\boldsymbol{v}_j^w$ (and $\boldsymbol{v}_j^p$) are derived by a singular value decomposition. If the number of columns of each data matrix exceeds the number of rows, the POD modes of the furnace wall and plate result from[2]

$$\boldsymbol{D}^w(\boldsymbol{D}^w)^{\mathrm{T}}\boldsymbol{v}_j^w = \boldsymbol{v}_j^w\mu_j^w, \qquad \boldsymbol{v}_i^w \cdot \boldsymbol{v}_j^w = \begin{cases} 1, & i=j \\ 0, & \text{else,} \end{cases} \qquad \mu_1^w \geq \mu_2^w \geq \cdots \geq 0 \tag{4.4a}$$

$$\boldsymbol{D}^p(\boldsymbol{D}^p)^{\mathrm{T}}\boldsymbol{v}_j^p = \boldsymbol{v}_j^p\mu_j^p, \qquad \boldsymbol{v}_i^p \cdot \boldsymbol{v}_j^p = \begin{cases} 1, & i=j \\ 0, & \text{else,} \end{cases} \qquad \mu_1^p \geq \mu_2^p \geq \cdots \geq 0. \tag{4.4b}$$

For the plate subsystem, the POD modes $\boldsymbol{v}_1^p, \ldots, \boldsymbol{v}_5^p$ are shown as plate temperature profiles in Fig. 4.1. The state vector $\boldsymbol{T}$ can now be approximated according to

$$\boldsymbol{T} \approx \widetilde{\boldsymbol{V}}\widetilde{\boldsymbol{T}} + \boldsymbol{T}_s^0, \quad \widetilde{\boldsymbol{V}} = \begin{bmatrix} \widetilde{\boldsymbol{V}}^w & \widetilde{\boldsymbol{V}}^p \end{bmatrix}, \quad \widetilde{\boldsymbol{V}}^w = \begin{bmatrix} \widetilde{\boldsymbol{v}}_1^w & \widetilde{\boldsymbol{v}}_2^w & \ldots \end{bmatrix}, \quad \widetilde{\boldsymbol{v}}_j^w = \begin{bmatrix} \boldsymbol{v}_j^w \\ \boldsymbol{0} \end{bmatrix} \tag{4.5a}$$

$$\widetilde{\boldsymbol{V}}^p = \begin{bmatrix} \widetilde{\boldsymbol{v}}_1^p & \widetilde{\boldsymbol{v}}_2^p & \ldots \end{bmatrix}, \quad \widetilde{\boldsymbol{v}}_j^p = \begin{bmatrix} \boldsymbol{0} \\ \boldsymbol{v}_j^p \end{bmatrix}, \tag{4.5b}$$

where the columns $\widetilde{\boldsymbol{v}}_j^w$ and $\widetilde{\boldsymbol{v}}_j^p$ of $\widetilde{\boldsymbol{V}}$ describe the POD modes of the wall and plate, and $\widetilde{\boldsymbol{V}}^{\mathrm{T}}\widetilde{\boldsymbol{V}} = \boldsymbol{I}$. The reduced state $\widetilde{\boldsymbol{T}}$ denotes the mode weights.

4.1.2 Reduced-Order Model

The POD-reduced model is given by

$$\widetilde{\boldsymbol{M}}(\widetilde{\boldsymbol{T}})\frac{\mathrm{d}}{\mathrm{d}t}\widetilde{\boldsymbol{T}} = \widetilde{\boldsymbol{A}}(\widetilde{\boldsymbol{T}})\widetilde{\boldsymbol{T}} + \widetilde{\boldsymbol{A}}'(\widetilde{\boldsymbol{T}})\boldsymbol{T}_s^0 + \widetilde{\boldsymbol{R}}(\widetilde{\boldsymbol{T}}) + \widetilde{\boldsymbol{B}}\boldsymbol{u} \tag{4.6a}$$

$$\widetilde{\boldsymbol{T}}(0) = \widetilde{\boldsymbol{V}}^{\mathrm{T}}(\boldsymbol{T}(0) - \boldsymbol{T}_s^0) \tag{4.6b}$$

$$\widetilde{y}^p = y^p - y_s^{p,0} \approx (\boldsymbol{c}^p)^{\mathrm{T}}\widetilde{\boldsymbol{V}}\widetilde{\boldsymbol{T}}, \tag{4.6c}$$

with

$$\widetilde{\boldsymbol{M}}(\widetilde{\boldsymbol{T}}) = \widetilde{\boldsymbol{V}}^{\mathrm{T}}\boldsymbol{M}(\widetilde{\boldsymbol{V}}\widetilde{\boldsymbol{T}} + \boldsymbol{T}_s^0)\widetilde{\boldsymbol{V}} \tag{4.6d}$$

$$\widetilde{\boldsymbol{A}}(\widetilde{\boldsymbol{T}}) = \widetilde{\boldsymbol{V}}^{\mathrm{T}}\boldsymbol{A}(\eta; \widetilde{\boldsymbol{V}}\widetilde{\boldsymbol{T}} + \boldsymbol{T}_s^0)\widetilde{\boldsymbol{V}} \tag{4.6e}$$

$$\widetilde{\boldsymbol{A}}'(\widetilde{\boldsymbol{T}}) = \widetilde{\boldsymbol{V}}^{\mathrm{T}}\Big(\boldsymbol{A}(\eta; \widetilde{\boldsymbol{V}}\widetilde{\boldsymbol{T}} + \boldsymbol{T}_s^0) - \boldsymbol{A}(\eta; \boldsymbol{T}_s^0)\Big) \tag{4.6f}$$

$$\widetilde{\boldsymbol{R}}(\widetilde{\boldsymbol{T}}) = \widetilde{\boldsymbol{V}}^{\mathrm{T}}\boldsymbol{R}(\varepsilon^p; \widetilde{\boldsymbol{V}}\widetilde{\boldsymbol{T}} + \boldsymbol{T}_s^0) - \widetilde{\boldsymbol{V}}^{\mathrm{T}}\boldsymbol{R}(\varepsilon^p; \boldsymbol{T}_s^0) \tag{4.6g}$$

$$\widetilde{\boldsymbol{B}} = \widetilde{\boldsymbol{V}}^{\mathrm{T}}\boldsymbol{B}(\varepsilon^p). \tag{4.6h}$$

[2] Otherwise, if the number of rows of the data matrix exceeds the number of columns, the POD modes have to be computed like in [66].

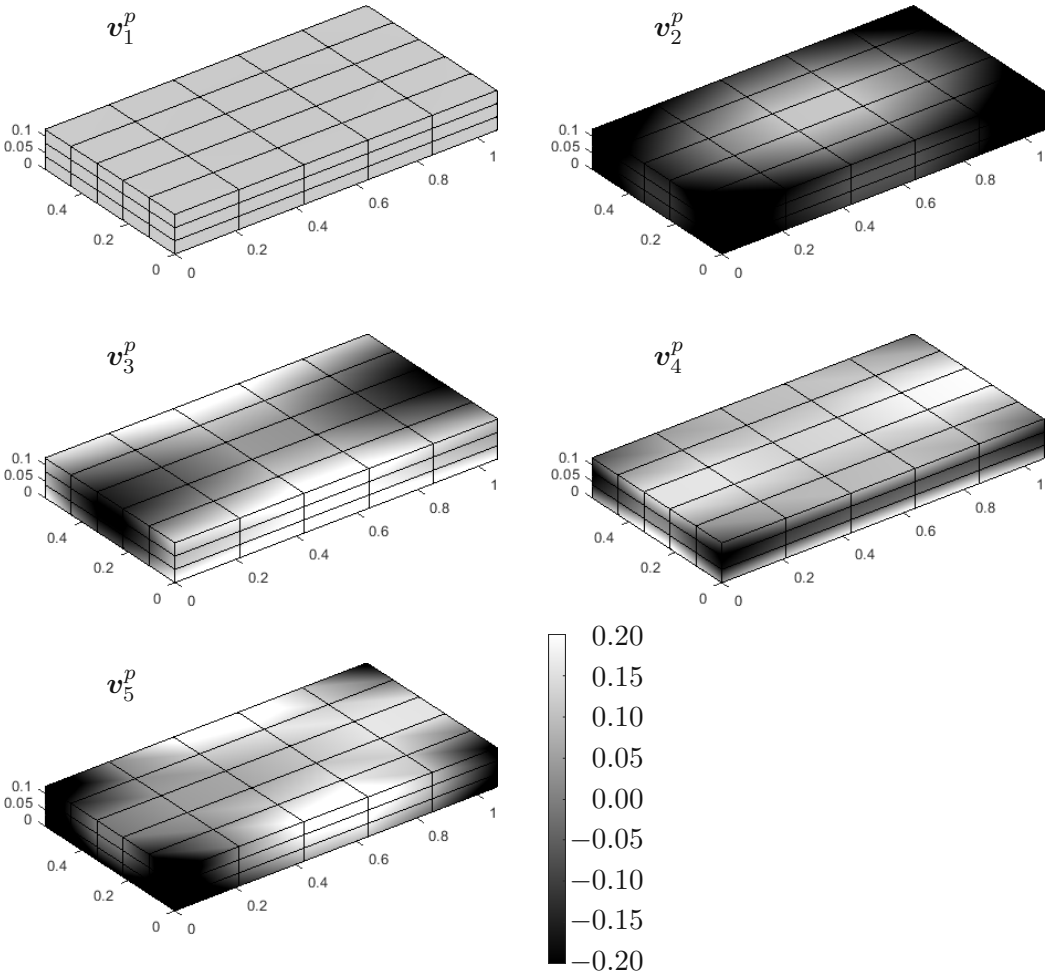

Figure 4.1: Plate temperature profiles corresponding to the POD mode shapes $\boldsymbol{v}_1^p, \ldots, \boldsymbol{v}_5^p$ of the plate.

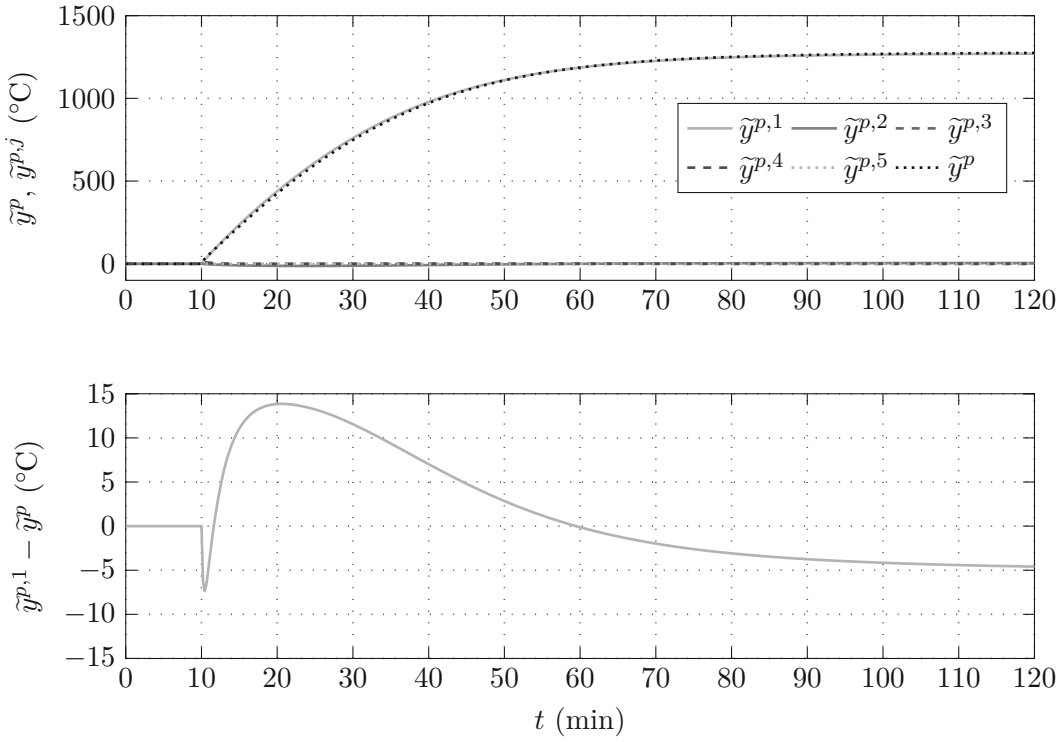

Figure 4.2: Comparison of the (reduced) pyrometer signal $\widetilde{y}^p(t)$ and contributions $\widetilde{y}^{p,j}(t)$ of the distinct POD modes.

The knowledge of η and ε^p is necessary to calculate $\boldsymbol{T}_s^0$ and $\widetilde{\boldsymbol{V}}$. Additionally, $\widetilde{\boldsymbol{V}}$ can change depending on the geometry of the plate. In the real production plant, the plate dimensions can vary greatly.

A pre-calculation of all possible values for $\boldsymbol{T}_s^0$ and $\widetilde{\boldsymbol{V}}$ would entail a large computational effort. The reduced model (4.6) will therefore not be used directly. The plate exit temperature is determined using the pyrometer output (3.24). Thus, it makes sense to further analyze the contributions of the POD modes $\boldsymbol{v}_j^p$ to the signal $\widetilde{y}^p(t)$ according to (4.6c).

4.1.3 Contributions to the Pyrometer Output

The output $\widetilde{y}^p$ from (4.6c) can be decomposed into the contributions $\widetilde{y}^{p,j}$ of each POD mode,

$$\widetilde{y}^p(t) = \widetilde{y}^{p,1}(t) + \widetilde{y}^{p,2}(t) + \dots \tag{4.7a}$$

$$\widetilde{y}^{p,j}(t) = (\boldsymbol{c}^p)^{\mathrm{T}} \widetilde{\boldsymbol{v}}_j^p (\widetilde{\boldsymbol{v}}_j^p)^{\mathrm{T}} (\boldsymbol{T}(t) - \boldsymbol{T}_s^0), \quad j = 1, 2, \dots \tag{4.7b}$$

For the recorded trajectory in (4.3), the signal $\widetilde{y}^p(t)$ and the modal contributions $\widetilde{y}^{p,j}(t)$ are shown in Fig. 4.2. It can be seen that $\widetilde{y}^{p,1}(t)$ resembles the signal $\widetilde{y}^p(t)$ with high quality throughout the heating process. In fact, the error between

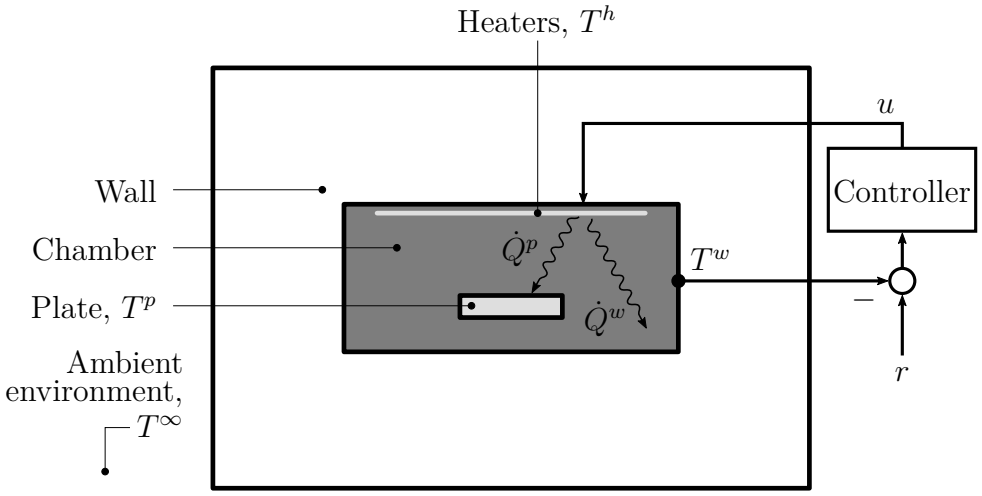

Figure 4.3: Batch-type reheating furnace with temperature control loop.

$\widetilde{y}^{p,1}(t)$ and $\widetilde{y}^p(t)$ does not exceed 14°C during the transient phase and is within ±5°C at steady state. Based on this, we will derive a minimal model that directly describes the plate dynamics in the mode $\boldsymbol{v}_1^p$ (for any combination of parameter values).

4.2 Minimal Model

In the previous section, it was pointed out that the model order reduction by POD entails a high computational effort, because the system parameters vary on a large scale and affect the POD mode shapes. On the other hand, the simulation study in Fig. 4.2 shows that the plate temperature $y^p(t)$ is well approximated by the dominant plate mode $\boldsymbol{v}_1^p$. Therefore, a radically simplified system model is introduced in this section to approximate the behavior of $y^p(t)$ with a first-order model.

Consider the abstract furnace schematic shown in Fig. 4.3. The chamber is enclosed by a wall with the interior temperature T^w. It contains the plate with the assumed homogeneous temperature T^p and a hydrogen gas atmosphere. Radiative heat exchange takes place between the wall, the plate, and the heaters mounted on the ceiling of the chamber. The interior temperature T^w is measured and held at the reference value $r(=\text{const.})$ by a control loop that sets the total input power u. The symbols $\dot{Q}^p$ and $\dot{Q}^w$ represent the radiative heat flows from the heaters (temperature T^h) to the plate and to the wall, respectively. Convection and contact heat transfer are neglected due to their small contributions (cf. Section 3.1.2). The ambient environment has the homogeneous temperature T^∞. A two-color pyrometer measures the plate temperature y^{in} before the plate is charged into the

furnace (at time t^{in}) and y^{out} after its discharge (at time t^{out}).

In this section, a lumped-parameter model of the heat transfer between the furnace wall, the heaters, and the plate will be derived using the state variables T^w and T^p. The model will be further reduced to a first-order model under the assumption of an ideally controlled interior wall temperature T^w.

4.2.1 Radiation Equivalent Circuit

For the radiation enclosure formed by the furnace chamber assume (cf. [5, Sec. 5.5.3])

- isothermal wall, plate and heater surfaces,
- gray Lambertian radiators,
- the hemispherical total emissivities ε^w, ε^p, and ε^h of the wall, the plate, and the heater, respectively, characterize the entire surface,
- the respective absorptivities are $a^w = \varepsilon^w$, $a^p = \varepsilon^p$, and $a^h = \varepsilon^h$,
- the respective reflectivities are $r^w = 1 - \varepsilon^w$, $r^p = 1 - \varepsilon^p$, and $r^h = 1 - \varepsilon^h$,
- purely diffuse emission and reflection, and that
- Lambert's cosine law is applicable, i.e., the view factors F^{wp}, F^{wh}, and F^{ph} can be used to describe the radiation exchange.

The hydrogen atmosphere in the chamber is transparent for radiation. Thus, the net-radiation method can be applied to describe the radiation exchange.

Let σ be the Stefan-Boltzmann constant, and A^w, A^p, and A^h the surface areas of the wall, the plate, and the heater, respectively. According to [5, Sec. 5.5.3.1], the net-radiation method can be applied to a radiative enclosure with three surfaces using the equivalent circuit shown in Fig. 4.4a. This representation is advantageous because the emissivities ε^p, ε^w, and ε^h only influence their respective branches of the equivalent circuit. The circuit can be simplified by means of the Δ to Y transform, which yields Fig. 4.4b, with the parameters

$$E^p = \frac{1-\varepsilon^p}{A^p\varepsilon^p} + \frac{\frac{1}{(A^p)^2 F^{ph} F^{pw}}}{\frac{1}{A^p F^{ph}} + \frac{1}{A^p F^{pw}} + \frac{1}{A^w F^{wh}}} \tag{4.8a}$$

$$E^w = \frac{1-\varepsilon^w}{A^w\varepsilon^w} + \frac{\frac{1}{A^p A^w F^{pw} F^{wh}}}{\frac{1}{A^p F^{ph}} + \frac{1}{A^p F^{pw}} + \frac{1}{A^w F^{wh}}}. \tag{4.8b}$$

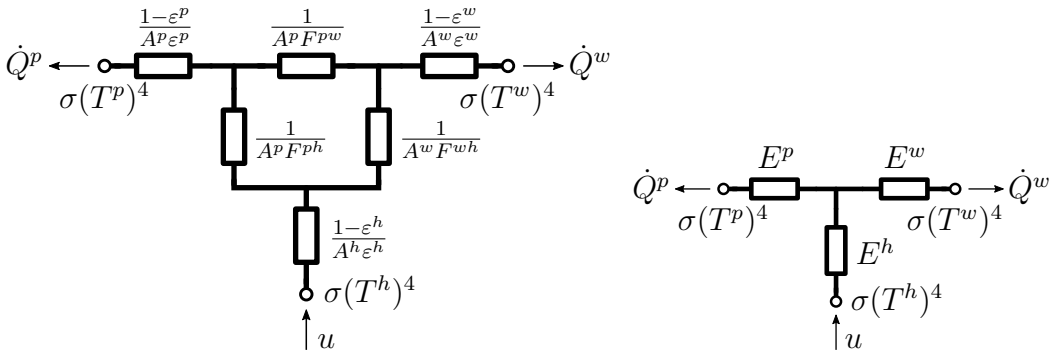

(a) Initial configuration. (b) Δ to Y transform.

Figure 4.4: Equivalent circuit of the radiation enclosure, according to the net-radiation method.

The parameter E^h is defined in a similar way, but will not be used any further. With the heat input u, the heat flows to the wall and the plate follow as

$$\dot{Q}^p = \frac{E^w}{E^p + E^w}u + \frac{1}{E^p + E^w}\Big(\sigma(T^w)^4 - \sigma(T^p)^4\Big) \tag{4.9a}$$

$$\dot{Q}^w = \frac{E^p}{E^p + E^w}u + \frac{1}{E^p + E^w}\Big(\sigma(T^p)^4 - \sigma(T^w)^4\Big). \tag{4.9b}$$

4.2.2 Dynamics

The plate and the wall in Fig. 4.3 are represented by lumped heat capacities $C^p(T^p)$ and $C^w(T^w)$, respectively. Let R^∞ be the heat resistance between the furnace interior wall and the ambient environment. The temperatures of the plate and the wall evolve according to

$$C^p(T^p)\frac{\mathrm{d}}{\mathrm{d}t}T^p = \dot{Q}^p \tag{4.10a}$$

$$C^w(T^w)\frac{\mathrm{d}}{\mathrm{d}t}T^w = \dot{Q}^w - \frac{1}{R^\infty}(T^w - T^\infty). \tag{4.10b}$$

At the charge and discharge times t^{in} and t^{out} of the plate, its temperatures are measured as

$$y^{\text{in}} = T^p(t^{\text{in}}) \tag{4.11a}$$

$$y^{\text{out}} = T^p(t^{\text{out}}). \tag{4.11b}$$

4.2.3 Model Reduction

Assuming ideal temperature control, i.e., $T^w \equiv r = \text{const.}$, the model equations (4.9) and (4.10) reduce to

$$\dot{Q}^p = \frac{E^w}{E^p + E^w} u + \frac{1}{E^p + E^w}\left(\sigma r^4 - \sigma (T^p)^4\right) \tag{4.12a}$$

$$\dot{Q}_s^w = \frac{E^p}{E^p + E^w} u + \frac{1}{E^p + E^w}\left(\sigma (T^p)^4 - \sigma r^4\right) \tag{4.12b}$$

$$C^p(T^p)\frac{\mathrm{d}}{\mathrm{d}t}T^p = \dot{Q}^p \tag{4.12c}$$

$$0 = \dot{Q}_s^w - \frac{1}{R^\infty}(r - T^\infty), \tag{4.12d}$$

where $\dot{Q}_s^w$ is the (constant) heat flow from the wall to the ambient environment. Eliminating u and $\dot{Q}^p$ in (4.12), we get the reduced model

$$C^p(T^p)\frac{\mathrm{d}}{\mathrm{d}t}T^p = \frac{E^w}{E^p}\dot{Q}_s^w + \frac{1}{E^p}(\sigma r^4 - \sigma (T^p)^4) \tag{4.13a}$$

$$y^{\text{in}} = T^p(t^{\text{in}}) \tag{4.13b}$$

$$y^{\text{out}} = T^p(t^{\text{out}}). \tag{4.13c}$$

Equations (4.12d) and (4.13) serve as the starting point for real-time optimization of the reheating times. Note that $C^p(T^p)$ and r are well known, while E^w, E^p, and $\dot{Q}_s^w$ have to be determined. In the next chapter, the unknown parameters of the minimal model (4.13) will be tuned to best approximate the measurements of y^{out} and to find optimal reheating times for future plates.

CHAPTER 5

Calculation of Optimum Reheating Times

In the previous chapters, a detailed process model of the considered chamber furnaces was formulated and drastically simplified to a first-order minimal model. The unknown parameters of the minimal model will be adapted, based on measurements of previously reheated plates, so that the minimal model is able to approximate the output of the detailed process model with sufficiently high accuracy. The minimal model can then be used to compute optimal reheating times for future products at very low computational costs.

In this chapter, a learning system is designed which comprises a parameter estimator and an optimizer for the reheating times. The designed estimator-optimizer structure will then be tested with the detailed process model representing the real plant. The design process and some of the numerical results are already published in [57].

5.1 Parameter Estimation and Calculation of Optimal Reheating Times

Based on the model equations (4.12d) and (4.13), the first goal is to determine the unknown parameters. From (4.12d), it can be seen that $\dot{Q}_s^w$ depends only on the heat resistance R^∞, the ambient temperature T^∞, and the reference temperature r. It is thus independent of the plate. According to (4.8), E^w and E^p change with the geometry of the radiation enclosure, including the dimensions of the plate. Additionally, ε^p, which influences E^p, can vary from product to product.

The basic idea is to estimate E^w and E^p based on similar plates that were reheated in the past and to reuse the estimated values to calculate the optimal

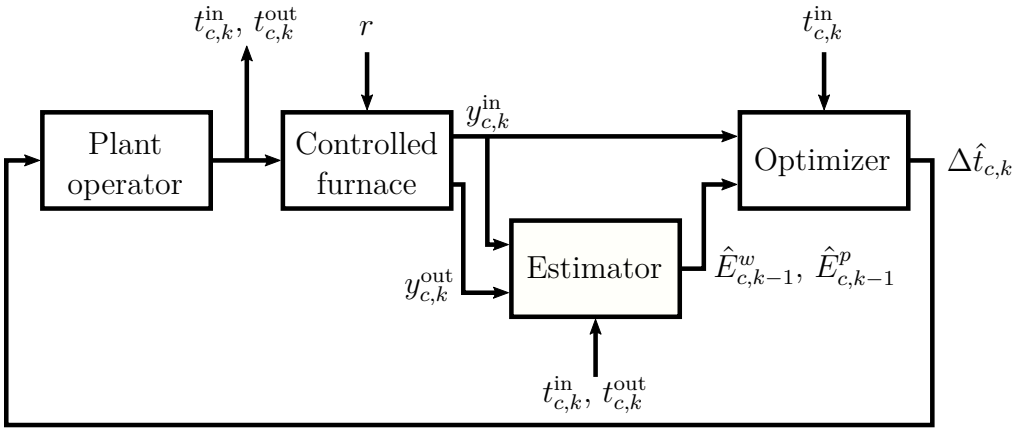

Figure 5.1: Proposed estimator-optimizer structure.

reheating times of similar products in the future. Therefore, the plates are grouped in product classes.

The parameter estimation and calculation of optimal reheating times proceed as follows:

- Identify $\dot{Q}^w_s$ for the furnace (Section 5.1.1).
- Define product classes for the expected product mix (Section 5.1.2).
- Estimate E^w for each class (Section 5.1.3).
- Estimate E^p for each class (Section 5.1.4).
- Calculate optimal reheating times for future products (Section 5.1.5).

Let c and k be the indices of the class and the product, respectively. For each plate, let $t^{\text{in}}_{c,k}$ and $t^{\text{out}}_{c,k}$ be the charge and discharge times, $y^{\text{in}}_{c,k}$ and $y^{\text{out}}_{c,k}$ the measured charge and discharge temperatures, and $\hat{E}^w_{c,k}$ and $\hat{E}^p_{c,k}$ the corresponding parameter estimates of E^w and E^p, respectively. Additionally, let $\Delta\hat{t}_{c,k}$ be the calculated optimal reheating times. In the following, the estimator-optimizer structure shown in Fig. 5.1 will be designed.

5.1.1 Heat Flow through Furnace Wall

At steady state ($\frac{\mathrm{d}}{\mathrm{d}t}T^p \equiv 0$, $T^p \equiv T^p_s$, $u \equiv u_s$), (4.12) yields

$$\dot{Q}^w_s = u_s. \tag{5.1}$$

Hence, $\dot{Q}^w_s$ can be directly obtained by measurement of the input $u(t) = u_s$ at steady state. This can be done at charged or empty state.

Product class c	Material	Previous rolling passes	Length (mm)	Width (mm)	Thickness (mm)
1	Mo	0	500 – 1500	0 – 1000	60 – 120
2	Mo	0	500 – 1500	1000 – 2000	10 – 120
3	W	0	0 – 1000	0 – 1000	10 – 60
4	Mo	1	1000 – 2500	0 – 1000	10 – 60
⋮	⋮	⋮	⋮	⋮	⋮

Table 5.1: Examples of product classes.

5.1.2 Product Classes

Products are grouped in product classes because the parameters E^w and E^p depend on the geometry of the radiation enclosure and thus on the geometric dimensions of the plates. Moreover, the parameter E^p is also influenced by the emissivity ε^p of the plate, which in turn depends on its material and surface condition. Therefore, for the estimation of E^w and E^p, plates with similar dimensions, material, and surface conditions are combined into one class.

In the considered rolling plant, the surface conditions of the plates depend mainly on the number of previous rolling passes. Table 5.1 shows some examples of typical product classes.

5.1.3 Estimation of E^w

To identify the parameter E^w_c, which represents E^w for the product class c, consider (4.13a) for the plate k from the product class c,

$$C^p_{c,k}(T^p_{c,k})\frac{\mathrm{d}}{\mathrm{d}t}T^p_{c,k} = \frac{1}{E^p_{c,k}}\left(\sigma\underbrace{\left(1+\frac{E^w_{c,k}\dot{Q}^w_s}{\sigma r^4}\right)}_{\beta^4_{c,k}} r^4 - \sigma(T^p_{c,k})^4\right), \tag{5.2}$$

where $C^p_{c,k}$, $T^p_{c,k}$, $E^w_{c,k}$ and $E^p_{c,k}$ are the respective parameters C^p, T^p, E^w, and E^p corresponding to that plate. While a change in $E^w_{c,k}$ does not change the qualitative evolution of the trajectory $T^p_{c,k}(t)$, it shifts the steady-state plate temperature $T^p_{c,k,s}$ in the form

$$T^p_{c,k,s} = \beta_{c,k} r, \quad \beta_{c,k} = \sqrt[4]{1+\frac{E^w_{c,k}\dot{Q}^w_s}{\sigma r^4}}. \tag{5.3}$$

Let β_c refer to the mean value of $\beta_{c,k}$ in the product class c. The ratio β_c is specific to the design and control of the considered furnace and can be determined

based on previous measurements $y_{c,k}^{\text{out}}$ in the respective class. For the considered system, $\beta_c \approx 1$ is assumed, i.e., the steady-state plate temperature $T_{c,k,s}^{p}$ does not significantly exceed the reference furnace temperature r. It is therefore expected that E_c^w will have relatively small values. The validity of this assumption is checked in Section 5.2. As initial estimate, $\hat{E}_{c,0}^w = 0$ is used, and the first product ($k = 1$) of each product class is overheated on purpose to find a representative estimate $\hat{E}_{c,1}^w$. Section 5.1.4 contains more details on this intentional overheating.

For the estimation of E_c^w consider (4.13a) at steady state. At the time $t_{c,k}^{\text{out}}$, the plate is discharged from the furnace and the temperature $y_{c,k}^{\text{out}}$ is measured according to (4.13c). In this case, $E_{c,k}^w$ calculates to

$$E_{c,k}^w = \frac{\sigma (y_{c,k}^{\text{out}})^4 - \sigma r^4}{\dot{Q}_s^w}. \tag{5.4}$$

A weighted recursive least-squares (RLS) algorithm, see, e.g., [41], can be used to estimate the mean value E_c^w of the product class c in the form

$$\kappa_{c,k}^w = \begin{cases} \dfrac{\kappa_{c,k-1}^w}{q + \kappa_{c,k-1}^w}, & \text{if } y_{c,k}^{\text{out}} > r \\ \kappa_{c,k-1}^w, & \text{else,} \end{cases} \qquad 0 \ll q < 1 \ll \kappa_{c,0}^w \tag{5.5a}$$

$$\hat{E}_{c,k}^w = \begin{cases} (1 - \kappa_{c,k}^w)\hat{E}_{c,k-1}^w + \kappa_{c,k}^w \dfrac{\sigma (y_{c,k}^{\text{out}})^4 - \sigma r^4}{\dot{Q}_s^w}, & \text{if } y_{c,k}^{\text{out}} > r \\ \hat{E}_{c,k}^w, & \text{else,} \end{cases} \qquad \hat{E}_{c,0}^w = 0 \tag{5.5b}$$

Here, it makes sense to only iterate the estimate if $y_{c,k}^{\text{out}} > r$, because this is a necessary condition for the steady state. The initial value $\kappa_{c,0}^w$ is chosen very large, such that the first iteration ($\hat{E}_{c,1}^w$) of the RLS algorithm is already close to the first measurement. The parameter q is an exponential forgetting factor.

Remark 1. If the condition $\beta_c \approx 1$ is not satisfied, it is necessary to determine the mean value E_c^w with higher accuracy. In this case, several intentional overheating cycles must be performed to get a better estimate $\hat{E}_{c,k}^w$.

5.1.4 Estimation of E^p

The parameter E_c^p, which refers to E^p for the product class c, is estimated based on (4.13). For a single plate, the estimate $\hat{E}_{c,k}^p$ is obtained from

$$\min_{\hat{E}_{c,k}^p} \frac{1}{2}(\hat{y}_{c,k}^{\text{out}} - y_{c,k}^{\text{out}})^2 + \frac{1}{2\gamma}(\hat{E}_{c,k}^p)^2 \tag{5.6a}$$

$$\text{s.t.} \quad C_{c,k}^p(\hat{T}_{c,k}^p)\frac{\mathrm{d}}{\mathrm{d}t}\hat{T}_{c,k}^p = \frac{\hat{E}_{c,k}^w}{\hat{E}_{c,k}^p}\dot{Q}_s^w + \frac{1}{\hat{E}_{c,k}^p}(\sigma r^4 - \sigma(\hat{T}_{c,k}^p)^4) \tag{5.6b}$$

$$\hat{T}_{c,k}^p(t_{c,k}^{\text{in}}) = y_{c,k}^{\text{in}} \tag{5.6c}$$

$$\hat{T}_{c,k}^p(t_{c,k}^{\text{out}}) = \hat{y}_{c,k}^{\text{out}}, \tag{5.6d}$$

where $\gamma > 0$ is a weighting parameter to regularize the optimization problem.

To use the estimate $\hat{E}_{c,k}^p$ for future plates with different dimensions, consider (4.8a). The parameter E^p can be rewritten in the form

$$E^p = \frac{1}{A^p}\left(\frac{1-\varepsilon^p}{\varepsilon^p} + \frac{1}{F^{pw} + F^{ph} + \frac{A^p F^{ph} F^{pw}}{A^w F^{wh}}}\right). \tag{5.7}$$

Because the plates are convex, $F^{pp} = 0$ and $F^{pw} + F^{ph} = 1$, see, e.g., [5]. Moreover, the reciprocity theorem for view factors implies $A^p F^{pw} = A^w F^{wp}$ and thus

$$E^p = \frac{1}{A^p}\underbrace{\left(\frac{1-\varepsilon^p}{\varepsilon^p} + \frac{1}{1 + \frac{F^{wp}F^{ph}}{F^{wh}}}\right)}_{1/\eta^p}. \tag{5.8}$$

If the ratio $(F^{wp}F^{ph})/F^{wh}$ of the view factors is known, ε^p can be directly computed from (5.8). In this work, however, the view factors are assumed to be unknown. The value

$$\eta^p = \frac{1}{A^p E^p} \tag{5.9}$$

is therefore used as a substitute parameter and will be estimated instead of ε^p.

Remark 2. The substitute parameter η^p depends on the view factors and therefore on the plate geometry. However, the range for the values of η^p can be reduced by making the product classes more specific with respect to the geometric dimensions.

Let $A_{c,k}^p$ be the surface area of the plate k from the product class c. Similar to (5.5), a weighted RLS algorithm of the form

$$\kappa_{c,k}^p = \frac{\kappa_{c,k-1}^p}{q + \kappa_{c,k-1}^p}, \qquad 0 \ll q < 1 \ll \kappa_{c,0}^p \tag{5.10a}$$

$$\hat{\eta}_{c,k}^p = (1 - \kappa_{c,k}^p)\hat{\eta}_{c,k-1}^p + \kappa_{c,k}^p \frac{1}{A_{c,k}^p \hat{E}_{c,k}^p}, \quad 0 < \hat{\eta}_{c,0}^p \ll 1 \tag{5.10b}$$

can be employed to approximate the mean value η_c^p of the product class c. The initial value $\hat{\eta}_{c,0}^p$ is chosen close to zero. This is an intentional underestimation to ensure that the first product in a certain class c is overheated. This intentional overheating cycle is used to trigger the estimator (5.5) for $\hat{E}_{c,1}^w$.

5.1.5 Calculation of Optimum Reheating Times

The estimates $\hat{E}_{c,k-1}^w$ and $\hat{\eta}_{c,k-1}^p$ from the previous plates are used in a prediction model to determine the optimal reheating time of the next plate from the same class c. The reheating times are computed by solving

$$C_{c,k}^p(\hat{T}_{c,k}^p(t))\frac{\mathrm{d}}{\mathrm{d}t}\hat{T}_{c,k}^p(t) = A_{c,k}^p\hat{\eta}_{c,k-1}^p\left(\hat{E}_{c,k-1}^w\dot{Q}_s^w + \sigma r^4 - \sigma(\hat{T}_{c,k}^p(t))^4\right) \tag{5.11a}$$

$$\hat{T}_{c,k}^p(0) = y_{c,k}^{\mathrm{in}} \tag{5.11b}$$

$$\hat{T}_{c,k}^p(\Delta\hat{t}_{c,k}) = y_d^{\mathrm{out}} \tag{5.11c}$$

for the unknown $\Delta\hat{t}_{c,k}$ by means of an ODE solver and linear interpolation of the solution. Here, y_d^{out} is the desired discharge temperature.

5.2 Proof of Concept

The developed strategy is tested in a simulation environment. The validated detailed process model (3.20) with the sensor outputs (3.22) and (3.24) and the temperature controller (3.23), see also Fig. 3.4, represents the considered batch-type furnace. The temperature-controlled process model was embedded in MATLAB/SIMULINK and connected to the proposed estimator-optimizer structure. The interfaces to the estimator-optimizer system are

$$u(t) = \mathbf{1}^{\mathrm{T}}\boldsymbol{u}(t) \tag{5.12a}$$

$$y_{c,k}^{\mathrm{in}} = y^p(t_{c,k}^{\mathrm{in}}) \tag{5.12b}$$

$$y_{c,k}^{\mathrm{out}} = y^p(t_{c,k}^{\mathrm{out}}), \tag{5.12c}$$

and the steady-state power input $\dot{Q}_s^w$ is obtained according to (5.1).

5.2.1 Plant Analysis

The temperature-controlled process model exhibits the following properties:

- The temperature controller (3.23) keeps the wall temperatures $\boldsymbol{y}^w$ close to the desired setpoint r. The assumption of an ideal temperature controller is therefore satisfied.
- The parameter $\dot{Q}_s^w$ can be computed directly in a steady-state simulation (cf. Section 5.1.1).

Product no.	Length (mm)	Width (mm)	Thickness (mm)	$\varepsilon^p_{c,k}$	$y^{\text{in}}_{c,k}$ (°C)	y^{out}_d (°C)	c	k
1	1240	610	120	0.25	30	1270	1	1
2	1220	600	68	0.25	30	1270	1	2
3	1270	610	120	0.25	30	1270	1	3
4	1150	1370	26	0.25	30	1270	2	1
5	840	580	68	0.25	30	1270	1	4
6	640	1520	13	0.25	30	1270	2	2
7	1260	630	120	0.25	30	1270	1	5
8	840	580	68	0.25	30	1270	1	6
9	1160	580	120	0.25	30	1270	1	7
10	1200	610	80	0.25	30	1270	1	8

Table 5.2: Product parameters for the test scenario.

- The maximum final plate temperatures were found to be in the range $T^p_s \approx 1.03r$. Hence $\beta \approx 1$ holds for β from (5.3). The parameter E^w can therefore be estimated according to the procedure presented in Section 5.1.3.
- The parameter η^p according to (5.9) will be used instead of ε^p (cf. Section 5.1.4).
- The ratio of the view factors according to (5.8) is $(F^{wp}F^{ph}/F^{wh}) \approx 0.2$ for the considered plates. Therefore, the estimate $\hat{\eta}^p_{c,k}$ will converge to a value close to ε^p.

5.2.2 Test Scenario

As a test scenario, products for a 12-hour shift were randomly generated. They are all reheated for the same setpoint $r = 1300$°C and the same desired product temperature $y^{\text{out}}_d = 1270$°C. The product data are given in Table 5.2. Following the definitions of the product classes from Table 5.1, the products are allocated to the classes $c = 1$ and $c = 2$.

For the open-loop configuration, the plant operator chooses reheating times $\Delta t^{\text{man}}_{c,k}$ according to the existing manufacturing plans, which are provided by an expert system based on experience and analogies. For the closed-loop configuration, the operator uses the calculated optimum reheating times $\Delta \hat{t}_{c,k}$. The designed system will be tested with the following simulation scenarios.

1. Open loop with fixed parameter values to analyze the estimator performance

2. Closed loop and fixed parameter values to analyze the performance limit of the designed system

3. Closed loop and uncertain parameter values to analyze the robustness of the designed system with respect to unknown variations of the parameters

The goal is to show that the proposed concept, demonstrated in the simulations 2 and 3, is able to reduce the reheating times compared to the expert system, demonstrated by simulation 1. Moreover, the exit temperatures $y_{c,k}^{\text{out}}$ (cf. (5.12c)) should be within a range of ± 15°C of the desired temperature y_d^{out}.

5.2.3 Simulation Results

Simulation 1: Open loop, fixed parameters Figure 5.2 depicts the simulation results for the reheating times $\Delta t_{c,k}^{\text{man}}$ according to the manufacturing plan.

The input heating powers $\boldsymbol{u}(t)$ behave differently in each zone of the furnace, depending on how much heat the plate draws from the respective zones. The plates of product classes $c = 1$ and $c = 2$ (see Table 5.1) are not so long that they extend into the last furnace zone (cf. Fig. 3.1). Therefore, $u_3(t)$ is almost constant.

The wall surface temperatures $\boldsymbol{y}^w$ experience short-time disturbances between 3°C and 10°C. The relative error $(y_i^w - r)/r$ $(i = 1, 2, 3)$ is below 1%. The assumption of ideal wall temperature control is therefore well justified.

The chosen reheating times $\Delta t_{c,k}^{\text{man}}$ are plotted and compared to the optimum reheating times $\Delta \hat{t}_{c,k}$. The total processing time is 591min.

Figure 5.2 shows that most products are heated beyond the desired value $y_d^{\text{out}} \pm 15$°C, while a few even leave the furnace too cold.

The objective of this simulation scenario is mainly to analyze the performance of the estimator. The estimates $\hat{E}_{c,k}^w$ and $\hat{\eta}_{c,k}^p$ are depicted in the bottom plots of Fig. 5.2 and $\hat{\eta}_{c,k}^p$ converges to a value close to the actual plate emissivities $\varepsilon_{c,k}^p = 0.25$.

Simulation 2: Closed loop, fixed parameters For the simulation 2, the calculated optimum reheating times $\Delta \hat{t}_{c,k}$ from (5.11) are used. The results for the closed-loop configuration with fixed parameters are shown in Fig. 5.3. The time evolutions of the input powers $\boldsymbol{u}(t)$ and the wall temperatures $\boldsymbol{y}^w(t)$ are similar to simulation 1.

The first product of each product class is intentionally overheated to perform the estimation of E_c^w. Then the error $(y_{c,k}^{\text{out}} - y_d^{\text{out}})$ quickly decays to the tolerance band $y_d^{\text{out}} \pm 15$°C.

The chosen reheating times $\Delta \hat{t}_{c,k}$ are plotted and compared to the reheating times $\Delta t_{c,k}^{\text{man}}$ from the manufacturing plan. The total processing time amounts to

Product no.	1	2	3	4	5
$\varepsilon^p_{c,k}$	0.2555	0.2357	0.2759	0.2091	0.2637
Product no.	6	7	8	9	10
$\varepsilon^p_{c,k}$	0.2245	0.2400	0.2666	0.2812	0.2165

Table 5.3: Perturbed parameters for simulation 3.

535min. This is an improvement of 9.5% compared to simulation 1, despite the time loss during the intentional overheating of the first product in both product classes.

The estimated values $\hat{E}^w_{c,k}$ and $\hat{\eta}^p_{c,k}$ differ from the open-loop estimates due to different (measurement) values of $y^{\text{out}}_{c,k}$. Notice especially the improved estimate of E^w_1, which was obtained through intentional overheating.

Simulation 3: Closed loop, uncertain parameters For simulation 3, the parameters $\varepsilon^p_{c,k}$ are perturbed with Gaussian noise (standard deviation 10% of the base value) and the calculated optimum reheating times $\Delta\hat{t}_{c,k}$ from (5.11) are used. The perturbed parameter values are given in Table 5.3. The corresponding sample standard deviation is 0.0254, i.e., approximately 10% of the base value. The results for the closed-loop configuration with uncertain parameters are depicted in Fig. 5.4.

The input powers $\boldsymbol{u}(t)$ and the wall temperatures $\boldsymbol{y}^w(t)$ are similar to simulations 1 and 2. The estimates $\hat{E}^w_{c,k}$ and $\hat{\eta}^p_{c,k}$ are close to the values of simulation 2, which implies that they are robust with respect to the (zero-mean) parameter perturbations.

In the considered case, the perturbation of $\varepsilon^p_{c,k}$ with Gaussian noise according to Table 5.3 increases the temperature error of most products by approximately 15°C. As a result, with the used sample products, the product parameters are required to deviate no more than 10% from their nominal value.

The exit temperatures $y^{\text{out}}_{c,k}$ of most of the products stay within the tolerance band of $y^{\text{out}}_d \pm 15$°C.

The total processing time is 532min and thus only slightly differs from simulation 2 due to the perturbation of $\varepsilon^p_{c,k}$.

5.3 Long-Term Tests

The results of the previous section prove the working principle of the designed estimator-optimizer structure for reheating time optimization. It is concluded that the upstream manufacturing process is required to specify product parameters with a total deviation of no more than 10% from their nominal value in order to keep the exit temperatures $y^{\text{out}}_{c,k}$ of the products within the tolerance band of

Test no.	Material	Length (mm)	Width (mm)	Thickness (mm)	$\varepsilon^{p}_{c,k}$	$y^{\text{in}}_{c,k}$ (°C)	y^{out}_{d} (°C)
1	Mo	500–1500	500	60	0.25	30	1270
2	Mo	1000	100–1000	60	0.25	30	1270
3	Mo	1000	500	2.5–120	0.25	30	1270

Table 5.4: Product parameters for the long-term tests.

± 15°C of the desired value y^{out}_{d}. In the following, the choice of product class boundaries is investigated in long-term tests.

5.3.1 Varying Plate Dimensions

In a set of long-term tests, the sensitivity of the designed estimator-predictor system with respect to the plate dimensions is examined. To this end, three long-term tests with 100 randomly generated products according to Table 5.4 are performed. The products are generated by a uniformly-distributed random variable. All products are allocated to the same product class. The long-term tests described in Table 5.4 demonstrate the sensitivity of the optimizer results with respect to variations in the plate dimension, that is, with respect to the product class boundaries.

Figure 5.5 shows histograms of the output temperatures $y^{\text{out}}_{c,k}$ from each long-term test. It can be seen that variations of the length (long-term test 1) and thickness (long-term test 3) of the plate have only minor influence on the output temperature. This is due to the geometries of the furnace chamber and plate. The chamber is designed as a long tube, where the door end acts as a mirror and the back end is relatively far away from the plate. Therefore, the heating of the plate depends only weakly on the longitudinal dimension. The robustness of the optimization result with respect to the plate thickness is due to the high thermal conductivity of molybdenum. As can be checked with the so-called Biot number (cf. [39]), the plate temperature is very close to its mean value along the thickness direction.

The sensitivity of the plate exit temperatures with respect to the plate width (long-term test 2) is higher compared to the other dimensions. In order to keep the exit temperatures within the tolerance band, it is necessary to narrow the width bounds of the considered product class.

5.3.2 Effects of Narrowing the Product Classes

The effects of subdividing a product class into several classes with restricted plate widths are examined in the following. Table 5.5 contains the parameters of four

Product classes	Material	Length (mm)	Width (mm)	Thickness (mm)	$\varepsilon^{p}_{c,k}$	$y^{\text{in}}_{c,k}$ (°C)	y^{out}_{d} (°C)
1	Mo	500–1500	100–1000	60–120	0.25	30	1270
9	Mo	500–1500	100–200,...1000	60–120	0.25	30	1270
1	Mo	500–1500	100–1000	60–120	0.225–0.275	30	1270
9	Mo	500–1500	100–200,...1000	60–120	0.225–0.275	30	1270

Table 5.5: Product parameters of the long-term tests.

long-term tests.

In the first test, products are randomly generated from a single large product class with plate widths ranging from 100mm to 1000mm. In the second test, the simulation is repeated using nine narrower class definitions, with plate widths from 100mm to 200mm, from 200mm to 300mm and so forth.

In the third and fourth test, the tests are repeated with added uncertainty in the plate emissivity. Here, the emissivities are uniformly distributed between 90% and 110% of their nominal value (cf. Table 5.5).

The histograms of the performed tests are shown in Fig. 5.6. It can be seen that narrowing the plate widths of a class clearly reduces the standard deviation of the product exit temperatures. In the considered case, the standard deviation is approximately halved. The outliers between 1305°C and 1310°C are caused by intentional overheating, as discussed in Section 5.1.4. In the tests with varying emissivities, the use of one large product class results in 13 underheated products, while the use of nine product classes results in only two underheated products.

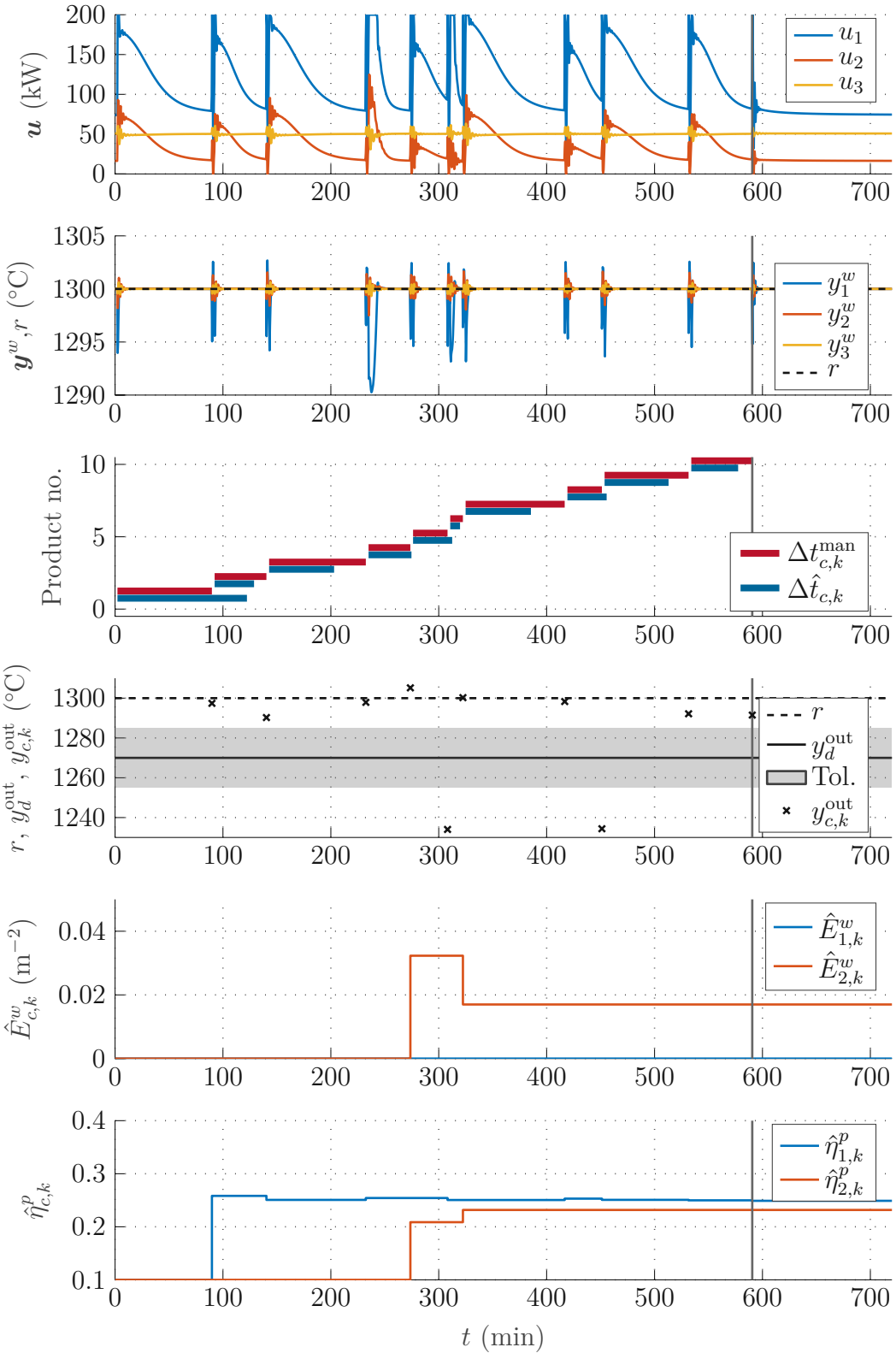

Figure 5.2: Result of simulation 1; fixed parameters, open loop.

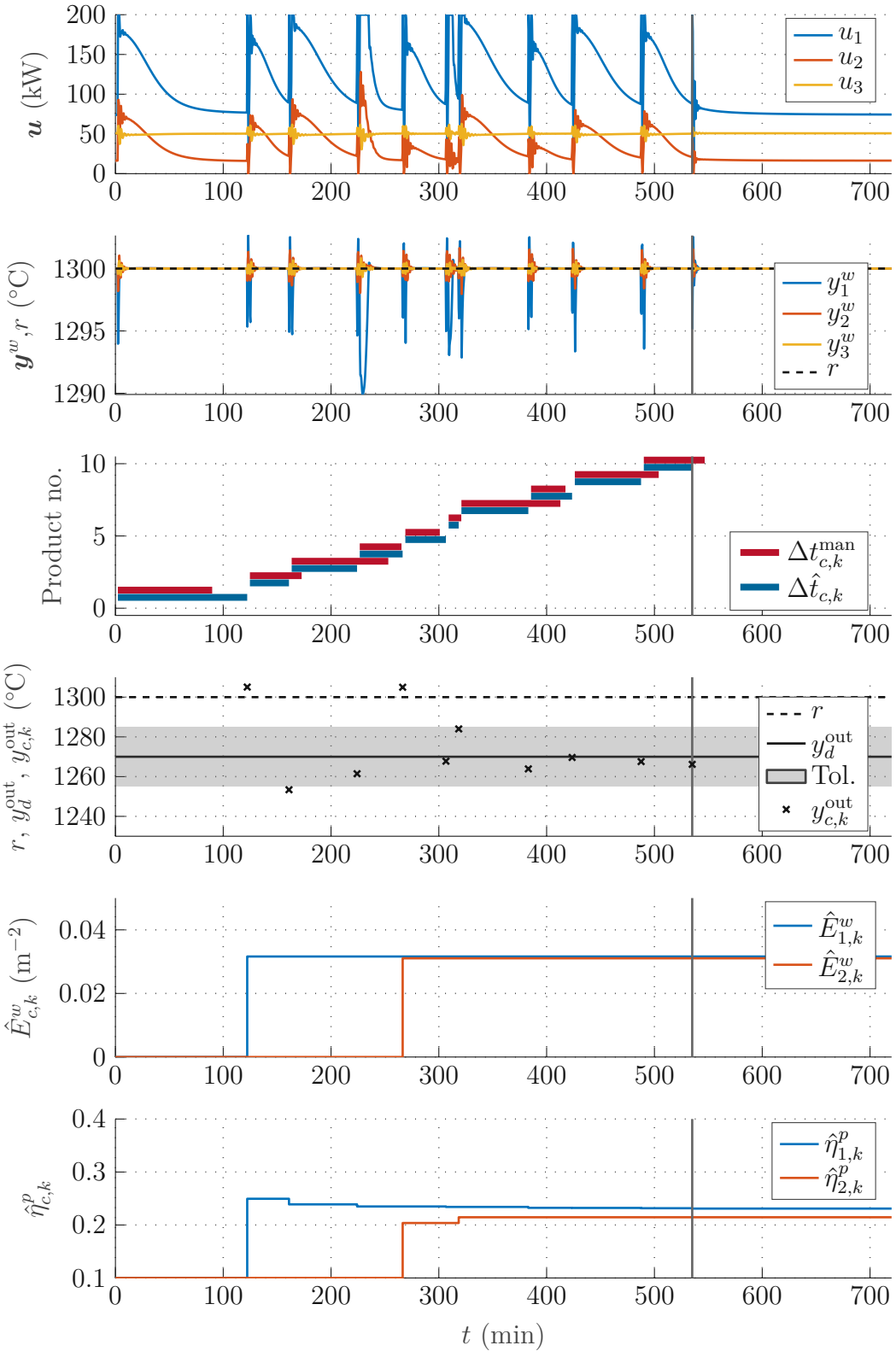

Figure 5.3: Result of simulation 2; fixed parameters, closed loop.

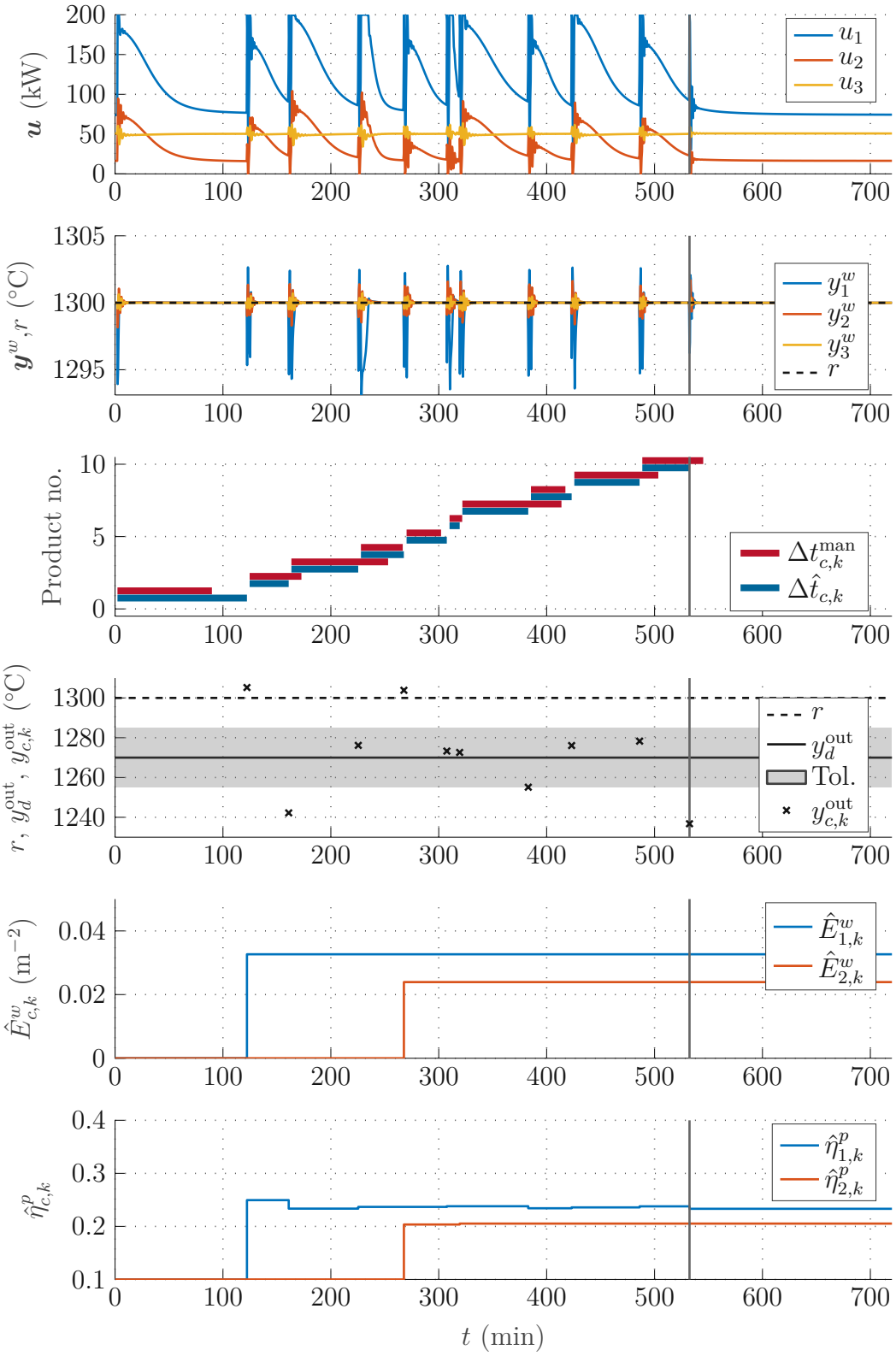

Figure 5.4: Result of simulation 3, perturbed parameters, closed loop.

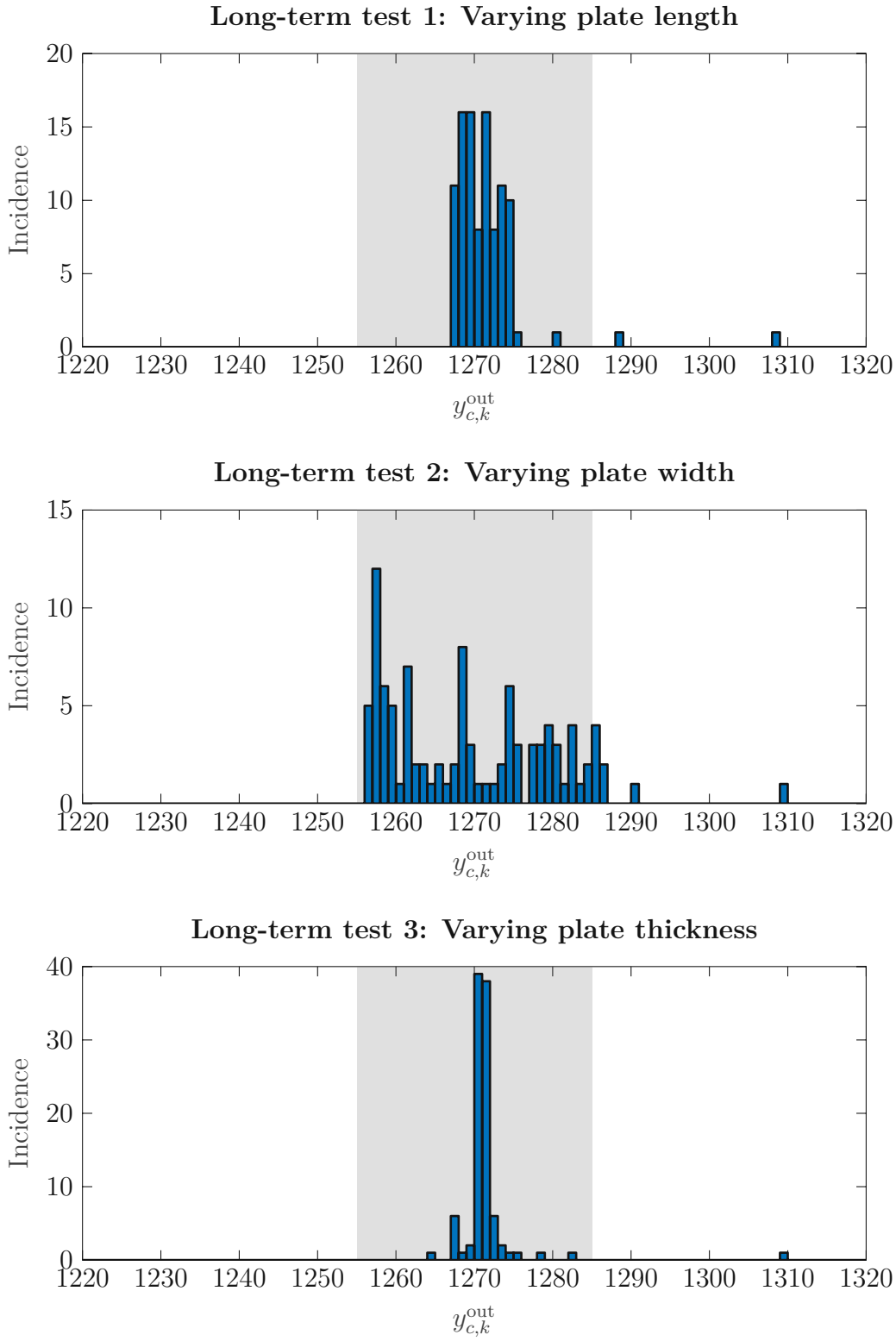

Figure 5.5: Results of the long-term tests.

Figure 5.6: Comparison of long-term tests for one large product class with nine smaller product classes. The simulation parameters are listed in Table 5.5.

CHAPTER 6

Conclusions and Outlook

In the first part of this thesis, the reheating of heavy plates of refractory metals in a batch-type chamber furnace was investigated. The goal was to determine the minimal reheating times for a given mode of operation where the plate temperature cannot be measured while the plate resides in the furnace. Due to the asymptotic evolution of the plate temperature towards its desired value, the required heating time for a given discharge temperature is highly sensitive with respect to the system parameters.

6.1 Summary

A detailed process model was developed based on first principles. This model captures the heat transfer by both radiation and conduction. Unknown material parameters of the furnace wall were identified based on measurement data.

Subsequently, a model order reduction was performed using the Proper Orthogonal Decomposition (POD) method with mode shapes derived from simulations. The reduced-order model was further examined and it was found that the desired model output, i.e., the discharge temperature, can be accurately described by a single POD mode. Based on this observation, a minimal model of order one was developed which has significantly lower computational costs.

The products of the plant may vary in size, material, surface properties, and rolling passes and are clustered according to these parameters. For each product class, some model parameters are estimated from the reheating of previous products in this class. Based on these estimates, the optimum reheating times of future products are calculated.

The solution based on the first-order mathematical model exhibits a high

accuracy even for uncertain model parameters. The performance of the proposed approach was investigated by simulation studies on the validated process model. For the considered test scenarios, a reduction of the total processing time by approximately 9.5% compared to the current operating practice can be achieved. Long-term tests were conducted to show the performance for properly chosen product classes and limited parameter uncertainties.

6.2 Conclusions

The considered system serves as an example for a reheating-by-waiting process. Since the reheating process is asymptotically stable and converges to the desired discharge temperature, the goal of this work was not to control the temperatures, but rather to accurately compute the optimum reheating time for a product. For this reason, it is sufficient that the model accurately captures the input-output relations of the process. The introduction of product classes allows to estimate representative product parameters and efficiently optimize the reheating times.

The designed estimator-optimizer structure can be easily transferred to other batch-type furnace systems and is a good example of a combination of first-principles models and data-driven methods.

6.3 Outlook

The considered furnaces are part of a production plant for heavy plates. The results of the optimizer may be used to change and adapt the production schedule of the heavy-plate mill. To this end, the designed estimator-optimizer structure can be embedded in a scheduling algorithm like [3].

Part II

Induction Reheating of Thin Metal Sheets

CHAPTER 7

Preliminaries

This second part of the thesis deals with the reheating process in the coil production plant of Plansee SE. The coil production plant is shown in Fig. 7.1. A thin sheet of refractory metal enters over the entry roller table and is fixed by a clamping roll. The sheet then passes under a number of electromagnetic inductors, where it is heated along the cutting lines in longitudinal direction. Finally, the sheet is cut into stripes and the stripes are wound up by a coiler. The produced coils undergo further manufacturing steps downstream.

The reheating of the sheet is caused by Joule losses from electromagnetically induced eddy currents. The induced eddy currents in the sheet diminish rapidly when the air gap between the inductor coil and the sheet is increased. The inductors are arranged in such a way that a mutual coupling is avoided.

The sheet is produced by the same rolling plant as described in Part I and the leveler used in the plant is designed for heavy plates rather than thin sheets. Therefore, the sheet retains some flatness defects. These flatness defects cause large temperature fluctuations during the reheating along the cutting line, which in turn compromise the quality of the cutting edges. Coils with inferior edge quality have to undergo additional manufacturing steps, or even have to be discarded.

7.1 Industrial Requirements

The necessity to post-process or discard badly-cut coils should be avoided. To this end, the induction heating (IH) process must be improved. For the cutting edge to be of good quality, the sheet should be heated above 250°C. On the other hand, unnecessary overheating of the sheet is a waste of energy.

Induction heating systems typically consist of power electronics, magnetic

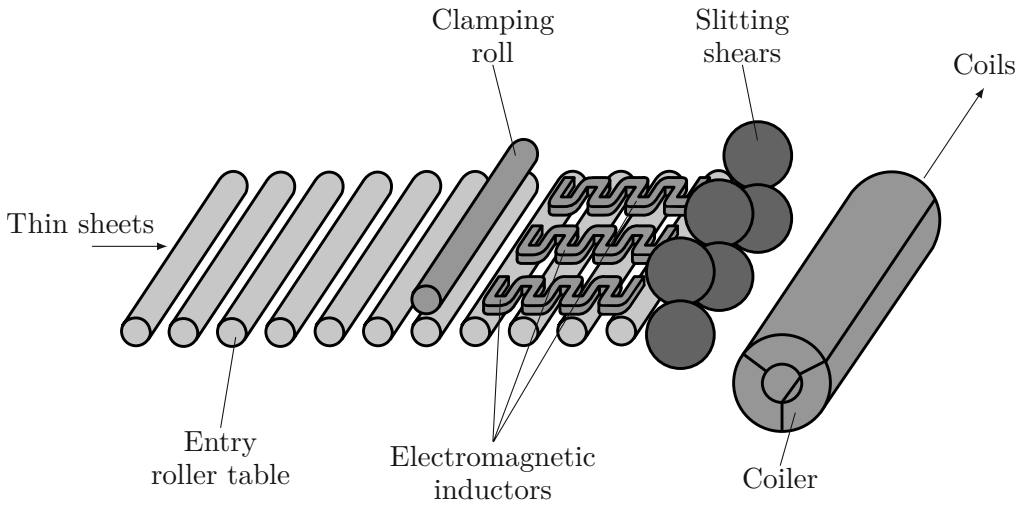

Figure 7.1: Coil production plant.

components including the workpiece, and a control system (cf. [42]). The geometry and power electronics of the considered IH system are already given. Consequently, a control system is required that mitigates the temperature fluctuations at the exit of each inductor.

In a first step, the total heating power transmitted from each inductor to the sheet should be controlled. This way, the correct amount of enthalpy can be supplied to the sheet. In a second step, the (unmeasured) air gap fluctuations should be compensated as accurately as possible by a temperature controller.

7.2 State of the Art

Most published control solutions focus on the power supplied to the inductor. The power can be controlled by the (complex) amplitude of the supply current, which was done in [15–17, 46]. Additionally, [44] contains a method to eliminate parasitic coupling effects between multiple inductors. For a single inductor system, a controller that tracks the resonance frequency and thus minimizes the reactive load for the power supply is designed in [75]. Controlling the (active) power supplied to the inductor does not guarantee that the desired heating power enters the workpiece. For this reason, the literature on this subject can only be the starting point for the problem at hand.

One option to capture the difference between the supply power and the actual heating power are electromagnetic field calculations, which are typically performed by finite-element (FE) software. FE simulations are used, for instance, in [24, 45, 47] to pre-calculate the distribution of induced currents. The results of [45, 47] are subsequently used for feedforward (FF) control. These works focus on domestic stoves, where the main objective is homogeneous heating rather than

temperature control.

Optimal FF temperature control was considered in [52–54]. The drawback of this approach is that the necessary FE calculations cannot be performed in real time.

With the exception of [19], the literature lacks reports on feedback (FB) temperature control for industrial IH systems. In [19], a nonlinear model predictive controller is designed based on a finite-difference model of a cylindrical rod with a surrounding coil. Unlike in the FE-based works, the geometry is simple enough for online calculations. Also, changes of the air gap geometry due to an excentric rod position are practically negligible.

The problem considered in this thesis differs from the works discussed above insofar as the uncertain and unmeasured air gap geometry has a major influence on the resulting sheet temperature. Nonetheless, the techniques used in these works serve as a good starting point for the investigations in this thesis.

7.3 Motivation

Usually, the field geometries in IH are supposed to be well known, or equivalently, uncertainties need to have only a negligible effect. This is the case in the reported applications from the literature. In longitudinal field applications, where the coil winds around the heating subject, a homogeneous distribution of the magnetic field and flux density can be assumed and small displacements of the load have no effect. In transversal field applications such as domestic stoves, the heating subject is supposed to be within a known distance to the coil winding.

In the present case, the variations of the air gap are neither known in advance nor measured and thus have to be compensated. Such configurations of induction heating are rather uncommon and require the design of new control concepts.

7.4 Approach and Scientific Contributions

The approach pursued in this thesis can be summarized as follows:

- Formulate a 3D FE model with a constant air gap and verify it with recorded plant data.
- Reduce to a control-oriented 1D model which systematically incorporates the air gap changes.
- Design a temperature controller to compensate for the variations of the air gap and test it in simulations.

Large parts of the designed air gap compensation and temperature controller presented in this thesis are already published in [55].

7.5 Outline of Part II

Part II of the thesis is organized as follows: Chapter 8 is dedicated to the formulation of the mathematical models. First, a 3D process model is derived from first principles and validated using recorded plant measurement data. The process model is then simplified to a control-oriented model, which consists of a 1D thermal model and an equivalent circuit for the elecromagnetic subsystem. In Chapter 9, a cascade controller is designed for the control-oriented model. The controller design is tested based on the detailed process model in Chapter 10 and some concluding remarks are given in Chapter 11.

CHAPTER 8

Physical Modeling

In the following, a mathematical model of the considered IH system is derived. Figure 8.1a shows the essential parts of the system. A thin molybdenum sheet moves under a longitudinal inductor coil winding and a narrow stripe of the sheet is reheated. Along this reheated stripe, a downstream slitting shear cuts the strip. The quality of the cutting edge strongly depends on the strip temperature T.

The metal sheet occupies the domain $\Omega^p \subset \mathbb{R}^3$. The sheet is fixed between an upstream clamping roll and the downstream slitting shear and exhibits uncertain flatness defects, which are caused by residual mechanical stresses that were introduced during the upstream rolling process. Additional thermal stresses are insignificant due to the low heat expansion of molybdenum.

A spatially fixed Cartesian coordinate system is used, where the sheet moves along the x direction below the inductor coil, i.e., $\Omega^p = \Omega^p(t)$, with the time coordinate t. The strip temperature depends on the spatial coordinates x, y, z, and the time t, i.e.,

$$T = T(x, y, z, t). \tag{8.1}$$

The inductor reaches from $x = \Delta l$ to $x = l_x - \Delta l$. The copper winding occupies the domain $\Omega^c \subset \mathbb{R}^3$ and has the entry and exit faces $\Gamma^{c,\text{in}}$ and $\Gamma^{c,\text{out}}$, respectively. The winding is a hollow conductor with rectangular cross-section and internal water cooling. Magnetic cores, so-called concentrators, of width l_z enclose the conductor and guide the magnetic flux. The field domain for the IH process model will be denoted by Ω. Consider the domains

$$\Omega^p(t), \Omega^c \subset \Omega \subset \mathbb{R}^3, \quad \Omega^p(t) \cap \Omega^c = \emptyset \tag{8.2a}$$

$$\Gamma^{c,\text{in}}, \Gamma^{c,\text{out}} \subset \partial\Omega^c \cap \partial\Omega \neq \emptyset \tag{8.2b}$$

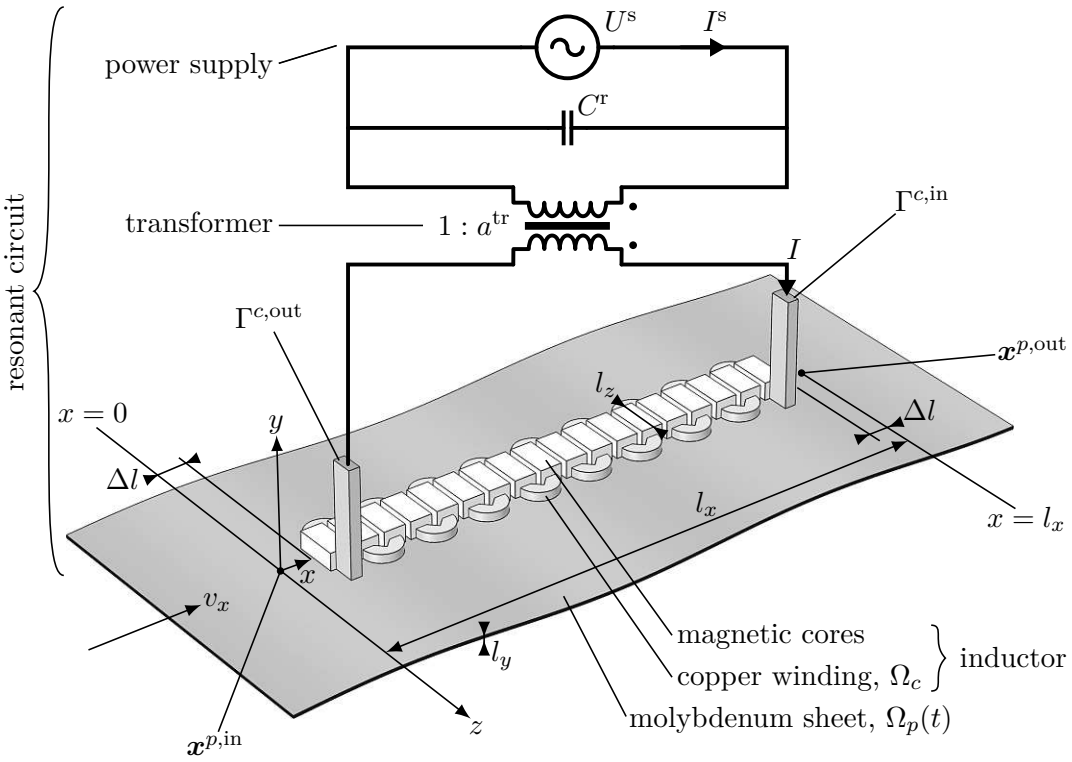

(a) Overview.

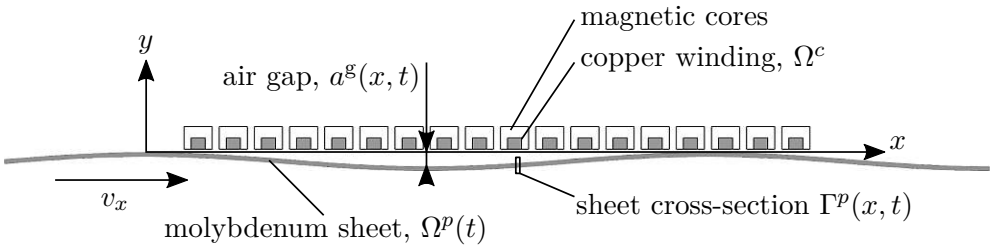

(b) Cross-sections.

Figure 8.1: Considered IH system.

and the sheet cross-sections (cf. Fig. 8.1b)

$$\Gamma^p(x,t) = \{[x',y',z'] \in \Omega^p(t) \mid x' = x\}. \tag{8.3}$$

The sheet $\Omega^p(t)$ has a thickness of l_y and moves with the (piecewise) constant velocity v_x along the direction x. The movement of the sheet entails an uncertain and time-variant air gap width between $\Omega^p(t)$ and Ω^c. In the upstream rolling process, the sheet is rolled in the direction x. Let us assume that the air gap

$$a^{\mathrm{g}}(x,t) = \operatorname{dist}(\Gamma^p(x,t), \Omega^c), \quad \Delta l < x < l_x - \Delta l \tag{8.4}$$

is independent of y and z, where $\operatorname{dist}(\cdot,\cdot)$ is the Euclidean distance between two sets.

The strip surface temperature $T|_{\partial\Omega^p(t)}$ is measured by two pyrometers on the upper surface of the sheet. At the measurement positions

$$\boldsymbol{x}^{p,\mathrm{in}}(t) = \begin{bmatrix} 0 & y^{p,\mathrm{in}}(t) & 0 \end{bmatrix}^{\mathrm{T}} \tag{8.5a}$$

$$\boldsymbol{x}^{p,\mathrm{out}}(t) = \begin{bmatrix} l_x & y^{p,\mathrm{out}}(t) & 0 \end{bmatrix}^{\mathrm{T}}, \tag{8.5b}$$

where $y^{p,\mathrm{in}}(t)$ and $y^{p,\mathrm{out}}(t)$ are the corresponding y coordinates of the upper strip surface, the pyrometers measure the temperatures

$$T^{\mathrm{in}}(t) = T|_{\boldsymbol{x}^{p,\mathrm{in}}}(t) \tag{8.6a}$$

$$T^{\mathrm{out}}(t) = T|_{\boldsymbol{x}^{p,\mathrm{out}}}(t). \tag{8.6b}$$

Remark 3. The positions $\boldsymbol{x}^{p,\mathrm{in}}$ and $\boldsymbol{x}^{p,\mathrm{out}}$ are only defined if the plate domain $\Omega^p(t)$ has yet reached the corresponding coordinates $x = 0$ and $x = l_x$, respectively.

The inductor is part of a parallel resonant circuit with a capacitor C^{r}. The capacitor and the inductor are coupled by an ideal transformer with the ratio $1 : a^{\mathrm{tr}}$. The resonant circuit is driven by an AC voltage source with adjustable RMS voltage U^{s} and angular frequency ω. The RMS voltage U^{s} and the RMS current I^{s} at the voltage source, and the RMS current I through the inductor are known from measurements.

The goal of the temperature controller is to heat the metal sheet to the desired value $T_d^{\mathrm{out}}(t)$ at the pyrometer position $\boldsymbol{x}^{p,\mathrm{out}}(t)$. The time-varying air gap is considered as an unknown disturbance since it neither can be measured nor is it known in advance. The main result of this chapter will be a control-oriented model of the IH process. It serves as a basis for the observer and controller design in Chapter 9.

8.1 Process Model

In a first step, a 3D FE model of the magnetic field is formulated and implemented in Comsol Multiphysics.

8.1.1 Electromagnetic Field

Consider Maxwell's equations for the dominant-magnetic case (see [27]), i.e., electrostatic charges and changes of the electric displacement field are neglected. With the magnetic field $\boldsymbol{H}$, the magnetic flux density $\boldsymbol{B}$, the electric field $\boldsymbol{E}$, and the current density $\boldsymbol{J}$, Maxwell's equations have the form

$$\nabla \times \boldsymbol{H} = \boldsymbol{J}, \qquad \text{in } \Omega \tag{8.7a}$$
$$\nabla \times \boldsymbol{E} = -\partial_t \boldsymbol{B}, \quad \text{in } \Omega \tag{8.7b}$$
$$\nabla \cdot \boldsymbol{B} = 0, \qquad \text{in } \Omega. \tag{8.7c}$$

Additionally, if surface currents are absent, the interface conditions on any surface Γ_{12} between two domains are

$$\boldsymbol{n}_{12} \times (\boldsymbol{H}_2 - \boldsymbol{H}_1) = \boldsymbol{0}, \quad \text{on } \Gamma_{12} \tag{8.8a}$$
$$\boldsymbol{n}_{12} \cdot (\boldsymbol{B}_2 - \boldsymbol{B}_1) = 0, \quad \text{on } \Gamma_{12}. \tag{8.8b}$$

The symbols $\boldsymbol{H}_1$, $\boldsymbol{H}_2$, $\boldsymbol{B}_1$, and $\boldsymbol{B}_2$ are the magnetic fields and flux densities on either side of the surface, while $\boldsymbol{n}_{12}$ denotes the normal direction from the first to the second domain. The constitutive equations read as

$$\boldsymbol{B} = \mu \boldsymbol{H}, \quad \text{in } \Omega \tag{8.9a}$$
$$\boldsymbol{J} = \sigma \boldsymbol{E}, \quad \text{in } \Omega \tag{8.9b}$$

where μ and σ are the magnetic permeability and the electric conductivity, respectively.

Using the magnetic vector potential $\boldsymbol{A}$ defined in the form

$$\boldsymbol{B} = \nabla \times \boldsymbol{A}, \quad \text{in } \Omega, \tag{8.10}$$

Maxwell's equations (8.7) can be reduced to

$$\nabla \times \left(\mu^{-1} \nabla \times \boldsymbol{A}\right) = \boldsymbol{J}, \qquad \text{in } \Omega \tag{8.11a}$$
$$\nabla \times \boldsymbol{E} = \nabla \times (-\partial_t \boldsymbol{A}), \quad \text{in } \Omega. \tag{8.11b}$$

According to (8.9b) and (8.11b) the current $\boldsymbol{J}$ can be partitioned into

$$\boldsymbol{J} = \sigma \boldsymbol{E} = -\sigma \partial_t \boldsymbol{A} + \boldsymbol{J}^{\text{ext}}, \quad \text{in } \Omega, \tag{8.12}$$

where the term $-\sigma \partial_t \boldsymbol{A}$ represents the induced current density and $\boldsymbol{J}^{\text{ext}}$ comprises those currents which are impressed on the system. Due to (8.11b), $\boldsymbol{J}^{\text{ext}}$ is curl-free. Also, from (8.7a), it follows that $\boldsymbol{J}$ is divergence-free. If additionally the Coulomb gauge ($\nabla \cdot \boldsymbol{A} = 0$, cf. [27]) is applied, $\boldsymbol{J}^{\text{ext}}$ is divergence-free. The divergence-free

$\boldsymbol{J}^{\text{ext}}$ represents the current that enters and leaves the field domain Ω and must sum up to the global current J^{ext} entering the inductor coil, i.e.,

$$J^{\text{ext}} = -\int_{\Gamma^{\text{c,in}}} \boldsymbol{n} \cdot \boldsymbol{J}^{\text{ext}} \, \mathrm{d}\boldsymbol{s} = \int_{\Gamma^{\text{c,out}}} \boldsymbol{n} \cdot \boldsymbol{J}^{\text{ext}} \, \mathrm{d}\boldsymbol{s}. \tag{8.13}$$

The system equations (8.11) thus take the form

$$\boldsymbol{\nabla} \times (\mu^{-1} \boldsymbol{\nabla} \times \boldsymbol{A}) = -\sigma \partial_t \boldsymbol{A} + \boldsymbol{J}^{\text{ext}}, \quad \text{in } \Omega \tag{8.14a}$$

$$-\int_{\Gamma^{\text{c,in}}} \boldsymbol{n} \cdot \boldsymbol{J}^{\text{ext}} \, \mathrm{d}\boldsymbol{s} = J^{\text{ext}}. \tag{8.14b}$$

8.1.1.1 Time-Harmonic Formulation

For IH, it is sufficient to consider time-harmonic solutions of the electromagnetic system. Therefore, the time-harmonic formulations

$$\boldsymbol{A} = \mathrm{Re}\big(\hat{\boldsymbol{A}} e^{i\omega t}\big), \quad \text{in } \Omega \tag{8.15a}$$

$$\boldsymbol{J}^{\text{ext}} = \mathrm{Re}\big(\hat{\boldsymbol{J}}^{\text{ext}} e^{i\omega t}\big), \quad \text{in } \Omega, \tag{8.15b}$$

with the imaginary unit i and the complex amplitudes $\hat{\boldsymbol{A}}$ and $\hat{\boldsymbol{J}}^{\text{ext}}$, are used. Furthermore, with the RMS value I of the current J^{ext}, the steady-state version of (8.14) reads as

$$\boldsymbol{\nabla} \times (\mu^{-1} \boldsymbol{\nabla} \times \hat{\boldsymbol{A}}) = -i\omega\sigma \hat{\boldsymbol{A}} + \hat{\boldsymbol{J}}^{\text{ext}}, \quad \text{in } \Omega \tag{8.16a}$$

$$\left| \int_{\Gamma^{\text{c,in}}} \boldsymbol{n} \cdot \hat{\boldsymbol{J}}^{\text{ext}} \, \mathrm{d}\boldsymbol{s} \right| = I\sqrt{2}. \tag{8.16b}$$

The PDE (8.16a) has to be complemented by appropriate boundary conditions.

8.1.1.2 Joule Heating

The Joule losses in a conductor are defined as

$$Q = \boldsymbol{J} \cdot \boldsymbol{E}, \quad \text{in } \Omega. \tag{8.17}$$

In the domain of the metal sheet, it holds that

$$\boldsymbol{J} = -\sigma \partial_t \boldsymbol{A}, \quad \text{in } \Omega^p \tag{8.18a}$$

$$Q = \sigma \|\partial_t \boldsymbol{A}\|_2^2, \quad \text{in } \Omega^p. \tag{8.18b}$$

From this, the average heating power during one time period $2\pi/\omega$ follows in the form

$$\frac{\omega}{2\pi} \int_{t-2\pi/\omega}^{t} Q \, \mathrm{d}t' = \frac{\sigma\omega^2}{2} \|\hat{\boldsymbol{A}}\|_2^2, \quad \text{in } \Omega^p. \tag{8.19}$$

This term will be used to describe the heat sources in the heat transfer model. In this work, the time scale of the electromagnetic field problem is several orders of magnitude faster than the heat transfer dynamics. The transient behavior of the electromagnetic field will therefore be neglected. Instead, all time dependencies of the electromagnetic quantities $\hat{\boldsymbol{A}}$, $\hat{\boldsymbol{J}}^{\text{ext}}$ and I are considered on the slower time scale of the heat transfer problem.

8.1.2 Heat Transfer

The hollow conductor Ω^c has an internal water cooling that keeps the inductor at low temperatures. It is thus assumed that the temperature of the inductor is constant (at room temperature) and heat transfer is only considered in the domain Ω^p. For this domain, the heat conduction equation with advection due to the strip movement with the velocity v_x along the direction x and the heating due to the IH reads as (cf. [26])

$$\rho c_p(\partial_t T + v_x \partial_x T) = \boldsymbol{\nabla} \cdot (\lambda \boldsymbol{\nabla} T) + \frac{\sigma \omega^2}{2} \|\hat{\boldsymbol{A}}\|_2^2, \quad \text{in } \Omega^p. \tag{8.20}$$

Here, T, ρ, c_p, and λ denote the temperature, mass density, specific heat capacity, and thermal conductivity of the strip, respectively.

Each material point of the strip stays in the magnetic field domain only for a few seconds. Due to this short time span, the losses due to radiative and convective cooling on $\partial\Omega^p$ are neglected. Using the surface normal derivative operator ∂_n, (8.20) is complemented by the boundary and initial conditions

$$T = T^{\text{in}}, \quad \text{on } \Gamma^p(0) \tag{8.21a}$$
$$-\lambda \partial_n T = 0, \quad \text{on } \partial\Gamma^p(x)|_{x\in(0,l_x]} \tag{8.21b}$$
$$T|_{t=0} = T_0, \quad \text{in } \Omega^p. \tag{8.21c}$$

8.1.3 Model Summary

In summary, the IH process model consists of the equations (8.16) with the interface conditions (8.8) combined with (8.9a) and (8.10)

$$\boldsymbol{\nabla} \times (\mu^{-1} \boldsymbol{\nabla} \times \hat{\boldsymbol{A}}) = -i\omega\sigma \hat{\boldsymbol{A}} + \hat{\boldsymbol{J}}^{\text{ext}}, \quad \text{in } \Omega \tag{8.22a}$$
$$\boldsymbol{n}_{12} \times \left(\mu_2^{-1} \boldsymbol{\nabla} \times \boldsymbol{A}_2 - \mu_1^{-1} \boldsymbol{\nabla} \times \boldsymbol{A}_1\right) = \boldsymbol{0}, \quad \text{on any } \Gamma_{12} \tag{8.22b}$$
$$\boldsymbol{n}_{12} \cdot (\boldsymbol{\nabla} \times \boldsymbol{A}_2 - \boldsymbol{\nabla} \times \boldsymbol{A}_1) = 0, \quad \text{on any } \Gamma_{12} \tag{8.22c}$$
$$\left| \int_{\Gamma^{c,\text{in}}} \boldsymbol{n} \cdot \hat{\boldsymbol{J}}^{\text{ext}} \, \mathrm{d}\boldsymbol{s} \right| = I\sqrt{2} \tag{8.22d}$$

for the electromagnetic subsystem and equations (8.20), (8.21) and (8.6b)

$$\rho c_p(\partial_t T + v_x \partial_x T) = \boldsymbol{\nabla} \cdot (\lambda \boldsymbol{\nabla} T) + \frac{\sigma\omega^2}{2} \|\hat{\boldsymbol{A}}\|_2^2, \quad \text{in } \Omega^p \tag{8.23a}$$

$$T = T^{\text{in}}, \quad \text{on } \Gamma^p(0) \tag{8.23b}$$

$$-\lambda \partial_n T = 0, \quad \text{on } \partial\Gamma^p(x)|_{x\in(0,l_x]} \tag{8.23c}$$

$$T|_{t=0} = T_0 \tag{8.23d}$$

$$T^{\text{out}} = T|_{\boldsymbol{x}^{p,\text{out}}}, \tag{8.23e}$$

for the heat transfer subsystem. This process model is solved with the finite-element (FE) software COMSOL MULTIPHYSICS. An experimental validation of the FE model along with a sensitivity analysis is given in the next section. It is shown that the exit temperature $T^{\text{out}} = T|_{\boldsymbol{x}^{p,\text{out}}}$ is highly sensitive to variations of the (unmeasured) air gap a^{g}.

8.1.4 Validation of the Process Model

For validation of the process model, a heating experiment was conducted at the industrial plant. The time-averaged measurement values are compared to the results of the process model for a quasi-stationary scenario.

8.1.4.1 Experiment

The signals ω, U^{s}, I^{s}, T^{in}, T^{out}, a^{g}, and v_x were recorded and their time averages calculated, see Table 8.1 and Fig. 8.2. The mean air gap $\overline{a}^{\text{g}}_{\text{meas}}$ and velocity

Quantity	Measurement	Max. uncertainty	Time avg.	Avg. value
ω	ω_{meas}	$\pm 2\pi \times 10\text{rad/s}$	$\overline{\omega}_{\text{meas}}$	$2\pi \times 7746\text{rad/s}$
U^{s}	$U^{\text{s}}_{\text{meas}}$	$\pm 0.5\text{V}$	$\overline{U}^{\text{s}}_{\text{meas}}$	679.5V
I^{s}	$I^{\text{s}}_{\text{meas}}$	$\pm 0.1\text{A}$	$\overline{I}^{\text{s}}_{\text{meas}}$	94.2A
T^{in}	$T^{\text{in}}_{\text{meas}}$	$\pm 5°\text{C}$	$\overline{T}^{\text{in}}_{\text{meas}}$	30°C
T^{out}	$T^{\text{out}}_{\text{meas}}$	$\pm 5°\text{C}$	$\overline{T}^{\text{out}}_{\text{meas}}$	268°C
a^{g}	$a^{\text{g}}_{\text{meas}}$	$\pm 0.5\text{mm}$	$\overline{a}^{\text{g}}_{\text{meas}}$	8.4mm
v_x	$v_{x,\text{meas}}$	$\pm 0.01\text{m/s}$	$\overline{v}_{x,\text{meas}}$	0.1m/s

Table 8.1: Data from the heating experiment.

$\overline{v}_{x,\text{meas}}$ were extracted from video data using the CANNY algorithm (see [10]). In these experiments, the current I entering the inductor (cf. Fig. 8.1a) and the phase angle ϕ^{s} between U^{s} and I^{s} were not measured. The transformer ratio $1 : a^{\text{tr}}$ is also not known exactly. These missing quantities have to be estimated before the simulation model is evaluated. For this purpose, the following inverse problem is solved.

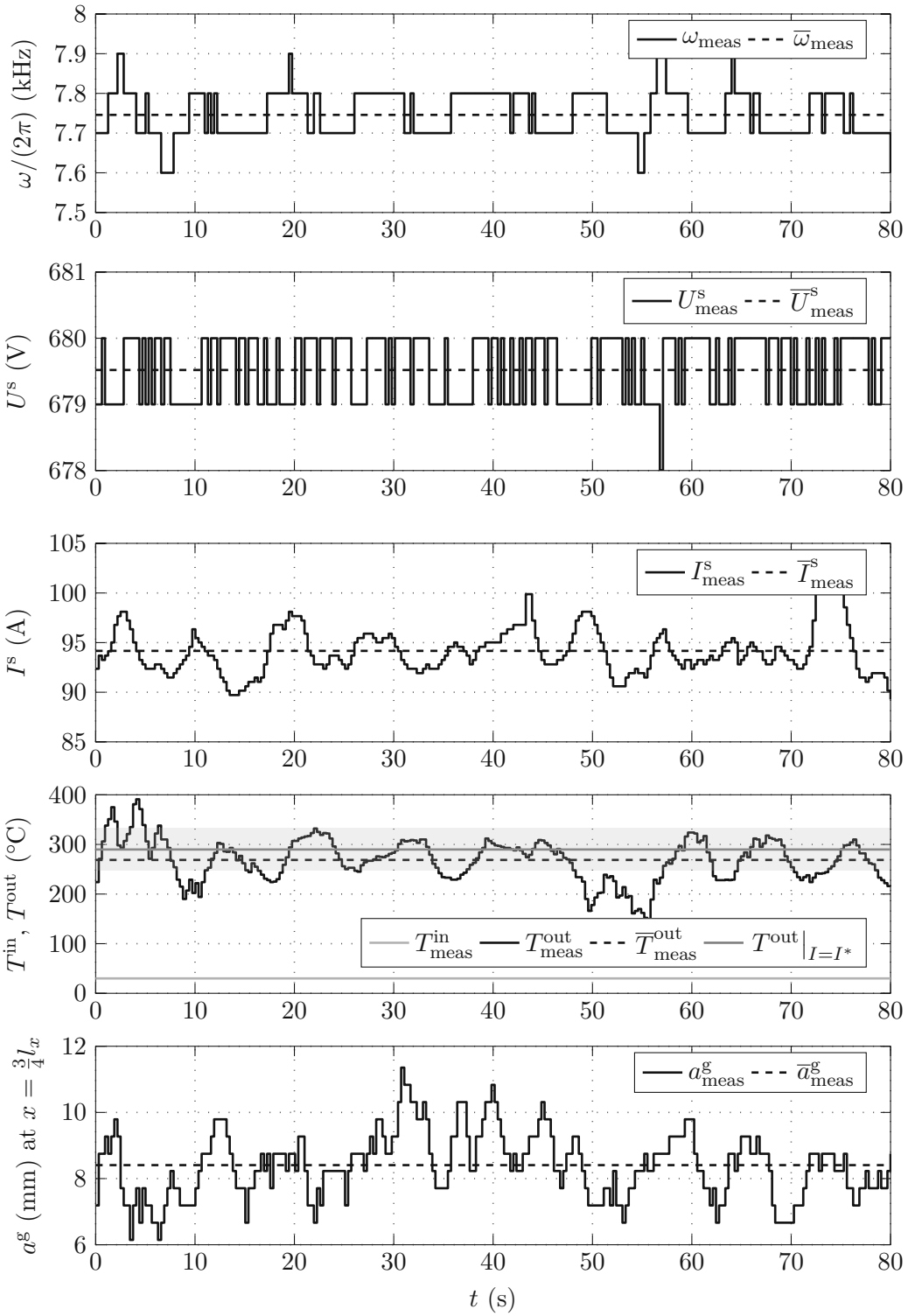

Figure 8.2: Measurement data and results for validation.

8.1.4.2 Inverse Problem

The complex power $\underline{S}^{\mathrm{s}}$ supplied by the voltage source is distributed to the capacitor and the inductor, i.e., $\underline{S}^{\mathrm{s}} = \underline{S}(I) - i\omega C^{\mathrm{r}}(U^{\mathrm{s}})^2$. Here, $\underline{S}(I)$ denotes the complex power related to the inductor, which can be computed by the FE model. The inductor current I is obtained by solving the inverse problem

$$I^* = \arg\min_{I} \left(\overline{U}^{\mathrm{s}}_{\mathrm{meas}} \overline{I}^{\mathrm{s}}_{\mathrm{meas}} - \left| \underline{S}(I) - i\omega C^{\mathrm{r}} (\overline{U}^{\mathrm{s}}_{\mathrm{meas}})^2 \right| \right)^2 \tag{8.24a}$$

$$\text{s.t.} \quad \omega = \overline{\omega}_{\mathrm{meas}}, \quad T^{\mathrm{in}} = \overline{T}^{\mathrm{in}}_{\mathrm{meas}}, \quad a^{\mathrm{g}} = \overline{a}^{\mathrm{g}}_{\mathrm{meas}}, \quad v_x = \overline{v}_{x,\mathrm{meas}} \tag{8.24b}$$

using the algorithm SNOPT (see [18]).

8.1.4.3 Validation

In steady state, the process model yields the exit temperature

$$T^{\mathrm{out}}\Big|_{I=I^*} = 290°\mathrm{C}. \tag{8.25}$$

Based on the solution of (8.24), the sensitivity

$$\left. \frac{\partial T^{\mathrm{out}}|_{I=I^*}}{\partial a^{\mathrm{g}}} \right|_{a^{\mathrm{g}}=\overline{a}^{\mathrm{g}}_{\mathrm{meas}}} \approx -86 \frac{°\mathrm{C}}{\mathrm{mm}} \tag{8.26}$$

of T^{out} with respect to a^{g} was calculated by finite differences. With the given uncertainty of 0.5mm for $a^{\mathrm{g}}_{\mathrm{meas}}$, it holds that

$$\left| \underbrace{T^{\mathrm{out}}\Big|_{I=I^*}}_{(8.25)} - \underbrace{\overline{T}^{\mathrm{out}}_{\mathrm{meas}}}_{\text{Table 8.1}} \right| = 22°\mathrm{C} < 43°\mathrm{C} = \underbrace{86 \frac{°\mathrm{C}}{\mathrm{mm}}}_{(8.26)} \times \underbrace{0.5\mathrm{mm}}_{\text{Table 8.1}}. \tag{8.27}$$

This implies that the FE model is within the uncertainties of the given measurement data and thus conforms to the recorded measurements. The simulated temperature profile is depicted in Fig. 8.3.

8.2 Control-Oriented Model

Based on the detailed process model (8.22) and (8.23), a reduced model suitable for real-time control is derived in this section.

8.2.1 Transition to Advection Equation

Using the specific enthalpy

$$h(x, y, z, t) = \int_0^{T(x,y,z,t)} \rho c_p(T') \, \mathrm{d}T', \tag{8.28}$$

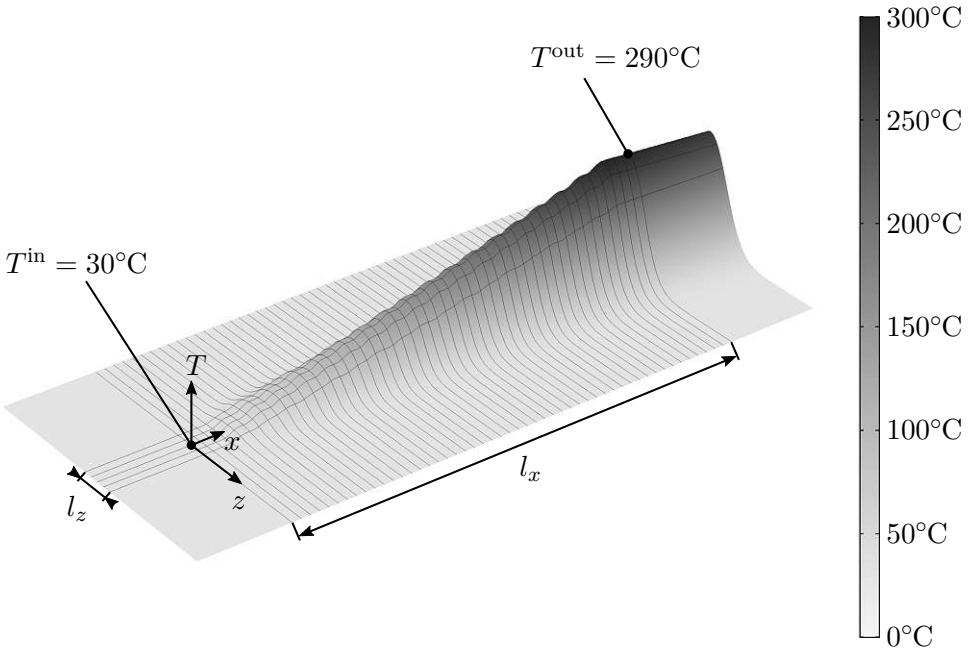

Figure 8.3: Temperature profile computed for validation of the process model.

the differential operations in (8.23) become

$$\partial_t h = \rho c_p(T)\partial_t T \tag{8.29a}$$
$$v_x \partial_x h = v_x \rho c_p(T)\partial_x T \tag{8.29b}$$
$$\boldsymbol{\nabla} h = \rho c_p(T)\boldsymbol{\nabla} T. \tag{8.29c}$$

The thermal subsystem (8.23) can therefore be reformulated as

$$\partial_t h + v_x \partial_x h = \boldsymbol{\nabla} \cdot \left(\frac{\lambda}{\rho c_p} \boldsymbol{\nabla} h \right) + \frac{\sigma \omega^2}{2} \|\hat{\boldsymbol{A}}\|_2^2, \quad \text{in } \Omega^p \tag{8.30a}$$
$$h = h^{\text{in}}(t), \quad \text{on } \Gamma^p(0) \tag{8.30b}$$
$$\partial_n h = 0, \quad \text{on } \partial\Gamma^p(x)|_{\boldsymbol{x}\in(0,l_x]} \tag{8.30c}$$
$$h|_{t=0} = h_0 \tag{8.30d}$$
$$h^{\text{out}}(t) = h|_{\boldsymbol{x}^{\text{out}}}. \tag{8.30e}$$

Based on the simulation results in Section 8.1.4 (cf. Fig. 8.3), it is assumed that on the stripe $|z| < l_z/2$ it is sufficient to consider the mean value of the temperature field (in the directions y and z). Moreover, the transport velocity v_x is high enough that the heat transfer by advection along the direction x clearly outweighs the effect of diffusion. It is therefore sufficient to consider the mean values $\overline{h}$ of h over a cross-section of this stripe. So let

$$\widetilde{\Gamma}^p(x) = \{[x', y', z'] \in \Omega^p \mid x' = x, |z'| < l_z/2\} \tag{8.31}$$

and also

$$\overline{h}(x,t) = \frac{1}{l_y l_z} \int_{\widetilde{\Gamma}^p(x)} h(x,y,z,t)\,\mathrm{d}\boldsymbol{s} \tag{8.32}$$

$$\overline{q}(x,t) = \frac{1}{l_y l_z} \int_{\widetilde{\Gamma}^p(x)} \boldsymbol{\nabla}\cdot\left(\frac{\lambda}{\rho c_p}\boldsymbol{\nabla} h\right) + \frac{\sigma\omega^2}{2}\|\hat{\boldsymbol{A}}\|_2^2\,\mathrm{d}\boldsymbol{s}. \tag{8.33}$$

The thermal subsystem (8.30) can thus be reduced to the one-dimensional advection equation

$$\partial_t \overline{h}(x,t) + v_x \partial_x \overline{h}(x,t) = \overline{q}(x,t), \quad x \in (0, l_x) \tag{8.34a}$$

$$\overline{h}(0,t) = \overline{h}^{\mathrm{in}}(t) \tag{8.34b}$$

$$\overline{h}(x,0) = \overline{h}_0(x) \tag{8.34c}$$

$$\overline{h}^{\mathrm{out}}(t) = \overline{h}(l_x,t). \tag{8.34d}$$

The source term $\overline{q}$ includes the coupling between the thermal and the electromagnetic subsystems and will be investigated next.

8.2.2 Equivalent Circuit Formulation

Consider the total heating power

$$P^p(t) = \int_0^{l_x} \int_{\widetilde{\Gamma}^p(x)} \frac{\sigma\omega^2}{2}\|\hat{\boldsymbol{A}}\|_2^2\,\mathrm{d}\boldsymbol{s}\,\mathrm{d}x, \tag{8.35}$$

the losses due to lateral diffusion

$$P^d(t) = \int_0^{l_x} \int_{\widetilde{\Gamma}^p(x)} \boldsymbol{\nabla}\cdot\left(-\frac{\lambda}{\rho c_p}\boldsymbol{\nabla} h\right)\mathrm{d}\boldsymbol{s}\,\mathrm{d}x \geq 0, \tag{8.36}$$

and the net heating power

$$P^h(t) = \int_0^{l_x} l_y l_z \overline{q}(x,t)\,\mathrm{d}x = P^p(t) - P^d(t). \tag{8.37}$$

Furthermore, consider a function $b(x,t)$ that describes the spatial distribution of $P^h(t)$ in the form

$$\overline{q}(x,t) = b(x,t)P^h(t), \quad \int_0^{l_x} l_y l_z b(x,t)\,\mathrm{d}x \equiv 1. \tag{8.38}$$

The function $b(x,t)$ strongly depends on the air gap $a^{\mathrm{g}}(x,t)$ (see (8.4)). If the air gap increases or decreases locally, then the qualitative shape of $b(x,t)$ changes accordingly. With the notions $P^p(t)$, $P^d(t)$, and $P^h(t)$ and the power distribution $b(x,t)$, the coupling of the thermal and electromagnetic subsystems can be described as follows.

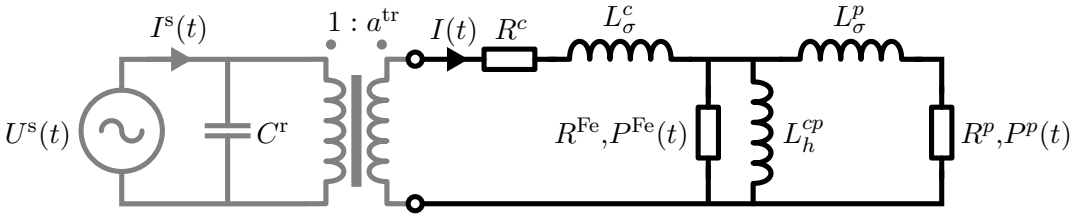

Figure 8.4: Equivalent circuit diagram of the IH system.

Consider the equivalent circuit diagram for the electromagnetic problem, shown in Fig. 8.4. The circuit represents the electromagnetic field configuration as a transformer with weak coupling. The ohmic losses in the conductor Ω^c and the sheet Ω^p (cf. Fig. 8.1a) are represented by the resistors R^c and R^p, respectively. The inductances L^c_σ and L^p_σ describe the magnetic stray fields, while L^{cp}_h refers to the coupling between the coil and the sheet. The resistor R^{Fe} accounts for losses in the magnetic concentrators and dissipates the power $P^{\mathrm{Fe}}(t)$.

Remark 4. Note that the powers $P(t)$, $P^p(t)$, $P^d(t)$, $P^h(t)$, and $P^{\mathrm{Fe}}(t)$, as well as the terms $I(t)$, $I^{\mathrm{s}}(t)$, and $U^{\mathrm{s}}(t)$ are RMS values. Their time-dependence is understood on the slower time scale of the thermal subsystem (cf. Section 8.1.1).

The electric power $P(t)$ supplied to the coil can only be dissipated by the resistors. Hence, $P(t)$ can be split into

$$\begin{aligned} P(t) &= R^c|I(t)|^2 + P^p(t) + P^{\mathrm{Fe}}(t) \\ &= R^c|I(t)|^2 + P^h(t) + \underbrace{P^d(t) + P^{\mathrm{Fe}}(t)}_{P^l(t)}. \end{aligned} \tag{8.39}$$

The losses in the magnetic concentrators $P^{\mathrm{Fe}}(t)$ and due to lateral heat diffusion $P^d(t)$ are summarized in the term $P^l(t)$.

Insertion of (8.38) into (8.34a) and consideration of (8.39) yields

$$\partial_t \overline{h}(x,t) + v_x \partial_x \overline{h}(x,t) = b(x,t)\Big(P(t) - R^c|I(t)|^2 - P^l(t)\Big). \tag{8.40}$$

The system input can be summarized as

$$u(t) = P(t) - R^c|I(t)|^2. \tag{8.41}$$

The spatial power distribution $b(x,t)$ and the power $P^l(t)$ have to be calculated or estimated. For P^l, the disturbance model

$$\frac{\mathrm{d}}{\mathrm{d}t}P^l(t) = w(t), \quad P^l(0) = P^l_0, \tag{8.42}$$

with the process noise $w(t)$ is assumed. Furthermore, the output equation (8.34d) is extended by the measurement noise $n(t)$ of the pyrometers, such that

$$\overline{h}^{\mathrm{out}}(t) = \overline{h}(l_x,t) + n(t). \tag{8.43}$$

8.2.3 Continuous-Time Model Summary

Finally, the control-oriented model takes the form

$$\partial_t \overline{h}(x,t) + v_x \partial_x \overline{h}(x,t) = b(x,t)\Big(u(t) - P^l(t)\Big), \quad x \in (0, l_x) \tag{8.44a}$$

$$\frac{\mathrm{d}}{\mathrm{d}t} P^l(t) = w(t) \tag{8.44b}$$

$$\overline{h}(0,t) = \overline{h}^{\mathrm{in}}(t) \tag{8.44c}$$

$$\overline{h}(x,0) = \overline{h}_0(x) \tag{8.44d}$$

$$P^l(0) = P_0^l \tag{8.44e}$$

$$\overline{h}^{\mathrm{out}}(t) = \overline{h}(l_x,t) + n(t). \tag{8.44f}$$

The model (8.44) does not contain any material parameters of the sheet. Transformations between the mean specific enthalpy $\overline{h}$ and the temperature T based on (8.28) can be performed outside of the control loop. Thus, the system dynamics simplifies to a linear time-varying PDE-ODE system.

The implementation of the virtual input $u(t)$ according to (8.41) requires a cascade controller. The design of such a controller, along with some stability considerations is presented in Appendix B.

8.2.4 Discrete-Time Model

The control-oriented model (8.44) is discretized in space and time using the finite volume method and the upwind scheme. Let the uniform spatial step size be $\Delta x = l_x/N$ and the constant sampling time Δt. For numerical stability, they have to satisfy the Courant-Friedrichs-Lewy condition (cf. [13])

$$C = \frac{v_x \Delta t}{\Delta x} \leq 1. \tag{8.45}$$

This yields the discrete-time model

$$\begin{bmatrix} \boldsymbol{h}_{k+1} \\ P^l_{k+1} \end{bmatrix} = \begin{bmatrix} \boldsymbol{\Phi} & -\boldsymbol{\Gamma}_k \\ \mathbf{0}^{\mathrm{T}} & 1 \end{bmatrix} \begin{bmatrix} \boldsymbol{h}_k \\ P^l_k \end{bmatrix} + \begin{bmatrix} \boldsymbol{\Gamma}_k & \boldsymbol{\Gamma}^{\mathrm{in}} \\ 0 & 0 \end{bmatrix} \begin{bmatrix} u_k \\ h^{\mathrm{in}}_k \end{bmatrix} + \begin{bmatrix} \mathbf{0} \\ \Delta t \end{bmatrix} w_k \tag{8.46a}$$

$$y_k = \boldsymbol{c}^{\mathrm{T}} \boldsymbol{h}_k + n_k, \tag{8.46b}$$

with the state vector

$$\boldsymbol{h}_k = [\overline{h}(j\Delta x, k\Delta t)]_{j=1,\ldots,N}, \quad k > 0 \tag{8.47a}$$

$$\boldsymbol{h}_0 = [\overline{h}_0(j\Delta x)]_{j=1,\ldots,N}, \tag{8.47b}$$

the system matrices

$$\boldsymbol{\Phi} = \begin{bmatrix} 1-C & 0 & 0 & \dots \\ C & 1-C & 0 & \dots \\ 0 & C & 1-C & \dots \\ \vdots & \vdots & \vdots & \ddots \end{bmatrix} \tag{8.47c}$$

$$\boldsymbol{\Gamma}_k = \left[\frac{\Delta t}{\Delta x} \int_{(j-1)\Delta x}^{j\Delta x} b(x, k\Delta t)\, \mathrm{d}x \right]_{j=1,\dots,N} \tag{8.47d}$$

$$\boldsymbol{\Gamma}^{\mathrm{in}} = \begin{bmatrix} C & 0 & 0 & \dots \end{bmatrix}^{\mathrm{T}} \tag{8.47e}$$

$$\boldsymbol{c} = \begin{bmatrix} 0 & \dots & 0 & 1 \end{bmatrix}^{\mathrm{T}}, \tag{8.47f}$$

and the signals

$$\begin{aligned} P_k^l = P^l(k\Delta t), \quad u_k = u(k\Delta t), \quad h_k^{\mathrm{in}} = \overline{h}^{\mathrm{in}}(k\Delta t), \quad y_k = \overline{h}^{\mathrm{out}}(k\Delta t), \\ w_k = w(k\Delta t), \quad n_k = n(k\Delta t). \end{aligned} \tag{8.47g}$$

A validation of the discretized control-oriented model (8.46) is performed next.

8.2.5 Validation of the Control-Oriented Model

To validate the discrete-time control-oriented model, the output of (8.46) is compared to the output of the detailed process model (8.22) and (8.23).

First, the responses $P(t)$ and $T^{\mathrm{out}}(t)$ to a step change of $I(t)$ are simulated in the process model. The parameters for the simulation are listed in Table 8.2. Additionally, the value R^c was determined from (8.22), with no sheet present in the field domain and the input $u_k = u(k\Delta t)$ of the control-oriented model was calculated according to (8.41).

The control-oriented model (8.46) was then simulated with different values of the Courant number C and the (constant) disturbance input P_k^l was tuned such that the exit temperature T^{out} in the control-oriented model corresponds to the process model at steady state.

The results are depicted in Fig. 8.5. Note that the input power $P(t)$ experiences a slight drift due to the material parameters changing with the sheet temperature. In the case of $C = 0.1$, the effects of numerical diffusion are visible around $t = 5\mathrm{s}$.

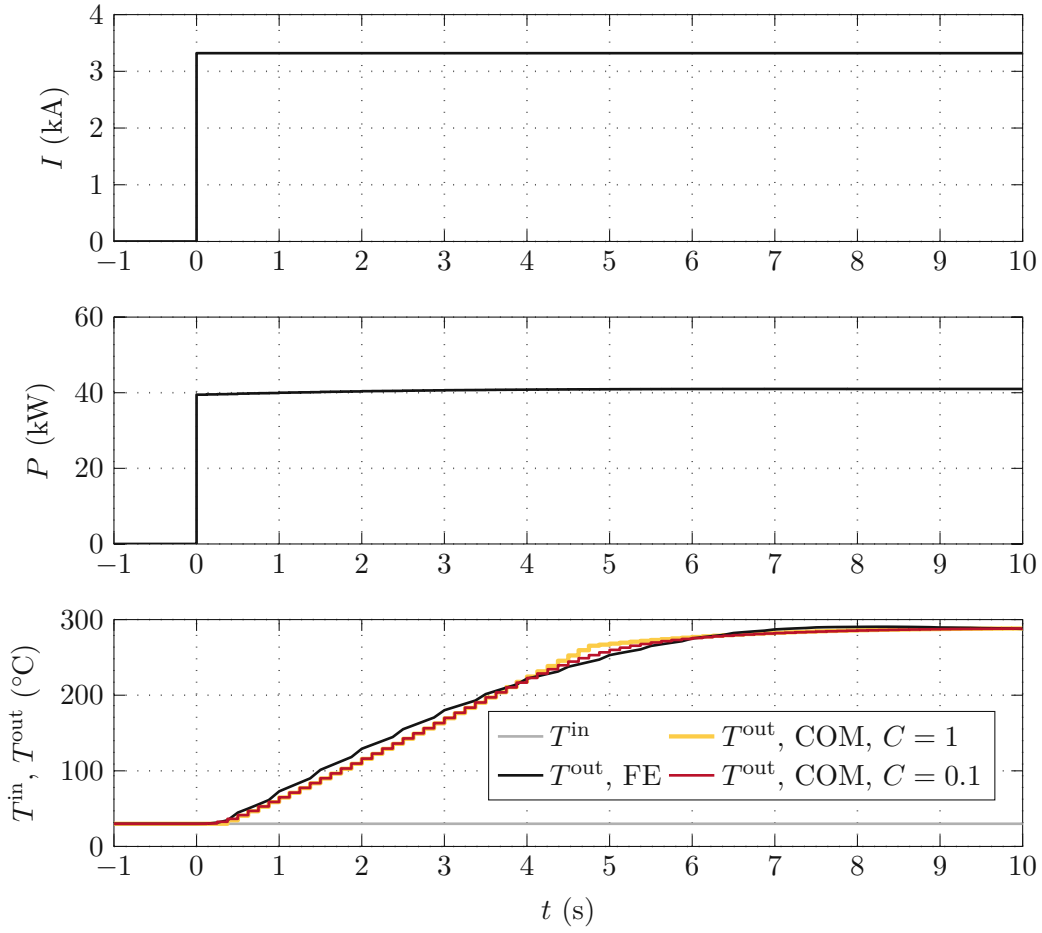

Figure 8.5: Validation of the control-oriented model (8.44): Comparison of the process model (FE) according to (8.22) and (8.23) and the control-oriented model (COM) according to (8.46).

Parameter	Symbol	Value
Sheet material	–	Mo
Sheet velocity	v_x	0.1m/s
Entry temperature	T^{in}	30°C
Source angluar frequency	ω	$2\pi \times 7746$rad/s
Input current (RMS)	$I(t),\ t > 0$	3.32kA
Air gap	a^{g}	8.4mm
Courant number, see (8.45)	C	$\{0.1, 1\}$
Disturbance input	$P_k^l,\ k > 0$	2kW
Input vector	$\mathbf{\Gamma}_k$	$\mathbf{\Gamma}$, see (9.3)
Sampling time	Δt	125ms

Table 8.2: Parameters for the validation of the control-oriented model (8.46) using the detailed process model (8.22) and (8.23).

CHAPTER 9

Controller Design

In this chapter, a 2-degrees-of-freedom (2DOF) controller is designed for the control-oriented model (8.46). To this end, the model is decomposed into a forward model, containing the known parts of the model, and an error model, containing the uncertain parts of the model. Then, a feedforward controller is designed for the forward model and a feedback controller for the error model. A first version of this control concept is already published in [55]. Additionally, an equivalent continuous-time flatness-based design of the feedforward controller can be found in Appendix C.

9.1 Decomposition

The model (8.46) is decomposed into a forward model that contains the known parts of the dynamics and an error model that contains the uncertain parts. Exploiting the linearity of (8.46), consider

$$\boldsymbol{h}_k = \boldsymbol{h}_k^{\mathrm{ff}} + \boldsymbol{h}_k^{\mathrm{fb}} \tag{9.1a}$$
$$u_k = u_k^{\mathrm{ff}} + u_k^{\mathrm{fb}} \tag{9.1b}$$
$$y_k = y_k^{\mathrm{ff}} + y_k^{\mathrm{fb}}. \tag{9.1c}$$

Moreover, assume time-independent approximations $b_0(x)$ and $\mathbf{\Gamma}$ of $b(x,t)$ and $\mathbf{\Gamma}_k$, respectively, in the form

$$b(x,t) = b_0(x) + \widetilde{b}(x,t) \tag{9.2a}$$

$$b_0(x) = \begin{cases} ((l_x - 2\Delta l) l_y l_z)^{-1}, & \Delta l < x < l_x - \Delta l \\ 0, & \text{else} \end{cases} \tag{9.2b}$$

$$1 \equiv \int_0^{l_x} l_y l_z b(x,t)\,\mathrm{d}x = \underbrace{\int_0^{l_x} l_y l_z b_0(x)\,\mathrm{d}x}_{=1} + l_y l_z \underbrace{\int_0^{l_x} \widetilde{b}(x,t)\,\mathrm{d}x}_{=0} \tag{9.2c}$$

and

$$\mathbf{\Gamma}_k = \mathbf{\Gamma} + \widetilde{\mathbf{\Gamma}}_k \tag{9.3a}$$

$$\mathbf{\Gamma} = \left[\frac{\Delta t}{\Delta x} \int_{(j-1)\Delta x}^{j\Delta x} b_0(x)\,\mathrm{d}x \right]_{j=1,\dots,N} \tag{9.3b}$$

$$\widetilde{\mathbf{\Gamma}}_k = \left[\frac{\Delta t}{\Delta x} \int_{(j-1)\Delta x}^{j\Delta x} \widetilde{b}(x, k\Delta t)\,\mathrm{d}x \right]_{j=1,\dots,N} \tag{9.3c}$$

$$1 = \frac{\Delta x l_y l_z}{\Delta t} \mathbf{1} \cdot \mathbf{\Gamma}_k = \underbrace{\frac{\Delta x l_y l_z}{\Delta t} \mathbf{1} \cdot \mathbf{\Gamma}}_{=1} + \frac{\Delta x l_y l_z}{\Delta t} \underbrace{\mathbf{1} \cdot \widetilde{\mathbf{\Gamma}}_k}_{=0}. \tag{9.3d}$$

Using (9.1) and (9.3), (8.46) can be rewritten as

$$\begin{bmatrix} \boldsymbol{h}_{k+1}^{\mathrm{ff}} + \boldsymbol{h}_{k+1}^{\mathrm{fb}} \\ P_{k+1}^{l} \end{bmatrix} = \begin{bmatrix} \mathbf{\Phi} & -\mathbf{\Gamma} - \widetilde{\mathbf{\Gamma}}_k \\ \mathbf{0}^{\mathrm{T}} & 1 \end{bmatrix} \begin{bmatrix} \boldsymbol{h}_k^{\mathrm{ff}} + \boldsymbol{h}_k^{\mathrm{fb}} \\ P_k^{l} \end{bmatrix} + \\ + \begin{bmatrix} \mathbf{\Gamma} + \widetilde{\mathbf{\Gamma}}_k & \mathbf{\Gamma}^{\mathrm{in}} \\ 0 & 0 \end{bmatrix} \begin{bmatrix} u_k^{\mathrm{ff}} + u_k^{\mathrm{fb}} \\ h_k^{\mathrm{in}} \end{bmatrix} + \begin{bmatrix} \mathbf{0} \\ \Delta t \end{bmatrix} w_k \tag{9.4a}$$

and

$$y_k^{\mathrm{ff}} + y_k^{\mathrm{fb}} = \boldsymbol{c}^{\mathrm{T}} \left(\boldsymbol{h}_k^{\mathrm{ff}} + \boldsymbol{h}_k^{\mathrm{fb}} \right) + n_k. \tag{9.4b}$$

Now, define the forward system

$$\boldsymbol{h}_{k+1}^{\mathrm{ff}} = \mathbf{\Phi} \boldsymbol{h}_k^{\mathrm{ff}} + \mathbf{\Gamma} u_k^{\mathrm{ff}} + \mathbf{\Gamma}^{\mathrm{in}} h_k^{\mathrm{in}}, \quad \boldsymbol{h}_0^{\mathrm{ff}} = \boldsymbol{h}_0 \tag{9.5a}$$

$$y_k^{\mathrm{ff}} = \boldsymbol{c}^{\mathrm{T}} \boldsymbol{h}_k^{\mathrm{ff}}. \tag{9.5b}$$

Subtraction of (9.5) from (9.4) yields the error system

$$\begin{bmatrix} \boldsymbol{h}_{k+1}^{\mathrm{fb}} \\ P_{k+1}^{l} \end{bmatrix} = \begin{bmatrix} \mathbf{\Phi} & -\mathbf{\Gamma}_k \\ \mathbf{0}^{\mathrm{T}} & 1 \end{bmatrix} \begin{bmatrix} \boldsymbol{h}_k^{\mathrm{fb}} \\ P_k^{l} \end{bmatrix} + \begin{bmatrix} \widetilde{\mathbf{\Gamma}}_k & \mathbf{\Gamma}_k \\ 0 & 0 \end{bmatrix} \begin{bmatrix} u_k^{\mathrm{ff}} \\ u_k^{\mathrm{fb}} \end{bmatrix} + \begin{bmatrix} \mathbf{0} \\ \Delta t \end{bmatrix} w_k, \quad \boldsymbol{h}_0^{\mathrm{fb}} = \mathbf{0} \tag{9.6a}$$

$$y_k^{\mathrm{fb}} = \boldsymbol{c}^{\mathrm{T}} \boldsymbol{h}_k^{\mathrm{fb}} + n_k, \tag{9.6b}$$

which contains the unknown parts of (8.46). Note that the term $\widetilde{\mathbf{\Gamma}}_k u_k^{\mathrm{ff}}$ in (9.6) represents a coupling to the forward system. In the next section, feedforward (FF) and feedback (FB) controllers will be designed for the forward system and the error system, respectively, to control the exit temperature of the sheet.

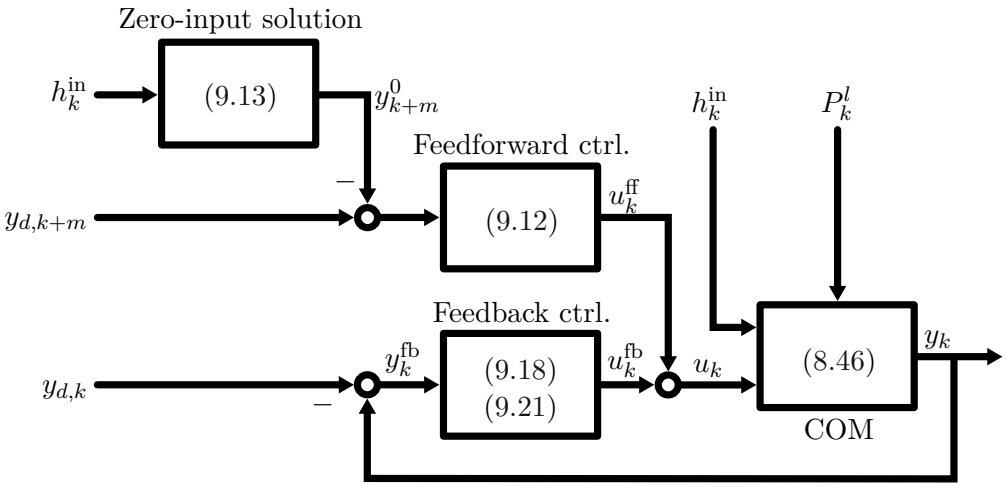

Figure 9.1: 2DOF control structure for the control-oriented model (COM) of the IH system.

9.2 Temperature Control

For output tracking control of (8.46), the 2DOF controller structure shown in Fig. 9.1 is designed in this section.

9.2.1 Feedforward Controller

The forward system (9.5) is a disturbance-free LTI system. Its input-output representation can be written as

$$y_k^{\text{ff}} = G_{uy}(\delta)u_k^{\text{ff}} + \underbrace{\boldsymbol{c}^{\text{T}}(\delta\boldsymbol{I} - \boldsymbol{\Phi})^{-1}\Big(\boldsymbol{h}_0\delta_{k+1} + \boldsymbol{\Gamma}^{\text{in}}h_k^{\text{in}}\Big)}_{=y_k^0}, \tag{9.7}$$

with the forward time shift operator δ for one sampling interval, i.e.,

$$\delta y_k = y_{k+1}, \tag{9.8}$$

the discrete-time impulse

$$\delta_k = \begin{cases} 1 & \text{if } k = 0 \\ 0 & \text{else,} \end{cases} \tag{9.9}$$

the identity matrix $\boldsymbol{I}$, and the transfer function operator from u_k^{ff} to y_k^{ff}

$$G_{uy}(\delta) = \boldsymbol{c}^{\text{T}}(\delta\boldsymbol{I} - \boldsymbol{\Phi})^{-1}\boldsymbol{\Gamma}. \tag{9.10}$$

Choosing y_k^{ff} equal to the desired output $y_{d,k}$ yields the FF control law

$$u_k^{\text{ff}} = G_{uy}^{-1}(\delta)\Big(y_{d,k} - y_k^0\Big), \tag{9.11}$$

which is generally not proper (i.e., not causal)[1] because there is a delay of m (≥ 1) time steps between the input u_k^{ff} and the response y_k^{ff} at the output of the system. Still, the FF controller (9.11) can be realized because the future reference input $y_{d,k}$ is known in advance and also the zero-input solution y_k^0 can be obtained up to N ($> m$) time steps earlier. The FF control law (9.11) can hence be reformulated as

$$u_k^{\mathrm{ff}} = \left(\delta^{-m} G_{uy}^{-1}(\delta)\right)\left(y_{d,k+m} - y_{k+m}^0\right) \tag{9.12}$$

where $\delta^{-m} G_{uy}^{-1}(\delta)$ is proper. Likewise, y_{k+m}^0 is obtained in the form

$$y_{k+m}^0 = \delta^m \boldsymbol{c}^{\mathrm{T}} (\delta \boldsymbol{I} - \boldsymbol{\Phi})^{-1} \left(\boldsymbol{h}_0 \delta_{k+1} + \boldsymbol{\Gamma}^{\mathrm{in}} h_k^{\mathrm{in}}\right). \tag{9.13}$$

The error $y_k^{\mathrm{fb}} = y_k - y_{d,k}$ is passed to a FB controller, which is designed in the following.

9.2.2 Feedback Controller

The error system (9.6) can be rewritten in the form

$$\begin{bmatrix} \boldsymbol{h}_{k+1}^{\mathrm{fb}} \\ P_{k+1}^l \end{bmatrix} = \begin{bmatrix} \boldsymbol{\Phi} & -\boldsymbol{\Gamma} \\ \boldsymbol{0}^{\mathrm{T}} & 1 \end{bmatrix} \begin{bmatrix} \boldsymbol{h}_k^{\mathrm{fb}} \\ P_k^l \end{bmatrix} + \begin{bmatrix} \boldsymbol{\Gamma} \\ 0 \end{bmatrix} u_k^{\mathrm{fb}} + \begin{bmatrix} \widetilde{\boldsymbol{\Gamma}}_k \\ 0 \end{bmatrix} (\underbrace{u_k^{\mathrm{ff}} + u_k^{\mathrm{fb}}}_{u_k} - P_k^l) + \begin{bmatrix} \boldsymbol{0} \\ \Delta t \end{bmatrix} w_k, \quad \boldsymbol{h}_0^{\mathrm{fb}} = \boldsymbol{0} \tag{9.14a}$$

$$y_k^{\mathrm{fb}} = \boldsymbol{c}^{\mathrm{T}} \boldsymbol{h}_k^{\mathrm{fb}} + n_k, \tag{9.14b}$$

with the unknown disturbance input $\widetilde{\boldsymbol{\Gamma}}_k (u_k - P_k^l)$. Two possible options to handle the disturbance are:

1. Assume that $\widetilde{\boldsymbol{\Gamma}}_k (u_k - P_k^l)$ has only a minor influence on the evolution of $\boldsymbol{h}_k^{\mathrm{fb}}$ and consider (cf. [55])

$$\begin{bmatrix} \boldsymbol{h}_{k+1}^{\mathrm{fb}} \\ P_{k+1}^l \end{bmatrix} = \begin{bmatrix} \boldsymbol{\Phi} & -\boldsymbol{\Gamma} \\ \boldsymbol{0}^{\mathrm{T}} & 1 \end{bmatrix} \begin{bmatrix} \boldsymbol{h}_k^{\mathrm{fb}} \\ P_k^l \end{bmatrix} + \begin{bmatrix} \boldsymbol{\Gamma} \\ 0 \end{bmatrix} u_k^{\mathrm{fb}} + \begin{bmatrix} \boldsymbol{0} \\ \Delta t \end{bmatrix} w_k, \quad \boldsymbol{h}_0^{\mathrm{fb}} = \boldsymbol{0} \tag{9.15a}$$

$$y_k^{\mathrm{fb}} = \boldsymbol{c}^{\mathrm{T}} \boldsymbol{h}_k^{\mathrm{fb}} + n_k. \tag{9.15b}$$

2. Regard $\widetilde{\boldsymbol{\Gamma}}_k (u_k - P_k^l)$ as process noise and consider

$$\begin{bmatrix} \boldsymbol{h}_{k+1}^{\mathrm{fb}} \\ P_{k+1}^l \end{bmatrix} = \begin{bmatrix} \boldsymbol{\Phi} & -\boldsymbol{\Gamma} \\ \boldsymbol{0}^{\mathrm{T}} & 1 \end{bmatrix} \begin{bmatrix} \boldsymbol{h}_k^{\mathrm{fb}} \\ P_k^l \end{bmatrix} + \begin{bmatrix} \boldsymbol{\Gamma} \\ 0 \end{bmatrix} u_k^{\mathrm{fb}} + \Delta t \boldsymbol{w}_k^e, \quad \boldsymbol{h}_0^{\mathrm{fb}} = \boldsymbol{0} \tag{9.16a}$$

$$y_k^{\mathrm{fb}} = \boldsymbol{c}^{\mathrm{T}} \boldsymbol{h}_k^{\mathrm{fb}} + n_k, \tag{9.16b}$$

with the extended process noise term $\boldsymbol{w}_k^e$.

[1] Due to the distance Δl from the coil to the output temperature pyrometer at the position $\boldsymbol{x}^{p,\mathrm{out}}$, see Fig. 8.1a, the output is delayed by a dead time of $m\Delta t$, with $m = \lfloor \Delta l / (v_x \Delta t) \rfloor + 1$ and the floor operator $\lfloor \cdot \rfloor$.

Here, option 1 is a special case of option 2. Therefore, option 2 will be pursued in the following and a FB controller will be designed for (9.16). The task for the FB controller is now to control the output y_k^{fb} of the simplified error system (9.16). In order to estimate and compensate P_k^l in (9.16), a linear-quadratic-Gaussian (LQG) controller consisting of a Kalman filter and a linear-quadratic regulator (LQR) will be designed.

9.2.2.1 Observer

The observability of (9.16) can be easily proven, e.g., by an eigenvector test. For the design of a Kalman filter for (9.16), let $\hat{\boldsymbol{x}}_k^e = \begin{bmatrix}(\hat{\boldsymbol{h}}_k^{\mathrm{fb}})^{\mathrm{T}} & \hat{P}_k^l\end{bmatrix}^{\mathrm{T}}$ be the estimated values of $\boldsymbol{h}_k^{\mathrm{fb}}$ and P_k^l. With

$$\begin{gathered}\boldsymbol{\Phi}^e = \begin{bmatrix}\boldsymbol{\Phi} & -\boldsymbol{\Gamma}\\ \boldsymbol{0}^{\mathrm{T}} & 1\end{bmatrix}, \quad \boldsymbol{\Gamma}^e = \begin{bmatrix}\boldsymbol{\Gamma}\\ 0\end{bmatrix}, \quad \boldsymbol{G}^e = \begin{bmatrix}\boldsymbol{I}\Delta t & \boldsymbol{0}\\ \boldsymbol{0}^{\mathrm{T}} & \Delta t\end{bmatrix}, \quad \boldsymbol{c}^e = \begin{bmatrix}\boldsymbol{c}\\ 0\end{bmatrix},\\ \boldsymbol{Q}^e = \operatorname{cov} \boldsymbol{w}_k^e = \begin{bmatrix}\boldsymbol{I}Q_1^e & \boldsymbol{0}\\ \boldsymbol{0}^{\mathrm{T}} & Q_2^e\end{bmatrix}, \quad R^e = \operatorname{cov} n_k,\end{gathered} \tag{9.17}$$

the steady-state Kalman filter reads as

$$\hat{\boldsymbol{x}}_{k+1}^e = \boldsymbol{\Phi}^e \hat{\boldsymbol{x}}_k^e + \boldsymbol{\Gamma}^e u_k^{\mathrm{fb}} + \hat{\boldsymbol{K}}^e (y_k^{\mathrm{fb}} - (\boldsymbol{c}^e)^{\mathrm{T}} \hat{\boldsymbol{x}}_k^e), \quad \hat{\boldsymbol{x}}_0^e = \boldsymbol{0}. \tag{9.18}$$

The gain vector $\hat{\boldsymbol{K}}^e$ follows from the algebraic Riccati equation

$$\boldsymbol{P}^e = \boldsymbol{\Phi}^e \boldsymbol{P}^e (\boldsymbol{\Phi}^e)^{\mathrm{T}} + \boldsymbol{G}^e \boldsymbol{Q}^e (\boldsymbol{G}^e)^{\mathrm{T}} - \hat{\boldsymbol{K}}^e (\boldsymbol{c}^e)^{\mathrm{T}} \boldsymbol{P}^e (\boldsymbol{\Phi}^e)^{\mathrm{T}} \tag{9.19a}$$

$$\hat{\boldsymbol{K}}^e = \boldsymbol{\Phi}^e \boldsymbol{P}^e \boldsymbol{c}^e \left((\boldsymbol{c}^e)^{\mathrm{T}} \boldsymbol{P}^e \boldsymbol{c}^e + R^e \right)^{-1}. \tag{9.19b}$$

The positive parameters Q_1^e, Q_2^e and R^e serve as tuning factors for the Kalman filter.

9.2.2.2 Controller

For the feedback (FB) controller design, consider the disturbance-free reduced error system

$$\boldsymbol{h}_{k+1}^{\mathrm{fb}} = \boldsymbol{\Phi} \boldsymbol{h}_k^{\mathrm{fb}} + \boldsymbol{\Gamma} u_k^{\mathrm{fb}} \tag{9.20a}$$

$$y_k^{\mathrm{fb}} = \boldsymbol{c}^{\mathrm{T}} \boldsymbol{h}_k^{\mathrm{fb}}. \tag{9.20b}$$

A steady-state LQR with disturbance feedforward

$$u_k^{\mathrm{fb}} = \boldsymbol{K}^{\mathrm{T}} \hat{\boldsymbol{h}}_k^{\mathrm{fb}} + \hat{P}_k^l \tag{9.21}$$

is designed, where the FB gain $\boldsymbol{K}$ satisfies the algebraic Riccati equation

$$\boldsymbol{P} = \boldsymbol{c} Q \boldsymbol{c}^{\mathrm{T}} + \boldsymbol{\Phi}^{\mathrm{T}} \boldsymbol{P} \boldsymbol{\Phi} - \left(\boldsymbol{\Gamma}^{\mathrm{T}} \boldsymbol{P} \boldsymbol{\Phi} \right)^{\mathrm{T}} \boldsymbol{K}^{\mathrm{T}} \tag{9.22a}$$

$$\boldsymbol{K}^{\mathrm{T}} = -\left(R + \boldsymbol{\Gamma}^{\mathrm{T}} \boldsymbol{P} \boldsymbol{\Gamma} \right)^{-1} \boldsymbol{\Gamma}^{\mathrm{T}} \boldsymbol{P} \boldsymbol{\Phi}, \tag{9.22b}$$

with the positive tuning factors Q and R.

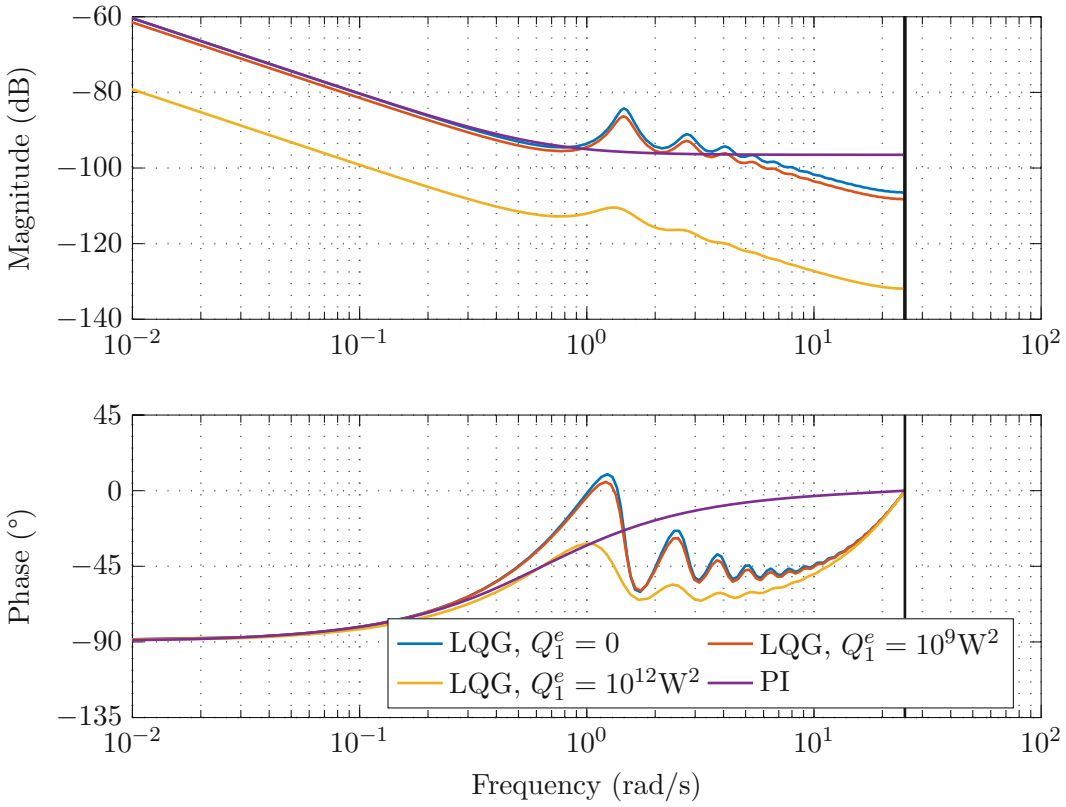

Figure 9.2: Bode plots of the designed LQG FB controller (LQG) for different values of Q_1^e and the first-order approximation (PI); $v_x = 0.1\mathrm{m/s}$, $N = 40$, $\Delta t = 0.125\mathrm{s}$, $Q_2^e = 1\mathrm{W}^2$, $R^e = 10^9(\mathrm{J/m^3})^2$, $Q = 1(\mathrm{m^3/s})^2$, $R = 10^9$.

9.2.2.3 Controller Order Reduction

The designed LQG controller (9.18) and (9.21) is a dynamic system of dimension $N+1$, see (8.46). Since the controller is an LTI system, it is worth examining the bode plot from the input y_k^{fb} to the output u_k^{fb} and look for possible simplifications.

A standard method for linear model-order reduction, in terms of the input-output behavior, is balanced truncation. Figure 9.2 shows the bode plot of the LQG controller ((9.18) and (9.21)) for different values of the tuning parameter Q_1^e along with a first-order approximation for $Q_1^e = 0$ calculated by balanced truncation.

It can be seen that the full-order LQG controller consists of an integral part and resonance peaks to compensate for the typical harmonic zeros of a delay system. With increasing value of Q_1^e, the resonant peaks and the overall gain of the LQG controller decreases. Likewise, the small phase lead around the inverse of the transport time ($2\pi v_x/l_x$) gets smaller when Q_1^e increases.

The first-order approximation adopts the integral behavior and exerts a constant proportional gain at higher frequencies, evening out the resonant peaks. The

2DOF-LQG controller and the first-order approximation for $Q_1^e = 0$, i.e., a 2DOF proportional-integral (PI) controller, will be compared in Chapter 10. We choose the value $Q_1^e = 0$ to best illustrate the qualitative behavior of the FB controller.

9.3 Controller Extension for Charge and Exit

In the considered IH process, thin sheets of refractory metal with leading and trailing ends are reheated. It can therefore be the case that

1. there is no sheet in the field domain,
2. there is a sheet entering the field domain and the leading edge is somewhere under the inductor,
3. there is a sheet covering the entire field domain, or
4. there is a sheet leaving the field domain and the trailing edge is somewhere under the inductor.

So far, the designed 2DOF controller only deals with Item 3 of this list. In the following, the necessary extensions of the controller for plate position estimation and temperature control during charge (Item 2) and exit (Item 4) are discussed.

9.3.1 Estimation of the Sheet Position

In a first step, the sheet position will be estimated. To this end, a nonlinear integrator is implemented for the positions x_k^{h} and x_k^{t} of the leading and trailing edges, respectively. Using the definition (8.3) of spatially fixed sheet cross-sections $\Gamma^p(x,t)$, let

$$\delta_k^{\mathrm{in}} = \begin{cases} 0, & \text{if } \Gamma^p(0, k\Delta t) = \emptyset \\ 1, & \text{else} \end{cases} \tag{9.23a}$$

$$\delta_k^{\mathrm{out}} = \begin{cases} 0, & \text{if } \Gamma^p(l_x, k\Delta t) = \emptyset \\ 1, & \text{else} \end{cases} \tag{9.23b}$$

be flags to indicate if the sheet is visible for either of the pyrometers at $x \in \{0, l_x\}$. The estimated position $\hat{x}_k^{\mathrm{h}}$ of the leading edge then follows from the difference equation

$$\hat{x}_{k+1}^{\mathrm{h}} = \begin{cases} \hat{x}_0^{\mathrm{h}}, & \text{if } \delta_k^{\mathrm{in}} = 0 \ \wedge \ \delta_k^{\mathrm{out}} = 0 \\ \min\{\hat{x}_k^{\mathrm{h}} + v_x \Delta t, l_x\}, & \text{else} \end{cases} \tag{9.24a}$$

$$\hat{x}_0^{\mathrm{h}} = 0. \tag{9.24b}$$

Likewise, for the estimated position $\hat{x}_k^{\mathrm{t}}$ of the trailing edge, define

$$\hat{x}_{k+1}^{\mathrm{t}} = \begin{cases} \min\{\hat{x}_k^{\mathrm{t}} + v_x \Delta t, l_x\}, & \text{if } \delta_k^{\mathrm{in}} = 0 \ \wedge \ \delta_k^{\mathrm{out}} = 1 \\ \hat{x}_0^{\mathrm{t}}, & \text{else} \end{cases} \tag{9.25a}$$

$$\hat{x}_0^{\mathrm{t}} = 0. \tag{9.25b}$$

The ramp-shaped signals $\hat{x}_k^{\mathrm{h}}$ and $\hat{x}_k^{\mathrm{t}}$ are used to calculate the part κ_k of the inductor that currently covers the sheet. This part reads as

$$\kappa_k = \mathrm{sat}\left(\frac{\hat{x}_k^{\mathrm{h}} - \Delta l}{l_x - 2\Delta l}\right) - \mathrm{sat}\left(\frac{\hat{x}_k^{\mathrm{t}} - \Delta l}{l_x - 2\Delta l}\right), \quad \mathrm{sat}(\xi) = \begin{cases} 0, & \text{if } \xi < 0 \\ \xi, & \text{if } 0 \leq \xi < 1 \\ 1, & \text{if } 1 \leq \xi. \end{cases} \tag{9.26}$$

In the next step, the signals δ_k^{in}, δ_k^{out}, and κ_k will serve for a switching criterion between normal operation when the sheet covers the entire field domain, charge, exit, and idle operation.

9.3.2 Temperature Controller Extension

The 2DOF temperature controller is based on the model of a sheet that covers the entire field domain. If there is no sheet at the exit of the IH system, the output signal y_k is not valid and the FB controller cannot be used. If the sheet is not covering the whole inductor, the FF signal u_k^{ff} must be appropriately scaled.

A simple yet effective adaption of the 2DOF controller to the varying coverage of the sheet in the field domain is shown in Fig. 9.3. The feedforward input u_k^{ff} is scaled with κ_k, which makes sense because $\mathbf{\Gamma}$ was chosen to be uniform along the inductor coil (cf. (9.3)). Additionally, the FB controller is enabled as soon as the leading edge of the plate reaches the exit pyrometer, i.e., $\delta_k^{\mathrm{out}} = 1$ and is disabled when the plate has left the field domain, i.e., $\kappa_k = 0$.

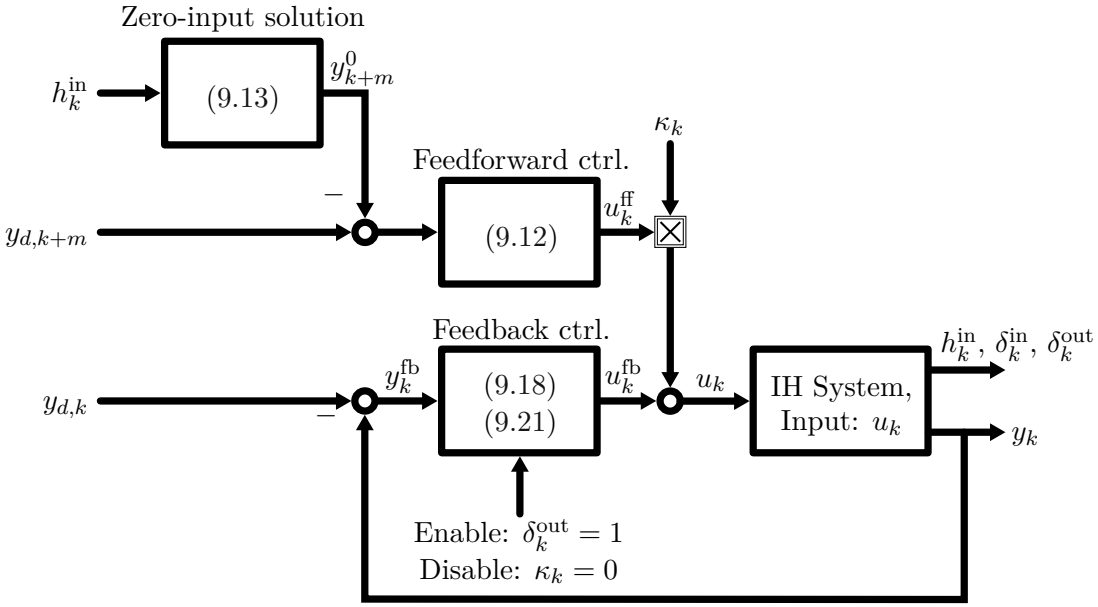

Figure 9.3: Extended 2DOF control structure for the IH system.

CHAPTER 10

Results and Performance

For the purpose of evaluation, the validated finite-element (FE) model from Section 8.1.3 was embedded in a MATLAB/SIMULINK model and connected to the designed temperature controller according to Fig. 9.3. To save computation time, a 2D implementation in the xy-plane was used instead of a 3D implementation. Following the considerations of Section 8.2.1, this approach should be sufficiently accurate for testing the performance of the closed-loop system.

In the current chapter, the proposed 2-degrees-of-freedom (2DOF) controller is compared to other control concepts in different simulation experiments based on a specific test scenario. The test scenario is defined based on the assumptions made for the controller design and the performance is evaluated for different sets of parameter values.

10.1 Test Scenario and Experiments

For the FB controller design in Section 9.2.2, the influence of the unknown power distribution $\widetilde{b}(x,t)$, see (9.2), or its discretized counterpart $\widetilde{\mathbf{\Gamma}}_k$, see (9.3), was regarded as process noise. It is expected that this assumption will be the major source of disturbance for the control concept. Therefore, the following test scenario aims at generating significant process disturbances via $\widetilde{b}(x,t)$, or $\widetilde{\mathbf{\Gamma}}_k$, by varying the air gap $a^{\mathrm{g}}(x,t)$.

The air gap $a^{\mathrm{g}}(x,t)$ used in the FE model can vary in space and time. The special case $a^{\mathrm{g}}(t)$, where the air gap is only time dependent, corresponds to a perfectly homogeneous air gap. In this case, $\widetilde{b}$ depends only on t, and due to (9.2) reduces to zero.

Likewise, if the air gap varies only in space, i.e., $a^{\mathrm{g}}(x)$, the profile $\widetilde{b}$ depends

only on x. In this special case, every material point of the metal sheet experiences the same evolution of a^{g} over time. A situation like this is easily controlled by the integral part of the designed 2DOF controller.

In conclusion, the coupled space-time-dependence of $\widetilde{b}$ plays an important role in testing the performance of the proposed controller. Therefore, let

$$a^{\mathrm{g}}(x,t) = a_0^{\mathrm{g}} - \hat{a}^{\mathrm{g}} \cos(k^{\mathrm{g}}(x - v_x t) + \phi^{\mathrm{g}}). \tag{10.1}$$

The parameters k^{g} and $\hat{a}^{\mathrm{g}}$ will be varied in the simulation scenario. Thereby, it has to be considered that $\hat{a}^{\mathrm{g}}$ is limited by the geometry of the surrounding parts, i.e., the gap between the inductor and the roller table for the sheet.

Five experiments are defined to test the controller performance. The parameters are given in Table 10.1.

Parameter		Experiments				
Name	Symbol	Exp. 1	Exp. 2	Exp. 3	Exp. 4	Exp. 5
Inductor length	l_x	0.5m				
Sheet length	–	8.5m				
Entry/exit dist.	Δl	27.5mm				
Mean air gap	a_0^{g}	7.5mm				
Air gap amplitude	$\hat{a}^{\mathrm{g}}$	0	5.0mm			
Angular wavenumber	k^{g}	$0\mathrm{m}^{-1}$	$2\pi/4\mathrm{m}$	$2\pi/2\mathrm{m}$	$2\pi/1\mathrm{m}$	$2\pi/2\mathrm{m}$
Phase offset	ϕ^{g}	0°	54°	108°	216°	108°
Sheet velocity	v_x	0.1m/s				
Sampling time	Δt	0.125s				
Courant number	C	1				
Output noise variance	$\mathrm{cov}\, T_k^{\mathrm{out}}$	0				$(15°\mathrm{C})^2$

Table 10.1: Simulation parameters for the test runs.

Measurement noise is expected to be relevant only at the exit of the inductors. The measurement noise is expected to be white Gaussian noise. The variance is derived from the specification of the used pyrometer. At the entrance, a homogeneous temperature is expected, which can be averaged and should be well known due to previous temperature measurements in the upstream rolling process. Remaining measurement offsets will be compensated by the integral controller.

Other disturbances due to parameter uncertainties are not an issue, because all necessary parameters, i.e., ρ^p, c_p^p, and v_x are well known. Also, constraints on the input power are not regarded, since the considered inductors are designed for input powers up to 120kW, which by far exceeds the required heating power.

10.2 Simulation Results and Evaluation

The designed 2DOF linear-quadratic-Gaussian (LQG) controller from Section 9.2.2 is compared to two proportional-integral (PI) controllers. The first one is a simple 1DOF PI controller tuned for the system (9.5) with $R^c = 0$ (i.e., $u_k = P_k$). The second one is the 2DOF PI controller derived in Section 9.2.2.3.

Experiment 1: Perfectly flat sheet The results for all three controllers are shown in Fig. 10.1. Since the considered sheet is perfectly flat, the integral parts of each controller asymptotically stabilize the error $(T_k^{\text{out}} - T_{d,k}^{\text{out}})$ in the exit temperature. The overheating of the leading and trailing ends is typical for so-called edge- or end effects of induction heating.

The 2DOF controllers utilize a cascade controller to implement $P_k = u_k + R^c I_k^2$ (see Appendix B), while the 1DOF-PI controller uses $P_k = u_k$. Accordingly, the values of u_k differ between the 1DOF and 2DOF controllers.

The contribution u_k^{ff} of the feedforward branch of the 2DOF controllers is shown separately in the plots of u_k. The 1DOF-PI controller integrates freely while the leading edge of the sheet travels through the field domain from $t = 1$s to $t = 6$s. Due to the temperature peaks caused by end effects, the feedback controllers produce negative steps when the sheet edges pass the exit pyrometer at $t = 6$s and $t = 91$s.

Experiment 2: Wavelength 4m The results are shown in Fig. 10.2. The proposed 2DOF controller keeps the output error $T_k^{\text{out}} - T_{d,k}^{\text{out}}$ within a tolerance of ± 10°C after a short settling time. Also, the reduced 2DOF PI controller provides very similar results. The 1DOF PI controller performs significantly worse, because it can only react to temperature control errors when they are measured by the exit pyrometer.

The maxima of the input power P_k are synchronized with the maxima of the (mean) air gap a^{g}. This implies that the underlying power controller of the 2DOF controllers, which transforms the virtual input u_k into the input power P_k, is able to compensate for variations in the mean value of the air gap a^{g}.

The feedback controllers can only compensate for static or slowly-varying output errors. In the case of the 1DOF PI controller, this leads to a delay of $(l_x - \Delta l)/v_x$ (≈ 5s) in the supplied heating power P_k. This shows that the feedforward part of the proposed 2DOF controller and the introduction of the virtual input u_k are key components of this approach.

Experiment 3: Wavelength 2m Figure 10.3 shows the results of this experiment for all three controllers. The qualitative behavior of all tested controllers is the same as in experiment 3. However, since the design of the feedback controllers was based on the assumption of a homogeneous air gap a^{g}, the error $T_k^{\text{out}} - T_{d,k}^{\text{out}}$

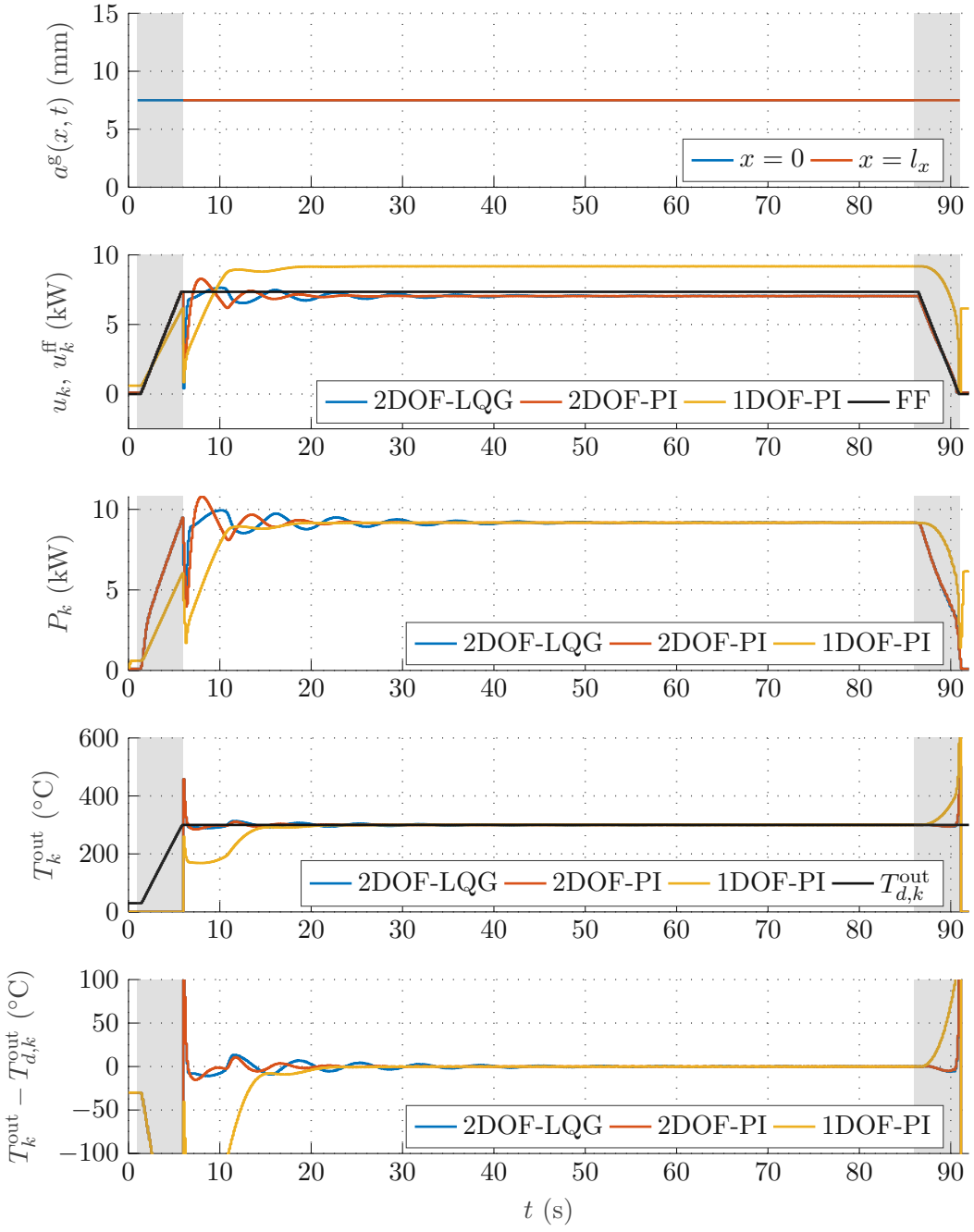

Figure 10.1: Experiment 1: Comparison of a 1DOF PI controller to the proposed 2DOF LQG and a 2DOF PI controller with the parameters from Table 10.1 ($\hat{a}^{\mathrm{g}} = 0$).

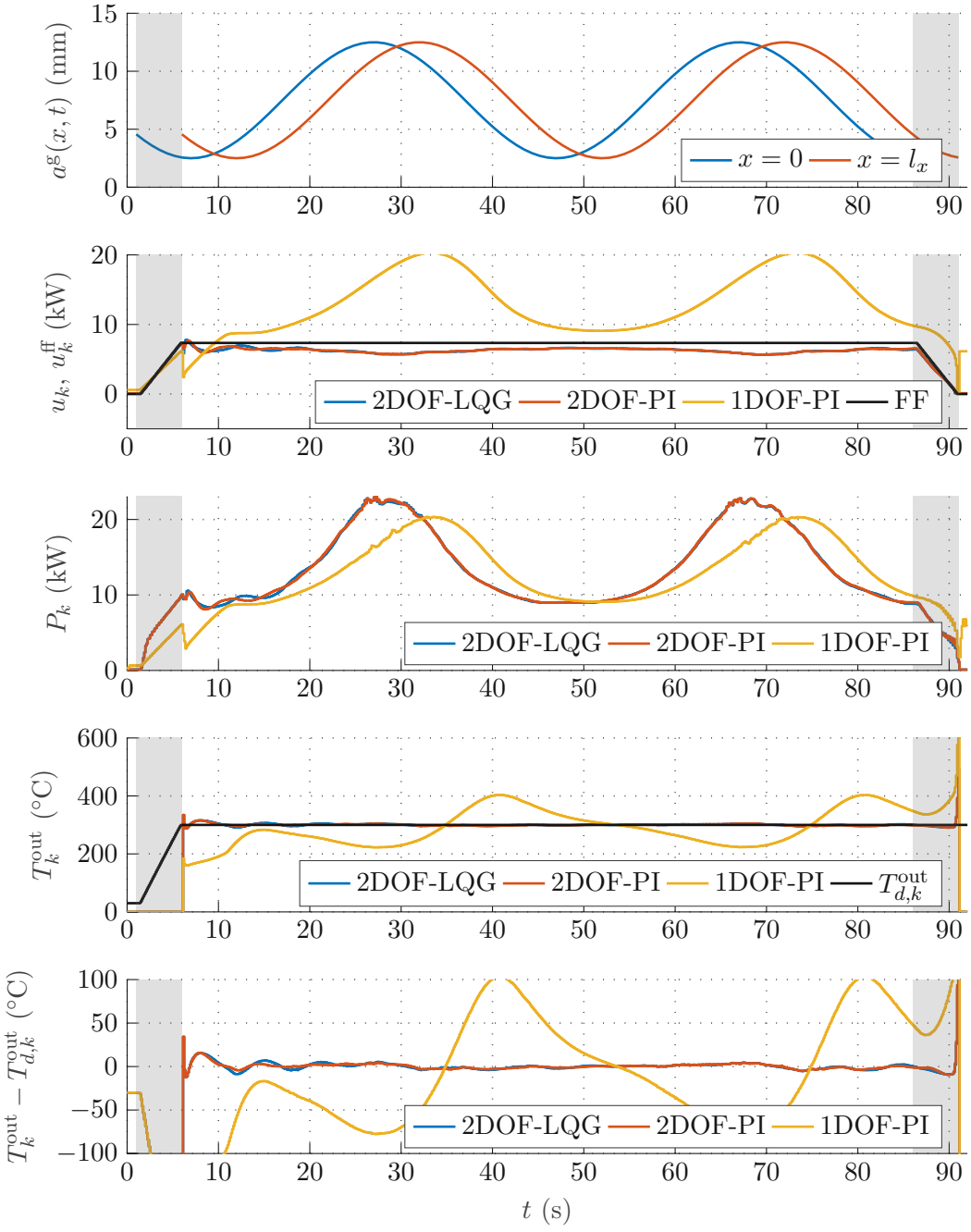

Figure 10.2: Experiment 2: Comparison of a 1DOF PI controller to the proposed 2DOF LQG and a 2DOF PI controller with the parameters from Table 10.1 ($k^{\mathrm{g}} = 2\pi/4\mathrm{m}$).

now oscillates with an amplitude of 20°C for both 2DOF controllers. The 1DOF PI controller yields unacceptable results in this experiment.

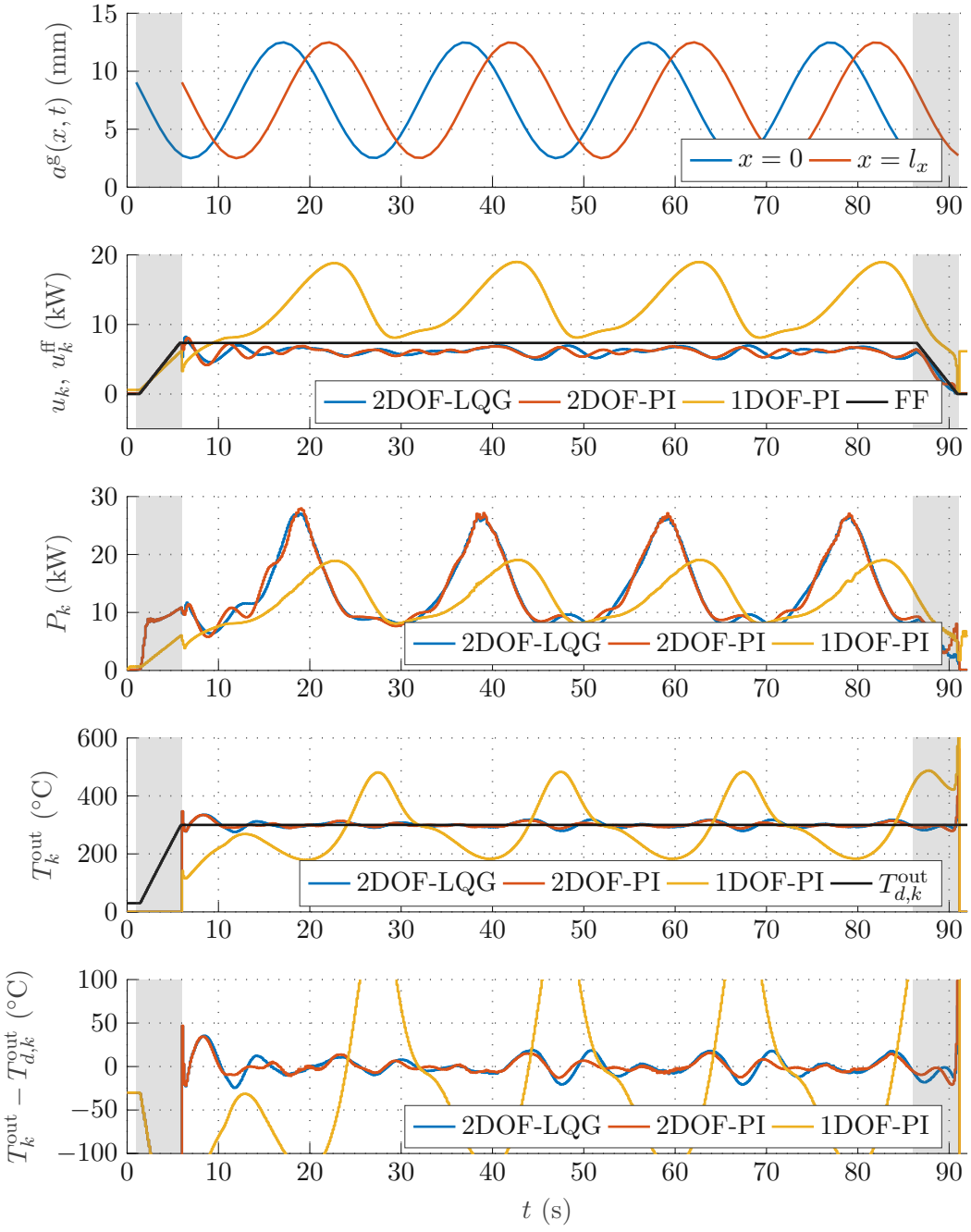

Figure 10.3: Experiment 3: Comparison of a 1DOF PI controller to the proposed 2DOF LQG and a 2DOF PI controller with the parameters from Table 10.1 ($k^{\mathrm{g}} = 2\pi/2\mathrm{m}$).

Experiment 4: Wavelength 1m The results are shown in Fig. 10.4. If the wavelength is further reduced, also the 2DOF controllers reach their performance limits. The assumption of a homogeneous air gap, which was used for the controller design, is no longer valid in this case.

From the simulation results, two conclusions can be drawn regarding the performance limits of the 2DOF controller. First, the inductor needs to be significantly shorter than the wavelength of the sheet (cf. Table 10.1). Secondly, the gap between the inductor and the roller table, which effectively limits $\hat{a}^{\mathrm{g}}$, should be as small as possible. The applicability of the control approach can thus be evaluated based on the geometric parameters of the IH system.

Experiment 5: Wavelength 2m**, output measurement noise** For the final test, experiment 3 was repeated with added measurement noise. The results are shown in Fig. 10.5.

It can be seen that all three controllers are robust to noise in the measured exit temperature T_k^{out}. This is because the integral parts of the feedback controllers filter the high-frequency components of the measurement noise and only the proportional feedback is affected. Due to the integrating behavior of the plant itself, i.e., the sheet, this additional noise from the feedback controller is again averaged. The feedforward branch of the 2DOF controllers is not affected by the output noise. Overall, the measured exit temperature with added noise is still within the required ± 50°C tolerance range.

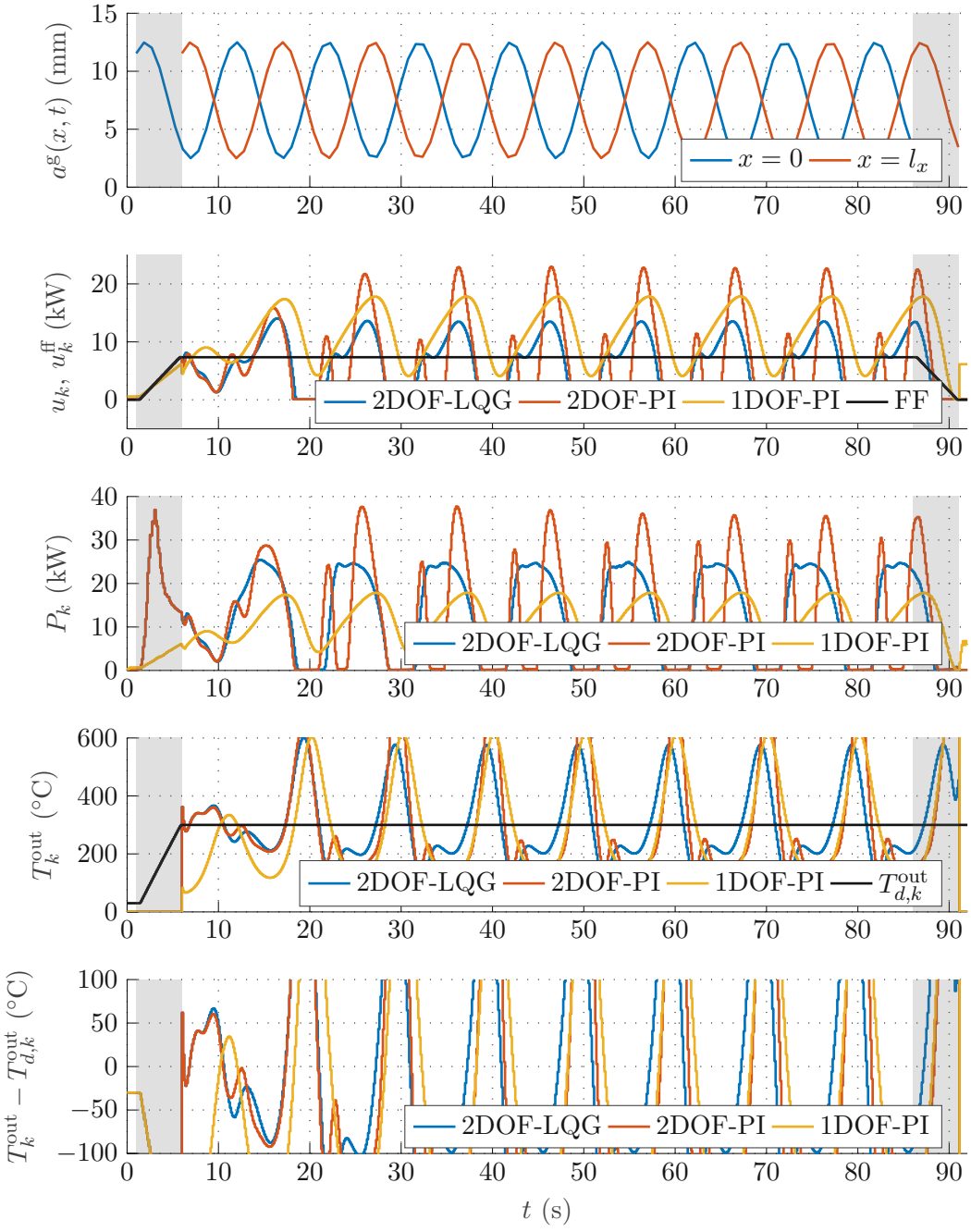

Figure 10.4: Experiment 4: Comparison of a 1DOF PI controller to the proposed 2DOF LQG and a 2DOF PI controller with the parameters from Table 10.1 ($k^{\mathrm{g}} = 2\pi/1\mathrm{m}$).

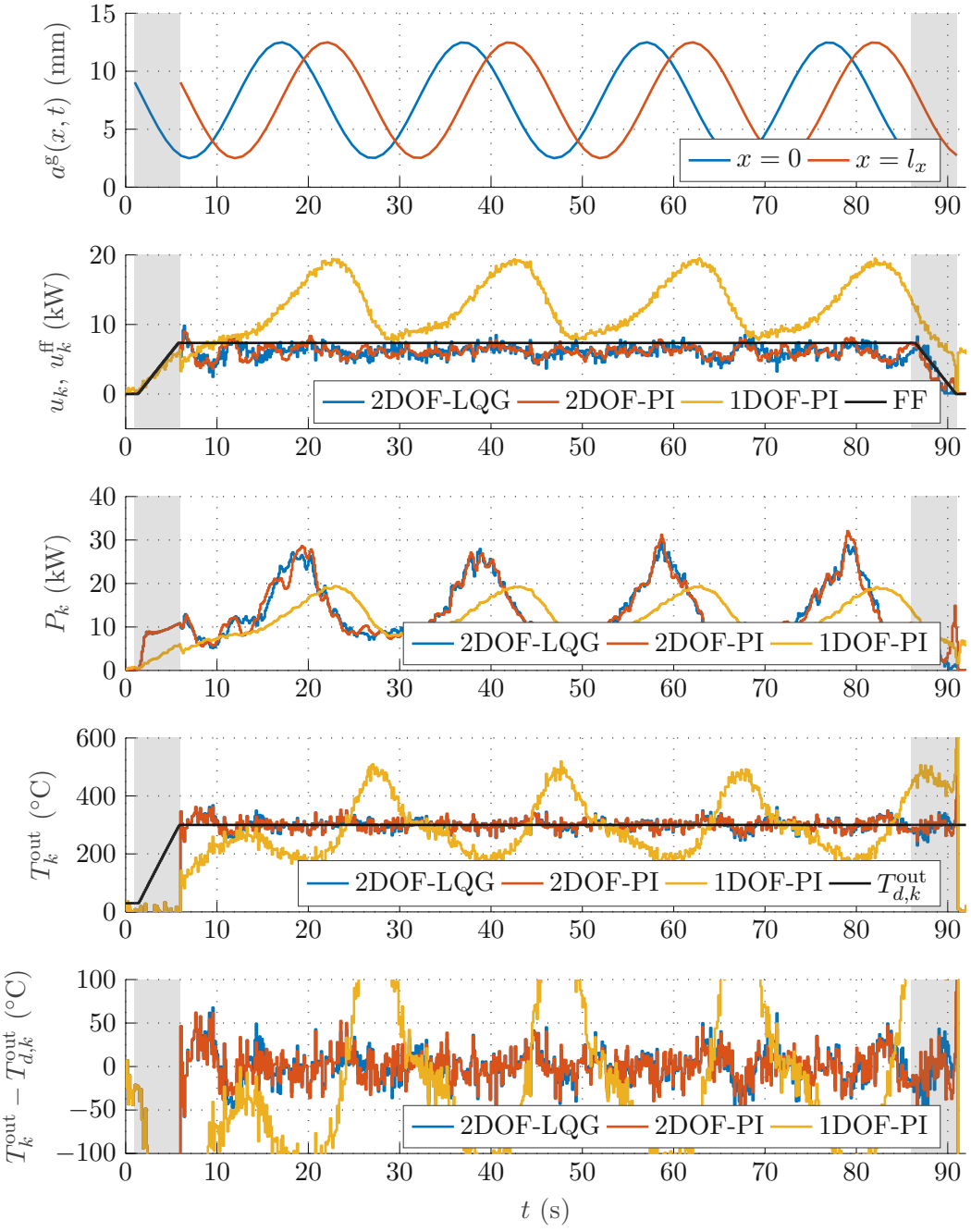

Figure 10.5: Experiment 5: Comparison of a 1DOF PI controller to the proposed 2DOF LQG and a 2DOF PI controller with the parameters from Table 10.1 ($k^{\mathrm{g}} = 2\pi/2\mathrm{m}$, measurement noise).

CHAPTER 11

Conclusions and Outlook

In this second part of the thesis, the process of induction heating of thin molybdenum sheets in translational motion was examined. The goal was to control the exit temperature of the sheet with minimum tolerance, in order to optimize the results of a downstream cutting process. The main challenge in this part was to compensate for the time-varying air gap between the sheet and the induction heater. For this, a real-time capable 2-degrees-of-freedom (2DOF) cascade controller was designed and tested in simulations. The results give qualitative information about the performance of the controller and how to further optimize the process.

11.1 Summary

First, a finite-element process model of the electromagnetic field problem was formulated and solved numerically as a reference. The model was validated experimentally, and the sensitivity of the exit temperature towards the air gap was examined.

The process model was then simplified to a one-dimensional transport system with an uncertain input function. A computationally expensive calculation of the electromagnetic field was avoided by employing an equivalent circuit model and the energy balance. Difficulties arising from nonlinear material parameters were circumvented by using the specific enthalpy as a system state instead of the temperature. The model inputs were changed from current to active power and a cascade control loop for the transmitted heating power was applied. The reduced model was validated by comparison with the process model. By tuning of the unknown disturbance input, the models can be brought to very good agreement.

The reduced model is a linear time-varying advection equation with unknown input disturbances and an uncertain input function. The input function was approximated by a time-invariant profile, and a 2DOF controller was designed for the resulting linear time-invariant system. The feedforward branch of the controller is a flatness-based inversion of the known parts of the reduced system model, while the feedback branch was designed as a linear-quadratic-Gaussian controller and later reduced to a proportional-integral controller. Finally, since the reduced model only describes a state of operation where the sheet covers the entire field domain, some additions were made to deal with the remaining cases.

The designed controller was tested in a representative test scenario, which is focused on evaluation of the design assumptions of the controller. The numerical results show that the controller is able to compensate for air gap fluctuations, depending on the spatial homogeneity of the air gap.

11.2 Conclusions

In conclusion, the designed control concept can be applied to a number of similar systems due to the generality of the reduced model. The application of an equivalent circuit model for the electromagnetic subsystem and a generic input function for the thermal subsystem allows for a transition from a multiphysics problem to the well-understood transport equation. Similar transitions are possible for any physical domains, as long as a conservation law – like in this case, the energy balance – is available.

For uncertain air gap geometries, it was found that the heating problem reduces to an identification problem for the unknown input function. To solve the identification problem, it is desirable to either employ additional sensors, or to reduce the length of the inductor as far as possible.

11.3 Outlook

From the results at hand, further steps can be taken to investigate and mitigate the effect of fluctuating air gaps. If, for a given inductor, the air gap fluctuations have shorter wavelengths, it is worthwhile to examine the form of the air gap and take it into account in the feedforward controller. This would lead to an identification problem and requires additional sensors, either for temperatures along the field domain or for the air gap width in the field domain.

Alternatively, the inductor design could be revisited. Since the ratio between the inductor length and the dominant wavelength of the sheet decides the quality of the heating process, it may be enough to design shorter inductor coils. Shortening of the inductor can, in turn, result in a large temperature gradient over a shorter distance. To mitigate this effect, the relative motion between the sheet and the

inductor can be altered and optimized. This idea is pursued in the related work [50] and follow-up publications for radiative heating.

Finally, the modeling and design concepts can be generalized to higher spatial dimensions. In this case, the inductor and pyrometers would move along the surface of a 2D or 3D object and simultaneously observe and control the temperature profile. Challenges include the estimation of a higher-dimensional input function and optimal path planning for sensors and actuators.

Appendices

APPENDIX A

Finite Volume Method

To illustrate the transition from (3.19) to (3.20), the finite volume (FV) method is applied in the following. Let the state vector $\boldsymbol{T}$ in (3.20) be the vector of mean temperatures in each subdivision $\Omega^w_{i,j}$ of the wall and Ω^p_i of the plate, i.e.,

$$\boldsymbol{T} = \left[\begin{array}{cccc|ccc} \overline{T}^w_{1,1} & \overline{T}^w_{1,2} & \dots & \overline{T}^w_{N^w,N^w_{N^w}} & \overline{T}^p_1 & \dots & \overline{T}^p_{N^p} \end{array} \right]^{\mathrm{T}}. \tag{A.1}$$

A.1 Left-Hand Side

The FV discretization of (3.19) is done by approximation of the integral over the respective domains $\Omega^w_{i,j}$ and Ω^p_i. Integration of the left-hand sides of (3.19a) and (3.19g) yields

$$\int_{\Omega^w_{i,j}} \rho^w_{i,j} c^w_{p,i,j}(T) \partial_t T \,\mathrm{d}\boldsymbol{x} \approx \int_{\Omega^w_{i,j}} \rho^w_{i,j} c^w_{p,i,j}(\overline{T}^w_{i,j}) \,\mathrm{d}\boldsymbol{x} \frac{\mathrm{d}}{\mathrm{d}t} \overline{T}^w_{i,j} = C^w_{i,j}(\overline{T}^w_{i,j}) \frac{\mathrm{d}}{\mathrm{d}t} \overline{T}^w_{i,j} \tag{A.2a}$$

$$\int_{\Omega^p_i} \rho^p c^p_p(T) \partial_t T \,\mathrm{d}\boldsymbol{x} \approx \int_{\Omega^p_i} \rho^p c^p_p(\overline{T}^p_i) \,\mathrm{d}\boldsymbol{x} \frac{\mathrm{d}}{\mathrm{d}t} \overline{T}^p_i = C^p_i(\overline{T}^p_i) \frac{\mathrm{d}}{\mathrm{d}t} \overline{T}^p_i. \tag{A.2b}$$

The resulting heat capacities $C^w_{i,j}$ and C^p_i are used in the mass matrix $\boldsymbol{M}(\boldsymbol{T})$ of (3.20)

$$\boldsymbol{M}(\boldsymbol{T}) = \left[\begin{array}{ccc|ccc} C^w_{1,1} & 0 & \dots & & & \\ 0 & C^w_{1,2} & \dots & & \boldsymbol{0} & \\ \vdots & \vdots & \ddots & & & \\ \hline & & & C^p_1 & 0 & \dots \\ & \boldsymbol{0} & & 0 & C^p_2 & \dots \\ & & & \vdots & \vdots & \ddots \end{array} \right]. \tag{A.3}$$

A.2 Right-Hand Side

Integration of the right-hand sides of (3.19a) and (3.19g) and application of the divergence theorem leads to

$$\int_{\Omega^w_{i,j}} \boldsymbol{\nabla} \cdot \left(\eta \lambda^w_{i,j}(T) \boldsymbol{\nabla} T\right) \mathrm{d}\boldsymbol{x} = \int_{\partial\Omega^w_{i,j}} \eta \lambda^w_{i,j}(T) \partial_n T \, \mathrm{d}\boldsymbol{x} = \sum_k \dot{Q}^w_{i,j,k} + \dot{Q}^{w,\mathrm{in}}_{i,j} + \dot{Q}^{w,\mathrm{out}}_{i,j} \tag{A.4}$$

and

$$\int_{\Omega^p_i} \boldsymbol{\nabla} \cdot (\lambda^p(T) \boldsymbol{\nabla} T) \, \mathrm{d}\boldsymbol{x} = \int_{\partial\Omega^p_i} \lambda^p(T) \partial_n T \, \mathrm{d}\boldsymbol{x} \quad = \sum_j \dot{Q}^p_{i,j} + \dot{Q}^{p,\mathrm{rad}}_i. \tag{A.5}$$

The flux terms $\dot{Q}^w_{i,j,k}$, $\dot{Q}^{w,\mathrm{in}}_{i,j}$, $\dot{Q}^{w,\mathrm{out}}_{i,j}$, $\dot{Q}^p_{i,j}$, and $\dot{Q}^{p,\mathrm{rad}}_i$ incorporate the boundary conditions of (3.19). These flux terms are derived by integrating the boundary conditions of (3.19) together with (3.9) and (3.12) over the respective boundary surfaces.

A.2.1 Heat Conduction in Solids

The conductive heat transfer $\dot{Q}^w_{i,j,k}$ between the wall elements $\Omega^w_{i,j}$ and $\Omega^w_{i,k}$ is approximated by

$$\dot{Q}^w_{i,j,k} \approx G^w_{i,j,k}\left(\overline{T}^w_{i,k} - \overline{T}^w_{i,j}\right), \quad G^w_{i,j,k} = \eta \lambda^w_{i,j,k} \frac{A^w_{i,j,k}}{l^w_{i,j,k}}. \tag{A.6}$$

The interface area $A^w_{i,j,k}$ between the wall elements is defined as

$$A^w_{i,j,k} = \int_{\partial\Omega^w_{i,j} \cap \partial\Omega^w_{i,k}} \mathrm{d}\boldsymbol{s} \tag{A.7}$$

and the distance $l^w_{i,j,k}$ connects the centers of mass

$$l^w_{i,j,k} = \left\| \frac{\int_{\Omega^w_{i,k}} \boldsymbol{x} \, \mathrm{d}\boldsymbol{x}}{\int_{\Omega^w_{i,k}} \mathrm{d}\boldsymbol{x}} - \frac{\int_{\Omega^w_{i,j}} \boldsymbol{x} \, \mathrm{d}\boldsymbol{x}}{\int_{\Omega^w_{i,j}} \mathrm{d}\boldsymbol{x}} \right\|. \tag{A.8}$$

The thermal conductivity $\lambda^w_{i,j,k}$ is composed from

$$\lambda^w_{i,j,k} = \frac{1}{\delta_{i,j,k}/\lambda^w_{i,j} + (1-\delta_{i,j,k})/\lambda^w_{i,k}}, \quad 0 \le \delta_{i,j,k} \le 1. \tag{A.9}$$

The parameter $\delta_{i,j,k}$ is chosen based on the portion of $l^w_{i,j,k}$ that is covered by either of the domains $\Omega^w_{i,j}$ and $\Omega^w_{i,k}$.

The heat conduction between the plate elements Ω_i^p is derived in a similar way, resulting in

$$\dot{Q}_{i,j}^p \approx G_{i,j}^p \left(\overline{T}_j^p - \overline{T}_i^p\right) \tag{A.10a}$$

$$G_{i,j}^p = \lambda^p \frac{A_{i,j}^p}{l_{i,j}^p} \tag{A.10b}$$

$$A_{i,j}^p = \int_{\partial\Omega_i^p \cap \partial\Omega_k^p} \mathrm{d}\boldsymbol{x} \tag{A.10c}$$

$$l_{i,j}^p = \left\| \frac{\int_{\Omega_i^p} \boldsymbol{x}\,\mathrm{d}\boldsymbol{x}}{\int_{\Omega_i^p} \mathrm{d}\boldsymbol{x}} - \frac{\int_{\Omega_j^p} \boldsymbol{x}\,\mathrm{d}\boldsymbol{x}}{\int_{\Omega_j^p} \mathrm{d}\boldsymbol{x}} \right\|. \tag{A.10d}$$

A.2.2 Outer Boundary

The heat flux on the outer boundary of the furnace wall depends on the ambient temperature T^∞ and the respective boundary temperatures $T_{i,j}^{w,\mathrm{out}}$. Integration of (3.12) yields

$$\begin{aligned}\dot{Q}_{i,j}^{w,\mathrm{out}} &= \int_{\partial\Omega_{i,j}^w \cap \Gamma^{\mathrm{out}}} \alpha^{\mathrm{out}}(T^\infty - T) + \sigma\varepsilon^{\mathrm{out}}\left((T^\infty)^4 - T^4\right) \mathrm{d}\boldsymbol{x} \approx \\ &\approx A_{i,j}^{w,\mathrm{out}}\left(\alpha^{\mathrm{out}}(T^\infty - T_{i,j}^{w,\mathrm{out}}) + \sigma\varepsilon^{\mathrm{out}}\left((T^\infty)^4 - (T_{i,j}^{w,\mathrm{out}})^4\right)\right),\end{aligned} \tag{A.11}$$

where

$$A_{i,j}^{w,\mathrm{out}} = \int_{\partial\Omega_{i,j}^w \cap \Gamma^{\mathrm{out}}} \mathrm{d}\boldsymbol{x}. \tag{A.12}$$

Using the distance

$$l_{i,j}^{w,\mathrm{out}} = \begin{cases} \left\| \dfrac{\int_{\Omega_{i,j}^w \cap \Gamma^{\mathrm{out}}} \boldsymbol{x}\,\mathrm{d}\boldsymbol{x}}{\int_{\Omega_{i,j}^w \cap \Gamma^{\mathrm{out}}} \mathrm{d}\boldsymbol{x}} - \dfrac{\int_{\Omega_{i,j}^w} \boldsymbol{x}\,\mathrm{d}\boldsymbol{x}}{\int_{\Omega_{i,j}^w} \mathrm{d}\boldsymbol{x}} \right\|, & \text{if } \Omega_{i,j}^w \cap \Gamma^{\mathrm{out}} \neq \emptyset \\ 0, & \text{otherwise} \end{cases} \tag{A.13}$$

from the center of mass of the element $\Omega_{i,j}^w$ to the outer boundary, the surface temperatures $T_{i,j}^{w,\mathrm{out}}$ can, in the simplest case, be determined by extrapolation in the form

$$T_{i,j}^{w,\mathrm{out}} = \left\{ \begin{array}{ll} \overline{T}_{i,j}^w + l_{i,j}^{w,\mathrm{out}} \dfrac{\overline{T}_{i,j}^w - \overline{T}_{i,j-1}^w}{l_{i,j,j-1}^w}, & \text{if } j > 1 \\ \overline{T}_{i,1}^w + l_{i,1}^{w,\mathrm{out}} \dfrac{\overline{T}_{i,2}^w - \overline{T}_{i,1}^w}{l_{i,2,1}^w}, & \text{if } j = 1 \end{array} \right\} = (\boldsymbol{s}_{i,j}^{w,\mathrm{out}})^{\mathrm{T}} \boldsymbol{T} \tag{A.14}$$

with the extrapolation operator $(\boldsymbol{s}_{i,j}^w)^{\mathrm{T}}$.

For a more compact notation, the convective and radiative parts of (A.11) are split up into

$$\begin{bmatrix} G^{w,\mathrm{out}}_{i,j,1} & G^{w,\mathrm{out}}_{i,j,2} & \dots \end{bmatrix} = G^{w,\mathrm{out}}_{i,j} (\boldsymbol{s}^w_{i,j})^{\mathrm{T}}, \qquad G^{w,\mathrm{out}}_{i,j} = A^{w,\mathrm{out}}_{i,j} \alpha^{\mathrm{out}} \tag{A.15a}$$

$$R^{w,\mathrm{out}}_{i,j}(\boldsymbol{T}) = E^{w,\mathrm{out}}_{i,j} \left((\boldsymbol{s}^w_{i,j})^{\mathrm{T}} \boldsymbol{T} \right)^4, \quad E^{w,\mathrm{out}}_{i,j} = A^{w,\mathrm{out}}_{i,j} \sigma \varepsilon^{\mathrm{out}}, \tag{A.15b}$$

such that

$$\begin{aligned} \dot{Q}^{w,\mathrm{out}}_{i,j} &\approx G^{w,\mathrm{out}}_{i,j} \left(T^\infty - (\boldsymbol{s}^w_{i,j})^{\mathrm{T}} \boldsymbol{T} \right) + E^{w,\mathrm{out}}_{i,j} \left((T^\infty)^4 - \left((\boldsymbol{s}^w_{i,j})^{\mathrm{T}} \boldsymbol{T} \right)^4 \right) \\ &= - \begin{bmatrix} G^{w,\mathrm{out}}_{i,j,1} & \dots \end{bmatrix} \boldsymbol{T} - R^{w,\mathrm{out}}_{i,j}(\boldsymbol{T}) + G^{w,\mathrm{out}}_{i,j} T^\infty + E^{w,\mathrm{out}}_{i,j} (T^\infty)^4. \end{aligned} \tag{A.16}$$

A.2.3 Radiation Enclosure

On the interior furnace walls, let

$$A^{w,\mathrm{in}}_{i,j} = \int_{\partial \Omega^w_{i,j} \cap \Gamma^{\mathrm{in}}} \mathrm{d}\boldsymbol{x} \tag{A.17}$$

and

$$l^{w,\mathrm{in}}_{i,j} = \begin{cases} \left\| \frac{\int_{\Omega^w_{i,j} \cap \Gamma^{\mathrm{in}}} \boldsymbol{x} \, \mathrm{d}\boldsymbol{x}}{\int_{\Omega^w_{i,j} \cap \Gamma^{\mathrm{in}}} \mathrm{d}\boldsymbol{x}} - \frac{\int_{\Omega^w_{i,j}} \boldsymbol{x} \, \mathrm{d}\boldsymbol{x}}{\int_{\Omega^w_{i,j}} \mathrm{d}\boldsymbol{x}} \right\|, & \text{if } \Omega^w_{i,j} \cap \Gamma^{\mathrm{in}} \neq \emptyset \\ 0, & \text{otherwise.} \end{cases} \tag{A.18}$$

The interior wall surface temperatures are

$$T^{w,\mathrm{in}}_{i,j} = \left\{ \begin{array}{ll} \overline{T}^w_{i,j} + l^{w,\mathrm{in}}_{i,j} \dfrac{\overline{T}^w_{i,j} - \overline{T}^w_{i,j+1}}{l^w_{i,j,j+1}}, & \text{if } j < N^w_i \\ \overline{T}^w_{i,N^w_i} + l^{w,\mathrm{in}}_{i,N^w_i} \dfrac{\overline{T}^w_{i,N^w_i - 1} - \overline{T}^w_{i,N^w_i}}{l^w_{i,N^w_i,N^w_i-1}}, & \text{if } j = N^w_i \end{array} \right\} = (\boldsymbol{s}^{w,\mathrm{in}}_{i,j})^{\mathrm{T}} \boldsymbol{T} \tag{A.19}$$

with the extrapolation operator $(\boldsymbol{s}^{w,\mathrm{in}}_{i,j})^{\mathrm{T}}$ and the plate surface temperatures are computed in a similar way, using $T^{p,\mathrm{in}}_i = (\boldsymbol{s}^p_i)^{\mathrm{T}} \boldsymbol{T}$, with the three-dimensional extrapolation operator $(\boldsymbol{s}^p_i)^{\mathrm{T}}$.

From (3.9) it follows that

$$\dot{Q}^{w,\mathrm{in}}_{i,j} = \int_{\partial \Omega^w_{i,j} \cap \Gamma^{\mathrm{in}}} \dot{q}^w(T, \boldsymbol{x}, \boldsymbol{u}) \, \mathrm{d}\boldsymbol{x} \approx R^{w,\mathrm{in}}_{i,j}(\boldsymbol{T}) + (\boldsymbol{b}^w_{i,j})^{\mathrm{T}} \boldsymbol{u}, \tag{A.20}$$

with

$$\begin{aligned} R^{w,\mathrm{in}}_{i,j}(\boldsymbol{T}) = -A^{w,\mathrm{in}}_{i,j} \sigma \varepsilon^w (T^{w,\mathrm{in}}_{i,j})^4 + \sum_{k,l} \int_{\partial \Omega^w_{i,j} \cap \Gamma^{\mathrm{in}}} \int_{\partial \Omega^w_{k,l} \cap \Gamma^{\mathrm{in}}} \sigma \varepsilon^w K(\boldsymbol{x}, \boldsymbol{x}') \, \mathrm{d}\boldsymbol{x}' \, \mathrm{d}\boldsymbol{x} T^{w,\mathrm{in}}_{k,l} + \\ + \sum_k \int_{\partial \Omega^w_{i,j} \cap \Gamma^{\mathrm{in}}} \int_{\partial \Omega^p_k \cap \partial \Omega^p} \sigma \varepsilon^p K(\boldsymbol{x}, \boldsymbol{x}') \, \mathrm{d}\boldsymbol{x}' \, \mathrm{d}\boldsymbol{x} T^{p,\mathrm{in}}_k \end{aligned} \tag{A.21}$$

and

$$\boldsymbol{b}_{i,j}^{w} = \begin{bmatrix} \frac{1}{A_1^h} \int_{\partial\Omega_{i,j}^w \cap \Gamma^{\text{in}}} \int_{\Gamma_1^h} K(\boldsymbol{x}, \boldsymbol{x}') \, \mathrm{d}\boldsymbol{x}' \, \mathrm{d}\boldsymbol{x} \\ \vdots \end{bmatrix}. \tag{A.22}$$

Similarly, for the plate radiation exchange, it holds

$$\dot{Q}_i^{p,\text{rad}} = \int_{\partial\Omega_i^p \cap \partial\Omega^p} \dot{q}^p(T, \boldsymbol{x}, \boldsymbol{u}) \, \mathrm{d}\boldsymbol{x} \approx R_i^p(\boldsymbol{T}) + (\boldsymbol{b}_i^p)^{\mathrm{T}} \boldsymbol{u}. \tag{A.23}$$

The double integrals of $K(\boldsymbol{x}, \boldsymbol{x}')$ are approximated by exchange factor calculations, usually based on Hemicube or Monte Carlo methods.

A.3 System Matrices

From (A.6), (A.10a) and (A.16), the matrices $\boldsymbol{A}(\boldsymbol{T})$ and $\boldsymbol{B}^d$ in (3.20) follow as

$$\boldsymbol{A}(\boldsymbol{T}) = \underbrace{-\left[\begin{array}{ccc|ccc} \sum_k G_{1,1,k}^w & -G_{1,1,2}^w & \cdots & & \\ -G_{1,2,1}^w & \sum_k G_{1,2,k}^w & \cdots & \multicolumn{3}{c}{\mathbf{0}} \\ \vdots & \vdots & \ddots & & \\ \hline & & & -\sum_j G_{1,j}^p & G_{1,2}^p & \cdots \\ \multicolumn{3}{c|}{\mathbf{0}} & G_{2,1}^p & -\sum_j G_{2,j}^p & \cdots \\ & & & \vdots & \vdots & \ddots \end{array}\right]}_{\boldsymbol{A}_0(\boldsymbol{T})} \underbrace{-\left[\begin{array}{ccc|c} G_{1,1,1}^{w,\text{out}} & G_{1,1,2}^{w,\text{out}} & \cdots & \\ G_{1,2,1}^{w,\text{out}} & G_{1,2,2}^{w,\text{out}} & \cdots & \mathbf{0} \\ \vdots & \vdots & \ddots & \\ \hline \multicolumn{3}{c|}{\mathbf{0}} & \mathbf{0} \end{array}\right]}_{=\boldsymbol{A}_1(\boldsymbol{T})} \tag{A.24}$$

and

$$\boldsymbol{B}^d = \left[\begin{array}{cc} G_{1,1}^{w,\text{out}} & E_{1,1}^{w,\text{out}} \\ \vdots & \vdots \\ \hline \multicolumn{2}{c}{\mathbf{0}} \end{array}\right]. \tag{A.25}$$

Furthermore, with the definitions in (A.20) and (A.23), the remaining terms of (3.20) become

$$\boldsymbol{R}(\boldsymbol{T}) = \left[\begin{array}{c} R_{1,1}^{w,\text{in}}(\boldsymbol{T}) - R_{1,1}^{w,\text{out}}(\boldsymbol{T}) \\ \vdots \\ \hline R_1^p(\boldsymbol{T}) \\ \vdots \end{array}\right] \tag{A.26}$$

and

$$\boldsymbol{B} = \left[\begin{array}{c} (\boldsymbol{b}_{1,1}^{w})^{\mathrm{T}} \\ \vdots \\ \hline (\boldsymbol{b}_{1}^{p})^{\mathrm{T}} \\ \vdots \end{array}\right]. \tag{A.27}$$

A.4 ODE System Analysis

The resulting ODE system takes the form

$$\boldsymbol{M}(\boldsymbol{T})\frac{\mathrm{d}}{\mathrm{d}t}\boldsymbol{T} = \boldsymbol{A}(\boldsymbol{T})\boldsymbol{T} + \boldsymbol{R}(\boldsymbol{T}) + \boldsymbol{B}\boldsymbol{u} + \boldsymbol{B}^{d}\boldsymbol{d}. \tag{A.28}$$

If the furnace is not charged, the plate domain is $\Omega^p = \emptyset$ and the terms $G_{i,j}^p$, R_i^p as well as any integral over Ω^p become zero. Hence, (3.20) includes the empty and the charged furnace model.

The system matrices $\boldsymbol{M}(\boldsymbol{T})$ and $\boldsymbol{A}(\boldsymbol{T})$ defined in (A.3) and (A.24), respectively, and the radiation nonlinearity $\boldsymbol{R}(\boldsymbol{T})$ defined in (A.26) exhibit useful properties for qualitative analysis. Some examples are given in the following:

- The mass matrix $\boldsymbol{M}(\boldsymbol{T})$ is symmetric and positive definite.
- The matrix $\boldsymbol{A}(\boldsymbol{T})$, according to (A.24), is the negative sum of a symmetric, weakly diagonally dominant matrix $\boldsymbol{A}_0$ and a weakly diagonally dominant matrix $\boldsymbol{A}_1$. The diagonal elements of both $\boldsymbol{A}_0$ and $\boldsymbol{A}_1$ are non-negative. The matrix $\boldsymbol{A}_0$ describes the in-domain heat conduction and the matrix $\boldsymbol{A}_1$ describes the losses due to convection on the outer system boundary.

  If the state vector $\boldsymbol{T}$ is ordered as shown in (A.1), $\boldsymbol{A}_0$ has the form of a block diagonal matrix. Each diagonal block of $\boldsymbol{A}_0$ represents one solid, i.e., Ω_i^w or Ω^p, that is isolated from the others in terms of conduction and convection. The diagonal blocks are weakly diagonally dominant and describe strongly connected graphs (see, e.g., [25, "property SC"]). The diagonal elements are non-negative. Therefore, $\boldsymbol{A}_0$ is positive semidefinite.

  The matrix $\boldsymbol{A}_1$ has the same block-diagonal structure as $\boldsymbol{A}_0$. For each diagonal block of $\boldsymbol{A}_0$, the matrix $\boldsymbol{A}_1$ can have one or more rows that are stricly diagonally dominant. If this is the case, then the respective diagonal block in $\boldsymbol{A}(\boldsymbol{T})$ is a so-called weakly chained diagonally dominant matrix and therefore non-singular, see, e.g., [4, 64].

  The structure of $\boldsymbol{A}_0$ and $\boldsymbol{A}_1$ ensures

  $$\mathbf{1}^{\mathrm{T}}\boldsymbol{A}(\boldsymbol{T})\boldsymbol{T} = -\mathbf{1}^{\mathrm{T}}\boldsymbol{A}_1(\boldsymbol{T})\boldsymbol{T} \leq 0.$$

  That is, each solid on its own can only store or leak heat.

- The function $\boldsymbol{R}(\boldsymbol{T})$ represents the radiation exchange in the furnace chamber and the radiation losses on the outer boundary. It exhibits a polynomial nonlinearity of order 4 due to the appearance of T^4 in (3.9) and (3.12). Due to energy conservation, it holds that $\mathbf{1}^{\mathrm{T}}\boldsymbol{R}(\boldsymbol{T}) \leq 0$. Moreover, structural properties similar to $\boldsymbol{A}(\boldsymbol{T})$ were proven in [58].

- The evolution of the total heat or enthalpy H in the system is described by

$$\frac{\mathrm{d}}{\mathrm{d}t}H = \mathbf{1}^{\mathrm{T}}\boldsymbol{M}(\boldsymbol{T})\frac{\mathrm{d}}{\mathrm{d}t}\boldsymbol{T} = \underbrace{\mathbf{1}^{\mathrm{T}}\boldsymbol{A}(\boldsymbol{T})\boldsymbol{T} + \mathbf{1}^{\mathrm{T}}\boldsymbol{R}(\boldsymbol{T})}_{\leq 0} + \mathbf{1}^{\mathrm{T}}\boldsymbol{B}\boldsymbol{u} + \mathbf{1}^{\mathrm{T}}\boldsymbol{B}^{d}\boldsymbol{d},$$

  where $\mathbf{1}^{\mathrm{T}}\boldsymbol{B}\boldsymbol{u} + \mathbf{1}^{\mathrm{T}}\boldsymbol{B}^{d}\boldsymbol{d} \geq 0$ because the heating powers $\boldsymbol{u}$ and the ambient temperatures $\boldsymbol{d}$ (in K) have to be non-negative. It can be expected that, similar to the findings in [58], the discretized system (A.28) is asymptotically stable. For the practical implementation, this implies that instabilities in the solution can only be caused by numerical effects.

APPENDIX B

Cascade Power Controller for Induction Heating

The virtual system input $u(t)$ defined in (8.41) describes the power that dissipates in the plate and the magnetic concentrators. For precise control of $u(t)$, a cascade control concept is required and will be derived in the following. To this end, consider

$$u(t) = P(t) - R^c|I(t)|^2 = P^p(t) + P^{\mathrm{Fe}}(t) \tag{B.1}$$

and, since $I(t)$ is real and non-negative,

$$|I(t)|^2 = I^2(t), \tag{B.2}$$

with the RMS input current $I(t)$ to the inductor, the RMS heating power P^p transmitted to the plate, and the RMS power P^{Fe} dissipated in the magnetic cores. The power P results from

$$P(t) = U^{\mathrm{s}}(t)I^{\mathrm{s}}(t)\cos(\phi^{\mathrm{s}}(t)). \tag{B.3}$$

The RMS source voltage U^{s} can be controlled externally, while the RMS source current I^{s}, the phase angle ϕ^{s}, I, and P depend on U^{s}.

Note that the time dependence of all signals in this appendix is understood on a time scale that is significantly slower than the electromagnetic system and significantly faster than the 2-degrees-of-freedom temperature control system.

B.1 Estimation of R^c during Idle Operation

If no sheet is present in the field domain, i.e., $P^p = 0$, assume

$$u(t) = P^{\mathrm{Fe}}(t) \tag{B.4a}$$
$$P^{\mathrm{Fe}}(t) \ll R^c I^2(t) \tag{B.4b}$$
$$P(t) = P^{\mathrm{Fe}}(t) + R^c I^2(t) \approx R^c I^2(t). \tag{B.4c}$$

This implies that only the inductor coil is heated, which is not desirable. However, the control law (B.1) requires knowledge of the resistance R^c. The idle times (when no sheet is present) can be used to determine the value of R^c.

The RMS values $U^{\mathrm{s}}(t)$, $I^{\mathrm{s}}(t)$, and $I(t)$ are measured and also the power factor $\cos(\phi^{\mathrm{s}}(t))$ of the power supply is known. The supplied active power $P(t)$ and the total resistance $R(t)$ of the inductor system read as

$$P(t) = U^{\mathrm{s}}(t) I^{\mathrm{s}}(t) \cos(\phi^{\mathrm{s}}(t)) \tag{B.5a}$$
$$R(t) = P(t)/I^2(t) = U^{\mathrm{s}}(t) I^{\mathrm{s}}(t) \cos(\phi^{\mathrm{s}}(t))/I^2(t). \tag{B.5b}$$

From (B.4), it follows that

$$R^c \approx R(t), \tag{B.6}$$

if no sheet is present. Therefore, in idle operation, R^c can be estimated by a recursive least-squares method in the form

$$\mu_k = \frac{\mu_{k-1}}{q + \mu_{k-1}}, \qquad 0 \ll q < 1 \ll \mu_{-1} \tag{B.7a}$$
$$\hat{R}^c_k = (1 - \mu_k)\hat{R}^c_{k-1} + \mu_k R(k\Delta t), \quad \hat{R}^c_{-1} = 0, \tag{B.7b}$$

and, while a sheet is present, the values $\mu_k = \mu_{k-1}$ and $\hat{R}^c_k = \hat{R}^c_{k-1}$ are held constant.

Remark 5. The exact value of R^c varies with the active cross-section of the coil, which can change due to proximity effects. This effect is expected to be minor and is not considered in the estimation.

B.2 Heating Power Controller

A controller for $u(t)$ is designed in the following. Consider the error

$$\begin{aligned} x(t) &= u(t) - u_d \\ &= P(t) - R^c I^2(t) - u_d \\ &= (R(t) - R^c) I^2(t) - u_d. \end{aligned} \tag{B.8}$$

The dynamics of $x(t)$ reads as

$$\begin{aligned}\frac{\mathrm{d}}{\mathrm{d}t}x(t) &= \frac{\mathrm{d}}{\mathrm{d}t}u(t)\\ &= \frac{\mathrm{d}}{\mathrm{d}t}R(t)I^2(t) + (R(t)-R^c)2I(t)\frac{\mathrm{d}}{\mathrm{d}t}I(t).\end{aligned} \tag{B.9}$$

Assuming that $I(t)$ directly serves as (sufficiently smooth) control input, a control law of the form

$$\begin{aligned}\frac{\mathrm{d}}{\mathrm{d}t}I(t) &= \frac{1}{2I(t)(R(t)-R^c)}\left(-\frac{\mathrm{d}}{\mathrm{d}t}R(t)I^2(t) - \frac{1}{\gamma}x(t)\right)\\ &= \frac{1}{2I(t)(R(t)-R^c)}\left(-\frac{\mathrm{d}}{\mathrm{d}t}R(t)I^2(t) - \frac{1}{\gamma}\Big((R(t)-R^c)I^2(t) - u_d\Big)\right)\end{aligned} \tag{B.10}$$

can be chosen to stabilize $x(t)$. The design parameter $\gamma > 0$ is the desired time constant for the decay of $x(t)$. The time evolutions of $I(t)$, $R(t)$, $P(t)$ and u_d are accessible by measurement and calculation. The expression $\frac{\mathrm{d}R}{\mathrm{d}t}$ can be obtained by approximate differentiation. The value of R^c is approximated by $\hat{R}^c_k$, according to (B.7).

The denominator in (B.10) is strictly positive, as long as there is a sheet present in the field domain, i.e., $R(t) > R^c$. To prevent a division by zero in the case that the estimate $\hat{R}^c_k$ of R^c is too large, the denominator can be approximated by $\max\{U_{\min}, 2I(t)(R(t)-\hat{R}^c_k)\}$ with an appropriate value for $U_{\min}$.

The exponential stability of $x(t)$ can be shown by the Lyapunov function

$$V(t) = \frac{1}{2}x^2(t) \tag{B.11}$$

and its time derivative

$$\frac{\mathrm{d}}{\mathrm{d}t}V(t) = -\frac{1}{\gamma}x^2(t) = -\frac{2}{\gamma}V(t). \tag{B.12}$$

Thus, if R^c, $R(t)$, and $\frac{\mathrm{d}R}{\mathrm{d}t}(t)$ are known, $x(t)$ is exponentially stable.

If the estimates of R^c, $R(t)$, or $\frac{\mathrm{d}R}{\mathrm{d}t}(t)$ are not exact, minor oscillations of $x(t)$, and hence $P(t)$, can be expected. Such oscillations can be seen in Fig. 10.2 between $t = 25$s and $t = 30$s and between $t = 65$s and $t = 70$s. During these time intervals, the air gap between the coil and the sheet is very large and still increasing. As soon as the air gap reaches its maximum value around $t = 30$s and $t = 70$s, the oscillations diminish again.

B.2.1 Practical Implementation of the Power Controller

The control law (B.10) was used in the COMSOL MULTIPHYSICS implementation of the detailed process model. However, for the real plant, it is necessary to translate (B.10) into a control law for the source voltage $U^{\mathrm{s}}(t)$.

Let the complex impedance of the inductor and the electromagnetic field system be $R(t) + iX(t)$. Hence, the source voltage can be expressed by

$$U^{\mathrm{s}}(t) = \frac{1}{a^{\mathrm{tr}}}|R(t) + iX(t)|I(t). \tag{B.13}$$

The reactance $X(t)$ can be computed in the form

$$X(t) = \sqrt{\left(\frac{a^{\mathrm{tr}}U^{\mathrm{s}}(t)}{I(t)}\right)^2 - (R(t))^2} \geq 0 \tag{B.14}$$

and the time derivative of (B.13) together with (B.10) yields the control law

$$\begin{aligned}\frac{\mathrm{d}}{\mathrm{d}t}U^{\mathrm{s}}(t) = \frac{1}{a^{\mathrm{tr}}}\Bigg(&\frac{1}{|R(t) + iX(t)|}\left(R(t)\frac{\mathrm{d}}{\mathrm{d}t}R(t) + X(t)\frac{\mathrm{d}}{\mathrm{d}t}X(t)\right)I(t) + \\ &+ \frac{|R(t) + iX(t)|}{2I(t)(R(t) - R^c)}\left(-\frac{\mathrm{d}}{\mathrm{d}t}R(t)I^2(t) - \frac{1}{\gamma}\Big((R(t) - R^c)I^2(t) - u_d\Big)\right)\Bigg).\end{aligned} \tag{B.15}$$

Remark 6. Alternatively, if a^{tr} is not available, a cascade current controller for $I(t)$ can be implemented and (B.10) can be used directly. In this case, cascade controllers are used for $I(t)$, $u(t)$ and the sheet exit temperature $T^{\mathrm{out}}(t)$. Consequently, if the inductor is driven with AC voltage at 10kHz, the $I(t)$-controller works at 1kHz, the $u(t)$-controller works at 100Hz, and finally, the operation of the T^{out}-controller is limited to 10Hz.

APPENDIX C

Alternative Temperature Controller Design for Induction Heating

In this appendix, a flatness-based feedforward controller is designed for the control-oriented PDE model (8.44). The design is different from the one presented in Chapter 9 as it is based on a late-lumping approach. The resulting controller will exhibit the same behavior as the discrete-time feedforward controller without numerical diffusion. Both approaches have distinct (and complementary) advantages and drawbacks, as will be discussed at the end of this appendix.

C.1 Decomposition into Forward Model and Error Model

For the state variable $\overline{h}$, the input u, the output y and the function b, the following decompositions

$$\overline{h}(x,t) = \overline{h}^f(x,t) + \overline{h}^e(x,t) \tag{C.1a}$$

$$u(t) = u^f(t) + u^e(t) \tag{C.1b}$$

$$\overline{h}^{\text{out}}(t) = y^f(t) + y^e(t) \tag{C.1c}$$

$$b(x,t) = b_0(x) + \widetilde{b}(x,t), \qquad \int_0^{l_x} l_x l_y \widetilde{b}(x,t)\,\mathrm{d}x \equiv 0 \tag{C.1d}$$

are made. Note especially that b_0 and $\widetilde{b}$ are defined similar to (9.2). Insertion of (C.1) into (8.44) results in

$$\begin{aligned}\Big(\partial_t \overline{h}^f(x,t) + v_x \partial_x \overline{h}^f(x,t)\Big) + \Big(\partial_t \overline{h}^e(x,t) + v_x \partial_x \overline{h}^e(x,t)\Big) = \\ = \Big(b_0(x) + \widetilde{b}(x,t)\Big)\Big(u^f(t) + u^e(t) - P^l(t)\Big) \quad \text{(C.2a)}\end{aligned}$$

$$\frac{\mathrm{d}}{\mathrm{d}t} P^l(t) = w(t) \quad \text{(C.2b)}$$

$$\overline{h}^f(0,t) + \overline{h}^e(0,t) = \overline{h}^{\mathrm{in}}(t) \quad \text{(C.2c)}$$

$$\overline{h}^f(x,0) + \overline{h}^e(x,0) = \overline{h}_0(x) \quad \text{(C.2d)}$$

$$P^l(0) = P_0^l \quad \text{(C.2e)}$$

$$y^f(t) + y^e(t) = \overline{h}^f(l_x,t) + \overline{h}^e(l_x,t) + n(t). \quad \text{(C.2f)}$$

Let $b_0(x)$ be the known part of $b(x,t)$. With this, a forward model can be defined as

$$\partial_t \overline{h}^f(x,t) + v_x \partial_x \overline{h}^f(x,t) = b_0(x) u^f(t) \quad \text{(C.3a)}$$

$$\overline{h}^f(0,t) = \overline{h}^{\mathrm{in}}(t) \quad \text{(C.3b)}$$

$$\overline{h}^f(x,0) = \overline{h}_0(x) \quad \text{(C.3c)}$$

$$y^f(t) = \overline{h}^f(l_x,t). \quad \text{(C.3d)}$$

where $\overline{h}^f$ is the forward state variable and u^f is the feedforward control input. Note that all parameters of the forward model are known. Subtracting (C.3) from (C.2) results in the error model

$$\partial_t \overline{h}^e(x,t) + v_x \partial_x \overline{h}^e(x,t) = b_0(x)\Big(u^e(t) - P^l(t)\Big) + \widetilde{b}(x,t)\Big(u^f(t) + u^e(t) - P^l(t)\Big) \quad \text{(C.4a)}$$

$$\frac{\mathrm{d}}{\mathrm{d}t} P^l(t) = w(t) \quad \text{(C.4b)}$$

$$\overline{h}^e(0,t) = 0 \quad \text{(C.4c)}$$

$$\overline{h}^e(x,0) = 0 \quad \text{(C.4d)}$$

$$P^l(0) = P_0^l \quad \text{(C.4e)}$$

$$y^e(t) = \overline{h}^e(l_x,t) + n(t), \quad \text{(C.4f)}$$

where the forward and error models are interconnected by the coupling term $\widetilde{b}(x,t)u^f(t)$. The continuous-time forward and error models (C.3) and (C.4) correspond directly to the discrete-time forward and error models (9.5) and (9.6). In analogy to Section 9.2.1, a feedforward controller for the forward model is designed in the following.

C.2 Feedforward Temperature Control

In the following, a flatness-based inversion of the forward model (C.3) will be derived in order to obtain a continuous-time feedforward control law. The solution of (C.3) can be expressed as

$$\overline{h}^f(x,t) = \begin{cases} \overline{h}_0(x - v_x t) + \int_0^t u^f(t') b_0(x - v_x(t-t'))\,\mathrm{d}t', & t < \dfrac{x}{v_x} \\ \overline{h}^{\mathrm{in}}(t - \frac{x}{v_x}) + \int_{t-\frac{x}{v_x}}^t u^f(t') b_0(x - v_x(t-t'))\,\mathrm{d}t', & \dfrac{x}{v_x} \le t \end{cases} \tag{C.5a}$$

$$y^f(t) = \overline{h}^f(l_x, t). \tag{C.5b}$$

For the known part b_0 of b, let (cf. (9.2))

$$b_0 = \begin{cases} \beta, & \Delta l < x < l_x - \Delta l \\ 0, & \text{else,} \end{cases} \qquad \beta = \frac{1}{(l_x - 2\Delta l) l_y l_z}. \tag{C.6}$$

Using this definition for b_0, the output of the forward system results in

$$y^f(t) = \begin{cases} \overline{h}_0(l_x - v_x t), & t < \dfrac{\Delta l}{v_x}, \\ \overline{h}_0(l_x - v_x t) + \beta \displaystyle\int_0^{t-\frac{\Delta l}{v_x}} u^f(t')\,\mathrm{d}t', & \dfrac{\Delta l}{v_x} \le t < \dfrac{l_x - \Delta l}{v_x}, \\ \overline{h}_0(l_x - v_x t) + \beta \displaystyle\int_{t-\frac{l_x-\Delta l}{v_x}}^{t-\frac{\Delta l}{v_x}} u^f(t')\,\mathrm{d}t', & \dfrac{l_x - \Delta l}{v_x} \le t < \dfrac{l_x}{v_x}, \\ \overline{h}^{\mathrm{in}}(t - \frac{l_x}{v_x}) + \beta \displaystyle\int_{t-\frac{l_x-\Delta l}{v_x}}^{t-\frac{\Delta l}{v_x}} u^f(t')\,\mathrm{d}t', & \dfrac{l_x}{v_x} \le t, \end{cases} \tag{C.7}$$

with the (formal) time derivative

$$\dot{y}^f(t) = \begin{cases} -v_x \overline{h}_0'(l_x - v_x t), & t < \dfrac{\Delta l}{v_x}, \\ -v_x \overline{h}_0'(l_x - v_x t) + \beta u^f(t - \frac{\Delta l}{v_x}), & \dfrac{\Delta l}{v_x} < t < \dfrac{l_x - \Delta l}{v_x}, \\ -v_x \overline{h}_0'(l_x - v_x t) + \beta\Big(u^f(t - \frac{\Delta l}{v_x}) - u^f(t - \frac{l_x - \Delta l}{v_x})\Big), & \dfrac{l_x - \Delta l}{v_x} < t < \dfrac{l_x}{v_x}, \\ \dot{\overline{h}}^{\mathrm{in}}(t - \frac{l_x}{v_x}) + \beta\Big(u^f(t - \frac{\Delta l}{v_x}) - u^f(t - \frac{l_x - \Delta l}{v_x})\Big), & \dfrac{l_x}{v_x} < t. \end{cases} \tag{C.8}$$

Note that y^f is only controllable after a time $\frac{\Delta l}{v_x}$. This is due to the spatial distance Δl between the end of the coil and the measurement point of the exit temperature.

Using the desired values $y_d(t)$ in place of $y^f(t)$, the feedforward control law is now computed from (C.8) in the form

$$u^f(t) = \begin{cases} \frac{1}{\beta}\Big(\dot{y}_d(t+\frac{\Delta l}{v_x}) + v_x \overline{h}_0'(l_x - \Delta l - v_x t)\Big), & t < \dfrac{l_x - 2\Delta l}{v_x} \\ \frac{1}{\beta}\Big(\dot{y}_d(t+\frac{\Delta l}{v_x}) + v_x \overline{h}_0'(l_x - \Delta l - v_x t)\Big) + u^f(t - \frac{l_x - 2\Delta l}{v_x}), & \dfrac{l_x - 2\Delta l}{v_x} < t < \dfrac{l_x - \Delta l}{v_x} \\ \frac{1}{\beta}\Big(\dot{y}_d(t+\frac{\Delta l}{v_x}) - \dot{\overline{h}}^{\text{in}}(t - \frac{l_x - \Delta l}{v_x})\Big) + u^f(t - \frac{l_x - 2\Delta l}{v_x}), & \dfrac{l_x - \Delta l}{v_x} < t. \end{cases} \tag{C.9}$$

Note that $u^f(t)$ is defined recursively. This implies that $u^f(t)$ will be a quasi-periodic function with the period $\frac{l_x - 2\Delta l}{v_x}$.

C.3 Comparison to the Early-Lumping Design

The continuous-time feedforward comtroller (C.9) will now be compared to the discrete-time feedforward controller according to (9.12). The initial condition and entry temperatures are set to 30°C, which corresponds to

$$\overline{h}^{\text{in}}(t) = \overline{h}_0(x) = 780\frac{\text{MJ}}{\text{m}^3}, \quad \dot{\overline{h}}^{\text{in}}(t) = \overline{h}_0'(x) = 0. \tag{C.10}$$

The responses of both feedforward controllers to a ramp in $y_d(t)$ and $y_{d,k} = y_d(k\Delta t)$, respectively, are shown in Fig. C.1. The parameter C of the discrete-time controller (see (8.45)) was chosen as $C = 1$ to avoid numerical diffusion. In this case, it can be seen that both feedforward controllers exhibit almost the same behavior.

The continuous-time controller does not require a spatial step size and therefore the CFL condition (8.45) does not apply in this case. Instead, a memory of the past values of $u^f(t)$, $\overline{h}^{\text{in}}(t)$, and $y_d(t)$ is required.

Depending on the application, it may be more advantageous to use either the continuous-time or the discrete-time implementation. The inverse of the plate velocity v_x determines the required length of memory of $u^f(t)$, $\overline{h}^{\text{in}}(t)$, and $y_d(t)$ in (C.9). Therefore, the continuous-time implementation is more suitable for higher values of v_x.

Conversely, the discrete-time controller works properly for small plate velocities v_x. If, however, v_x is too large for the CFL condition to hold, then the discrete-time implementation is no longer valid.

In conclusion, if no bounds on v_x are given, it may be necessary to implement both feedforward controllers (9.12) and (C.9) and switch between them, depending on v_x or the CFL condition (8.45).

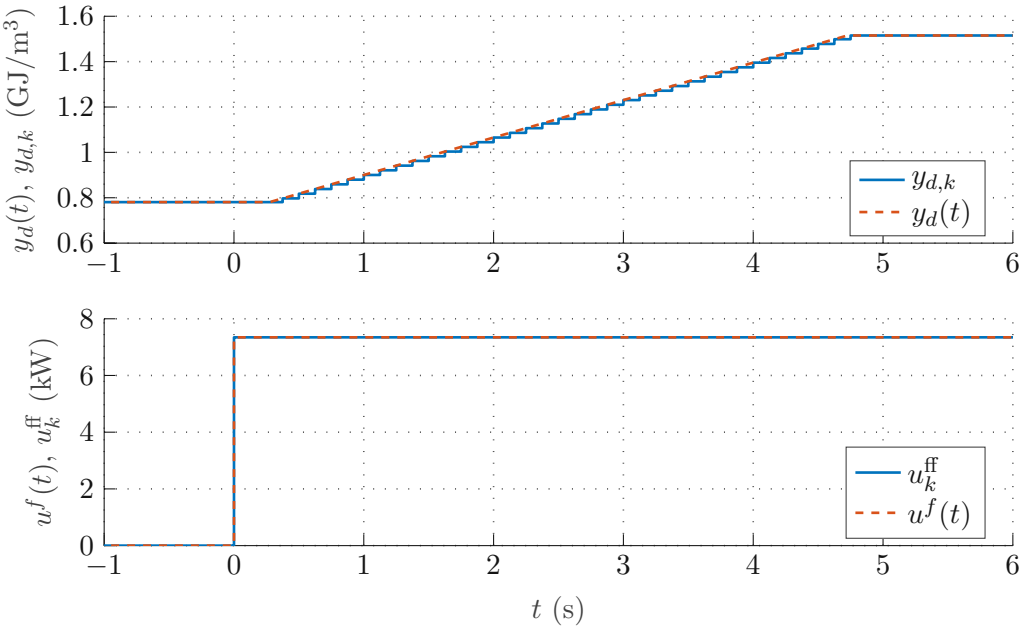

Figure C.1: Comparison of the continuous-time and discrete-time feedforward controllers.

Bibliography

[1] A. Aschauer, F. Roetzer, A. Steinboeck, and A. Kugi, "An Efficient Algorithm for Scheduling a Flexible Job Shop with Blocking and No-Wait Constraints", *IFAC-PapersOnLine*, 20th IFAC World Congress, vol. 50, no. 1, pp. 12 490–12 495, 2017. DOI: 10.1016/j.ifacol.2017.08.2056.

[2] ——, "Scheduling of a Flexible Job Shop with Multiple Constraints", *IFAC-PapersOnLine*, 16th IFAC Symposium on Information Control Problems in Manufacturing INCOM 2018, vol. 51, no. 11, pp. 1293–1298, 2018. DOI: 10.1016/j.ifacol.2018.08.354.

[3] ——, "Efficient Scheduling of a Stochastic No-Wait Job Shop with Controllable Processing Times", *Expert Systems with Applications*, vol. 162, p. 113 879, 2020. DOI: 10.1016/j.eswa.2020.113879.

[4] P. Azimzadeh and P. A. Forsyth, "Weakly Chained Matrices, Policy Iteration, and Impulse Control", *SIAM Journal on Numerical Analysis*, vol. 54, no. 3, pp. 1341–1364, 2016. DOI: 10.1137/15M1043431.

[5] H. D. Baehr and K. Stephan, *Wärme- und Stoffübertragung*, 7th ed. Berlin Heidelberg: Springer, 2010. DOI: 10.1007/978-3-642-10194-6.

[6] A. M. Bahman and S. A. Ebrahim, "Prediction of the minimum film boiling temperature using artificial neural network", *International Journal of Heat and Mass Transfer*, vol. 155, p. 119 834, 2020. DOI: 10.1016/j.ijheatmasstransfer.2020.119834.

[7] M. Bauccio, *ASM Metals Reference Book, 3rd Edition*. Materials Park, OH: ASM International, 1993.

[8] A. Bejan and A. D. Kraus, *Heat Transfer Handbook*. Hoboken, NJ: John Wiley & Sons, 2003.

[9] T. L. Bergman, Ed., *Introduction to Heat Transfer*, 6th ed. Hoboken, NJ: Wiley, 2011.

[10] J. Canny, "A Computational Approach To Edge Detection", *IEEE Transactions on Pattern Analysis and Machine Intelligence*, vol. PAMI-8, no. 6, pp. 679–698, 1986. DOI: 10.1109/TPAMI.1986.4767851.

[11] G. Chen and M. Gu, "Simulation of Steel Coil Heat Transfer in a High Performance Hydrogen Furnace", *Heat Transfer Engineering*, vol. 28, no. 1, pp. 25–30, 2007. DOI: 10.1080/01457630600985568.

[12] W.-H. Chen, M.-R. Lin, and T.-S. Leu, "Optimal Heating and Energy Management for Slabs in a Reheating Furnace", *Journal of Marine Science and Technology*, vol. 18, no. 1, pp. 24–31, 2010.

[13] R. Courant, K. Friedrichs, and H. Lewy, "Über die partiellen Differenzengleichungen der mathematischen Physik", *Mathematische Annalen*, vol. 100, no. 1, pp. 32–74, 1928. DOI: 10.1007/BF01448839.

[14] N. Depree, J. Sneyd, S. Taylor, M. Taylor, J. Chen, S. Wang, and M. O'Connor, "Development and Validation of Models for Annealing Furnace Control from Heat Transfer Fundamentals", *Computers & Chemical Engineering*, vol. 34, no. 11, pp. 1849–1853, 2010. DOI: 10.1016/j.compchemeng.2010.01.012.

[15] J. Egalon, S. Caux, P. Maussion, and O. Pateau, "Eigenvector Placement in State Space Control of Induction Heating Device", *IFAC Proceedings Volumes*, 8th Power Plant and Power System Control Symposium, vol. 45, no. 21, pp. 578–583, 2012. DOI: 10.3182/20120902-4-FR-2032.00101.

[16] J. Egalon, S. Caux, P. Maussion, M. Souley, and O. Pateau, "Multiphase System for Metal Disc Induction Heating: Modeling and RMS Current Control", *IEEE Transactions on Industry Applications*, vol. 48, no. 5, pp. 1692–1699, 2012. DOI: 10.1109/TIA.2012.2210176.

[17] H. Fujita and H. Akagi, "Pulse-Density-Modulated Power Control of a 4 kW, 450 kHz Voltage-Source Inverter for Induction Melting Applications", *IEEE Transactions on Industry Applications*, vol. 32, no. 2, pp. 279–286, 1996. DOI: 10.1109/28.491475.

[18] P. E. Gill, W. Murray, and M. A. Saunders, "SNOPT: An SQP Algorithm for Large-Scale Constrained Optimization", *SIAM Review*, vol. 47, no. 1, pp. 99–131, 2005. DOI: 10.1137/S0036144504446096.

[19] G. Goodwin, R. Middleton, M. Seron, and B. Campos, "Application of Nonlinear Model Predictive Control to an Industrial Induction Heating Furnace", *Annual Reviews in Control*, vol. 37, no. 2, pp. 271–277, 2013. DOI: 10.1016/j.arcontrol.2013.09.006.

[20] A. Y. Grigoriev, "Slope Angles of Rough Surface Asperities after Machining", *Journal of Friction and Wear*, vol. 36, no. 3, pp. 197–199, 2015. DOI: 10.3103/S106836661503006X.

[21] S. H. Han, S. W. Baek, S. H. Kang, and C. Y. Kim, "Numerical Analysis of Heating Characteristics of a Slab in a Bench Scale Reheating Furnace", *International Journal of Heat and Mass Transfer*, vol. 50, no. 9-10, pp. 2019–2023, 2007. DOI: 10.1016/j.ijheatmasstransfer.2006.10.048.

[22] S. H. Han and D. Chang, "Optimum Residence Time Analysis for a Walking Beam Type Reheating Furnace", *International Journal of Heat and Mass Transfer*, vol. 55, no. 15, pp. 4079–4087, 2012. DOI: 10.1016/j.ijheatmasstransfer.2012.03.049.

[23] X. Hao, J. Gu, N. Chen, W. Zhang, and X. Zuo, "3-D Numerical Analysis on Heating Process of Loads within Vacuum Heat Treatment Furnace", *Applied Thermal Engineering*, vol. 28, no. 14-15, pp. 1925–1931, 2008. DOI: 10.1016/j.applthermaleng.2007.12.007.

[24] D. Hömberg, T. Petzold, and E. Rocca, "Analysis and Simulations of Multifrequency Induction Hardening", *Nonlinear Analysis: Real World Applications*, vol. 22, pp. 84–97, 2015. DOI: 10.1016/j.nonrwa.2014.07.007.

[25] R. A. Horn and C. R. Johnson, *Matrix Analysis*, 2nd ed. Cambridge: Cambridge University Press, 2012. DOI: 10.1017/9781139020411.

[26] F. P. Incropera, D. P. DeWitt, T. L. Bergman, and A. S. Lavine, *Fundamentals of Heat and Mass Transfer*, 6th ed. Hoboken, NJ: John Wiley & Sons, 2006.

[27] J. D. Jackson, *Klassische Elektrodynamik*, 5th ed. Berlin Boston: De Gruyter, 2014.

[28] L. Jadachowski, A. Steinboeck, and A. Kugi, "Heat Transfer with Specular Reflections in an Experimental Annealing Device", *IFAC-PapersOnLine*, 8th Vienna International Conference on Mathematical Modelling, vol. 48, no. 1, pp. 494–499, 2015. DOI: 10.1016/j.ifacol.2015.05.069.

[29] P. Jafari, S. Sarmadi, S. Tasoujian, and H. Ghasemi, "Predictive AI platform on thin film evaporation in hierarchical structures", *International Journal of Heat and Mass Transfer*, vol. 171, p. 121 116, 2021. DOI: 10.1016/j.ijheatmasstransfer.2021.121116.

[30] A. Jaklič, F. Vode, and T. Kolenko, "Online Simulation Model of the Slab-Reheating Process in a Pusher-Type Furnace", *Applied Thermal Engineering*, vol. 27, no. 5, pp. 1105–1114, 2007. DOI: 10.1016/j.applthermaleng.2006.07.033.

[31] J.-Y. Jang and J.-B. Huang, "Optimisation of a Slab Heating Pattern with Various Skid Button Heights in a Walking-Beam-Type Reheating Furnace", *Ironmaking & Steelmaking*, vol. 45, no. 9, pp. 793–804, 2018. DOI: 10.1080/03019233.2017.1338386.

[32] J. Kang and Y. Rong, "Modeling and Simulation of Load Heating in Heat Treatment Furnaces", *Journal of Materials Processing Technology*, vol. 174, no. 1-3, pp. 109–114, 2006. DOI: 10.1016/j.jmatprotec.2005.03.037.

[33] A. I. Khan, M. M. Billah, C. Ying, J. Liu, and P. Dutta, "Bayesian Method for Parameter Estimation in Transient Heat Transfer Problem", *International Journal of Heat and Mass Transfer*, vol. 166, p. 120 746, 2021. DOI: 10.1016/j.ijheatmasstransfer.2020.120746.

[34] R. Kieffer and W. Hotop, *Pulvermetallurgie und Sinterwerkstoffe*. Berlin Heidelberg: Springer, 2013. DOI: 10.1007/978-3-642-94557-1.

[35] M. Y. Kim, "A Heat Transfer Model for the Analysis of Transient Heating of the Slab in a Direct-Fired Walking Beam Type Reheating Furnace", *International Journal of Heat and Mass Transfer*, vol. 50, no. 19, pp. 3740–3748, 2007. DOI: 10.1016/j.ijheatmasstransfer.2007.02.023.

[36] K. Kunisch and S. Volkwein, "Galerkin Proper Orthogonal Decomposition Methods for a General Equation in Fluid Dynamics", *SIAM Journal on Numerical Analysis*, vol. 40, no. 2, pp. 492–515, 2002. DOI: 10.1137/S0036142900382612.

[37] D. E. Lee and M. Y. Kim, "Optimum Residence Time for Steel Productivity and Energy Saving in a Hot Rolled Reheating Furnace", *Journal of Mechanical Science and Technology*, vol. 27, no. 9, pp. 2869–2877, 2013. DOI: 10.1007/s12206-013-0735-1.

[38] G. W. Lee and M. Y. Kim, "On the Thermal Behavior of the Slab in a Reheating Furnace with Radiation", *International Journal of Mechanical, Aerospace, Industrial, Mechatronic and Manufacturing Engineering*, vol. 8, no. 5, pp. 922–927, 2014. DOI: 10.5281/zenodo.1092544.

[39] J. H. Lienhard and J. H. Lienhard, *A heat transfer textbook*, Fifth Edition. Mineola, New York: Dover Publications, Inc, 2019.

[40] D. Lindholm, "A Finite Element Method for Solution of the Three-Dimensional Time-Dependent Heat-Conduction Equation with Application for Heating of Steels in Reheating Furnaces", *Numerical Heat Transfer, Part A: Applications*, vol. 35, no. 2, pp. 155–172, 1999. DOI: 10.1080/104077899275308.

[41] L. Ljung, *System Identification: Theory for the User*, 2nd ed. Upper Saddle River, NJ: Prentice Hall PTR, 1999.

[42] O. Lucia, P. Maussion, E. Dede, and J. Burdio, "Induction Heating Technology and Its Applications: Past Developments, Current Technology, and Future Challenges", *IEEE Transactions on Industrial Electronics*, vol. 61, no. 5, pp. 2509–2520, 2014. DOI: 10.1109/TIE.2013.2281162.

[43] A. Mochida, K. Kudo, Y. Mizutani, M. Hattori, and Y. Nakamura, "Transient Heat Transfer Analysis in Vacuum Furnaces Heated by Radiant Tube Burners", *Energy Conversion and Management*, vol. 38, no. 10, pp. 1169–1176, 1997. DOI: 10.1016/S0196-8904(96)00146-X.

[44] H. P. Ngoc, H. Fujita, K. Ozaki, and N. Uchida, "Phase Angle Control of High-Frequency Resonant Currents in a Multiple Inverter System for Zone-Control Induction Heating", *IEEE Transactions on Power Electronics*, vol. 26, no. 11, pp. 3357–3366, 2011. DOI: 10.1109/TPEL.2011.2146278.

[45] K. L. Nguyen, S. Caux, X. Kestelyn, O. Pateau, and P. Maussion, "Resonant Control of Multi-Phase Induction Heating Systems", in *IECON 2012 - 38th Annual Conference on IEEE Industrial Electronics Society*, Montreal, QC, Canada, 2012, pp. 3293–3298. DOI: 10.1109/IECON.2012.6389371.

[46] N.-J. Park, D.-Y. Lee, and D.-S. Hyun, "A Power-Control Scheme With Constant Switching Frequency in Class-D Inverter for Induction-Heating Jar Application", *IEEE Transactions on Industrial Electronics*, vol. 54, no. 3, pp. 1252–1260, 2007. DOI: 10.1109/TIE.2007.892741.

[47] H. N. Pham, H. Fujita, K. Ozaki, and N. Uchida, "Estimating Method of Heat Distribution Using 3-D Resistance Matrix for Zone-Control Induction Heating Systems", *IEEE Transactions on Power Electronics*, vol. 27, no. 7, pp. 3374–3382, 2012. DOI: 10.1109/TPEL.2011.2179984.

[48] Plansee SE, *Molybdenum, tungsten, tantalum, niobium, chromium. Strong metals make strong products. | Plansee*. [Online]. Available: https://www.plansee.com (visited on 12/21/2020).

[49] R. Prieler, B. Mayr, M. Demuth, B. Holleis, and C. Hochenauer, "Prediction of the Heating Characteristic of Billets in a Walking Hearth Type Reheating Furnace Using CFD", *International Journal of Heat and Mass Transfer*, vol. 92, pp. 675–688, 2016. DOI: 10.1016/j.ijheatmasstransfer.2015.08.056.

[50] L. Pyta, A. Deutschmann, F. Rötzer, D. Abel, and A. Kugi, "Reduced-Order Modeling of a Radiative Heating Process with Movable Radiators", *IFAC-PapersOnLine*, 11th IFAC Symposium on Nonlinear Control Systems NOLCOS 2019, vol. 52, no. 16, pp. 346–351, 2019. DOI: 10.1016/j.ifacol.2019.11.804.

[51] M. Raissi, P. Perdikaris, and G. E. Karniadakis, "Physics-informed neural networks: A deep learning framework for solving forward and inverse problems involving nonlinear partial differential equations", *Journal of Computational Physics*, vol. 378, pp. 686–707, 2019. DOI: 10.1016/j.jcp.2018.10.045.

[52] S. Rhein and K. Graichen, "Dynamic Optimization of Induction Heat-Up and Surface Hardening Processes on Complex Spatial Domains", in *2015 IEEE Conference on Control Applications (CCA)*, Sydney, NSW, Australia, 2015, pp. 1829–1834. DOI: 10.1109/CCA.2015.7320875.

[53] S. Rhein, T. Utz, and K. Graichen, "Dynamische Optimierung von Multiphysik-Problemen am Beispiel induktiver Heizvorgänge", *at - Automatisierungstechnik*, vol. 63, no. 9, pp. 713–726, 2015. DOI: 10.1515/auto-2015-0029.

[54] ——, "Optimal Control of Induction Heating Processes Using FEM Software", in *2015 European Control Conference (ECC)*, Linz, Austria, 2015, pp. 515–520. DOI: 10.1109/ECC.2015.7330595.

[55] F. Roetzer, A. Aschauer, L. Jadachowski, A. Steinboeck, and A. Kugi, "Temperature Control for Induction Heating of Thin Strips", *IFAC-PapersOnLine*, 21st IFAC World Congress, vol. 53, no. 2, pp. 11 968–11 973, 2020. DOI: 10.1016/j.ifacol.2020.12.722.

[56] F. Roetzer, A. Aschauer, A. Steinboeck, and A. Kugi, "A Computationally Efficient 3D Mathematical Model of a Molybdenum Batch-Reheating Furnace", *IFAC-PapersOnLine*, 9th Vienna International Conference on Mathematical Modelling, vol. 51, no. 2, pp. 819–824, 2018. DOI: 10.1016/j.ifacol.2018.04.015.

[57] ——, "Reheating Time Optimization for Metal Products in Batch-Type Furnaces", *International Journal of Heat and Mass Transfer*, 2021, submitted.

[58] H. H. Rosenbrock, "A Lyapunov Function with Applications to Some Nonlinear Physical Systems", *Automatica*, vol. 1, no. 1, pp. 31–53, 1963. DOI: 10.1016/0005-1098(63)90005-0.

[59] A. Saboonchi, S. Hassanpour, and S. Abbasi, "New Heating Schedule in Hydrogen Annealing Furnace Based on Process Simulation for Less Energy Consumption", *Energy Conversion and Management*, vol. 49, no. 11, pp. 3211–3216, 2008. DOI: 10.1016/j.enconman.2008.05.024.

[60] A. Saboonchi, S. Hassanpour, and F. Bayati, "Design of Heating Cycle in Hydrogen Annealing Furnaces", *Materials and Manufacturing Processes*, vol. 24, no. 12, pp. 1453–1458, 2009. DOI: 10.1080/10426910903124837.

[61] S. S. Sahay and A. M. Kumar, "Applications of Integrated Batch Annealing Furnace Simulator", *Materials and Manufacturing Processes*, vol. 17, no. 4, pp. 439–453, 2002. DOI: 10.1081/AMP-120014227.

[62] S. S. Sahay, R. Mehta, S. Raghavan, R. Roshan, and S. J. Dey, "Process Analytics, Modeling, and Optimization of an Industrial Batch Annealing Operation", *Materials and Manufacturing Processes*, vol. 24, no. 12, pp. 1459–1466, 2009. DOI: 10.1080/10426910903179922.

[63] *SemI40 - Power Semiconductor and Electronics Manufacturing 4.0*. [Online]. Available: http://www.semi40.eu/ (visited on 12/15/2020).

[64] P. N. Shivakumar and K. H. Chew, "A Sufficient Condition for Nonvanishing of Determinants", *Proceedings of the American Mathematical Society*, vol. 43, no. 1, pp. 63–66, 1974. DOI: 10.2307/2039326.

[65] V. K. Singh and P. Talukdar, "Comparisons of Different Heat Transfer Models of a Walking Beam Type Reheat Furnace", *International Communications in Heat and Mass Transfer*, vol. 47, pp. 20–26, 2013. DOI: 10.1016/j.icheatmasstransfer.2013.06.004.

[66] L. Sirovich, "Turbulence and the Dynamics of Coherent Structures Part III: Dynamics and Scaling", *Quarterly of Applied Mathematics*, vol. 45, no. 3, pp. 583–590, 1987. DOI: 10.1090/qam/910464.

[67] D. Staalman and A. Kusters, "On-Line Slab Temperature Calculation and -Control", in *International Mechanical Engineering Congress and Exposition*, Atlanta, GA, USA, 1996, pp. 1–8.

[68] A. Steinboeck, D. Wild, T. Kiefer, and A. Kugi, "A Mathematical Model of a Slab Reheating Furnace with Radiative Heat Transfer and Non-Participating Gaseous Media", *International Journal of Heat and Mass Transfer*, vol. 53, no. 25-26, pp. 5933–5946, 2010. DOI: 10.1016/j.ijheatmasstransfer.2010.07.029.

[69] S. Strommer, M. Niederer, A. Steinboeck, L. Jadachowski, and A. Kugi, "Nonlinear Observer for Temperatures and Emissivities in a Strip Annealing Furnace", *IEEE Transactions on Industry Applications*, vol. 53, no. 3, pp. 2578–2586, 2017. DOI: 10.1109/TIA.2017.2669327.

[70] Y. S. Touloukian and D. P. DeWitt, *Thermal Radiative Properties: Metallic Elements and Alloys*. Boston, MA: Springer, 1970.

[71] R. Wallis and J. Ward, "The Thermal Performance of an Electrical Resistance Furnace for Heating Steel Slabs", in *XII International Congress on Electroheat*, Montreal, Canada, 1992, pp. 977–986.

[72] D. Whitehouse, *Surfaces and Their Measurement*. Amsterdam: Elsevier, 2002. DOI: 10.1016/B978-1-903996-01-0.X5000-2.

[73] B. Wu, A. M. Arnold, E. Arnold, G. Downey, and C. Q. Zhou, "CFD Analysis of Batch-Type Reheating Furnace", in *International Mechanical Engineering Congress and Exposition, Volume 6: Energy Systems: Analysis, Thermodynamics and Sustainability*, Seattle, Washington, USA, 2007, pp. 753–759. DOI: 10.1115/IMECE2007-42454.

[74] Y.-Y. Yang and Y.-Z. Lu, "Development of a Computer Control Model for Slab Reheating Furnaces", *Computers in Industry*, vol. 7, no. 2, pp. 145–154, 1986. DOI: 10.1016/0166-3615(86)90036-9.

[75] J. Zerad, S. Riachy, P. Toussaint, and J.-P. Barbot, "A Nonlinear Controller for Parallel Induction Heating Systems", *IFAC-PapersOnLine*, 19th IFAC World Congress, vol. 47, no. 3, pp. 11 617–11 622, 2014. DOI: 10.3182/20140824-6-ZA-1003.00311.